

UNCLASSIFIED

AD NUMBER

AD810227

NEW LIMITATION CHANGE

TO

**Approved for public release, distribution
unlimited**

FROM

**Distribution authorized to U.S. Gov't.
agencies and their contractors;
Administrative/Operational Use; MAR 1967.
Other requests shall be referred to
Ballistic Systems and Space Systems Div.,
AFSC, Los Angeles AFS, Los Angeles, CA.**

AUTHORITY

**Space and Missile Systems Organization ltr
dtd 19 Jan 1972**

THIS PAGE IS UNCLASSIFIED

Best Available Copy

810227

Investigations in the Far-Infrared with a Lamellar Grating Interferometer

MARCH 1967

Prepared by J. M. DOWLING
Space Physics Laboratory
Laboratories Division
Laboratory Operations
AEROSPACE CORPORATION

Prepared for **BALLISTIC SYSTEMS AND SPACE SYSTEMS DIVISIONS**
AIR FORCE SYSTEMS COMMAND
LOS ANGELES AIR FORCE STATION
Los Angeles, California

Air Force Report No.
SSD-TR-67-30

Aerospace Report No.
TR-1001(9260-01)-7

INVESTIGATIONS IN THE FAR-INFRARED WITH A
LAMELLAR GRATING INTERFEROMETER

Prepared by

J. M. Dowling
Space Physics Laboratory

Laboratories Division
Laboratory Operations
AEROSPACE CORPORATION

March 1967

Prepared for

BALLISTIC SYSTEMS AND SPACE SYSTEMS DIVISIONS
AIR FORCE SYSTEMS COMMAND
LOS ANGELES AIR FORCE STATION
Los Angeles, California

~~Distribution and handling instructions~~

FOREWORD

This report is published by the Aerospace Corporation, El Segundo, California, under Air Force Contract No. AF 04(695)-1001 and documents research carried out from January 1965 to January 1967. On 17 March this report was submitted to Capt. R. D. Eaglet for review and approval.

Contributing authors to this work were Drs. R. T. Hall, C. M. Randall, and R. D. Rawcliffe. The authors would like to express their appreciation to Drs. E. B. Mayfield, R. A. Becker, and B. H. Billings for their constant encouragement and many helpful discussions concerning the work reported here. The assistance of Mr. S. B. Wiemokly and Mr. T. E. Mott in the fabrication and maintenance of the experimental apparatus is gratefully acknowledged.

Approved

R.A. Becker
R. A. Becker, Director
Space Physics Laboratory
Laboratories Division
Laboratory Operations

Publication of this report does not constitute Air Force approval of the report's findings or conclusions. It is published only for the exchange and stimulation of ideas.

Approved

Robert D. Eaglet
Robert D. Eaglet
Capt., USAF
Chief, Space Environment and
Electronics Branch

ABSTRACT

The theory and practice of far-infrared, two-beam interferometry is summarized. A description of the instrumentation and performance of the Aerospace Corporation two-beam, double-beam, far-infrared lamellar-grating interferometer is given. Detailed experimental measurements and analyses of the pure rotational spectra of the atmospheric molecules nitric oxide (NO) and water (H_2O) are presented. Also discussed in depth are measurements of the optical constants of some important far-infrared window materials and the fabrication and performance of narrow bandpass filters for the far-infrared. Included is a discussion of noise, experimental errors, and problems in the practice of two-beam interferometry. Finally, a summary is given of the computational programs necessary and convenient for reducing the raw interferometric data to their more readily used spectral form.

CONTENTS

ABSTRACT	iii
I. INTRODUCTION	1
II. THEORY	5
III. DESCRIPTION OF THE INSTRUMENT	25
A. Optics	25
B. Mechanics	32
C. Electronics and Data Recording System	37
IV. RESULTS	43
A. High Resolution Spectroscopy of Gases	43
1. Carbon Monoxide	43
2. Deuterium Chloride	51
3. Nitric Oxide	53
4. Water Vapor	65
5. Line Width	85
6. Absorption of Gases in the Medium Pressure Ranges (~1 - 10 atm)	93
B. Optical Constants of Solids	97
C. Index of Refraction of Gases	111
D. Narrow Bandpass Filters	112
V. NOISE, EXPERIMENTAL ERRORS, AND PROBLEMS	123
A. Origin Error ($x = 0$ point)	123
B. Periodic Error	126
C. Choice of Δx	128
D. Channel Spectra	130
E. Long Term Source Fluctuations - Step Functions	131
F. Stop-and-Go Scanning and Time Constants	133
G. Background Radiation	137
H. Drift	140
I. Noise	144

CONTENTS (Continued)

VI COMPUTATIONAL TECHNIQUES	157
A. Introduction	157
B. Computational Algorithms	157
1. Direct Sum Algorithm	157
2. Cooley-Tukey Algorithm	158
3. Comparison of Algorithms	162
4. Test Problem	163
C. Computer Program	169
REFERENCES	181
APPENDIX - INTERFEROMETRY AND CONVENTIONAL SPECTROSCOPY	A-1

TABLES

1.	First Derivative Extremes (Referenced to ν_0 for the Pure Rotational Lines of Carbon Monoxide	47
2.	Observed Frequencies and Deviations of Calculated Frequencies of Nitric Oxide	59
3.	Effective Rotational Constants of Nitric Oxide	60
4.	Rotational Constants of Nitric Oxide	62
5.	Pure Rotational Transistions of Water Vapor	68
6.	Other Transitions Used to Derive Energy Levels	75
7.	H_2O Energy Levels	77
8.	Comparison of Observed and Calculated Microwave Transitions of Water Vapor	82
9.	Parameters Derived from Least-Squares Fits to the Sum Rules of Fraley and Rao	83
10.	Equilibrium Rotational Constants	85
11.	Ground State Rotational Constants of the Water Molecule	86
12.	Distortions Caused by Mislocation of Origin	125
13.	Calculated (from Eq. 45) and Observed Standard Deviations	147
14.	Comparison of Integral Transform and Sum Transform of Straight Line Interferogram	166
A-1.	Comparison of a Conventional Grating Spectrometer and a Lamellar Grating Interferometer	A-3
A-2.	Comparison of Experimental Parameters Illustrated in Figure 71	A-6

FIGURES

1.	Interferograms for "source-like" $I(v)$	9
2.	Interferogram of a line with a Lorentz shape	12
3.	The scanning function of a two-beam interferometer	15
4.	Two δ function lines separated by $0.715 (L)^{-1}$ as would be seen by a two-beam interferometer which has been scanned out to $x_{max} = L$	17
5.	Two δ function lines separated by $(L)^{-1}$ as would be seen by a two-beam interferometer which has been scanned out to $x_{max} = L$	18
6.	The Lorentz line shape	21
7.	Plot of $I_L(v)$ for a Lorentz line with $L\epsilon = 3/4$	22
8.	Plot of $I_L(v)$ for a Lorentz line with $L\epsilon = 1/2$	23
9.	Plot of $I_L(v_0)/I_F$ versus $L\epsilon$	24
10.	Lamellar grating interferometer optical diagram	25
11.	Front view of the lamellar grating	28
12.	Side view of the interferometer	30
13.	The interferometer in place in the vacuum tank	31
14.	Electronic console and vacuum tank	32
15.	Back view of lamellar grating	36
16.	Block diagram of lamellar grating interferometer system	39
17.	Single-beam and double-beam interferometric features of the pure rotational spectrum of CO	41
18.	Single-beam and double-beam interferometric features of the channel spectrum of a plane parallel window of crystalline quartz	41
19.	The pure rotational double-beam interferogram of CO	43

FIGURES (Continued)

20.	The pure rotational spectrum of CO	45
21.	The $J = 17 \rightarrow 18$ transition of CO	46
22.	A portion of the pure rotational, double-beam interferogram of CO	49
23.	The pure rotational, double-beam interferogram of DCl	52
24.	Selected regions of the pure rotational spectrum of DCl	54
25.	The pure rotational, double-beam interferogram of NO	57
26.	The pure rotational spectrum of NO	58
27.	The pure rotational spectrum of water vapor	67
28.	The 38.6 and 59.9 cm^{-1} regions of the pure rotational spectrum of water vapor	72
29.	The sum rule plot for the "a" axis of the water molecule	80
30.	The sum rule plot for the "b" axis of the water molecule	80
31.	The sum rule plot for the "c" axis of the water molecule	81
32.	The sum rule plot for the combination of all axes of the water molecule	81
33.	The natural logarithm of the normalized signature intensity versus the reduced optical path difference for CO	87
34.	Linewidth parameter versus pressure for CO	87
35.	Correction curve for (Δv_D) due to finite resolution for weakly absorbing lines. curve A. Curve B is the variation of ϵ_L/ϵ_x	94
36.	Correction curve for (Δv_D) due to finite resolution for medium absorbing lines	95
37.	Preliminary line widths (self-broadened) for the pure rotational lines of CO	96

FIGURES (Continued)

38.	Absorption cell for medium pressures (-1 to 10 atm)	97
39.	Geometry of sample for channel spectrum index of refraction measurements	99
40.	Maximum sample thickness usable with present techniques for channel spectrum determination of refractive index in the FIR, for values of the real index n and absorption coefficient $\alpha = 4\pi k\nu$	103
41.	Transmittance of fused quartz $T(\nu)$ showing both channels and transmittance change caused by changing absorption	104
42.	Difference interferogram and spectrum for fused quartz, with and without editing	105
43.	Absorption coefficient, $\alpha = 4\pi k\nu$, and real refractive index for fused quartz	107
44.	Region of interferogram and spectrum for silicon sample	108
45.	Absorption coefficient and real refractive index for silicon	109
46.	Mean transmittance $\tau(\nu)$ of silicon	109
47.	Absorption coefficient and real refractive index for germanium	110
48.	Mean transmittance for germanium	110
49.	Details of filter construction	114
50.	Photograph of a completed filter	115
51.	Transmission of a single wire mesh as a function of reduced frequency	116
52.	Energy throughput of a wire mesh filter consisting of two 750-mesh screens separated by a 0.0805-cm spacer	117
53.	Measured finesse for 750-mesh filters of different spacing	119
54.	Reduction in finesse for 750-mesh, 0.081-cm spacing filter due to limitations of measuring technique	119

FIGURES (Continued)

55.	Transmission as a function of frequency for a 750-mesh, 0.081-cm spacing filter for two beam convergence angles	120
56.	Calculated transmission halfway between peaks of a 750-mesh filter	121
57.	Appearance of a Lorentz line when an error has been made in the location of the origin	124
58.	Optical path difference error in a linear inductosyn scale	128
59.	Schematic representation of signals into and out of the 19-cycle detector during one data acquisition cycle	135
60.	Effect on the spectrum of a large detector time constant	136
61.	Averages over adjacent 10-point regions of a water vapor interferogram, showing a case of nearly linear drift	140
62.	Difference between the spectrum near $\nu = 0$ as obtained from the uncorrected interferogram and that obtained from the same interferogram after dividing each point by $(1 - ax)$	142
63.	Individual lines obtained from the corrected and the uncorrected interferogram	143
64.	$I(\nu)$ and $I_L(\nu)$ for $L = (5\epsilon)^{-1}$	150
65.	Spectrum S/N curves and maximum intensity to sidelobe intensity curve	151
66.	Two identical Lorentz lines separated by 4ϵ , and $L\epsilon = 0.200$	155
67.	Comparison of computing times for the Direct Sum and Cooley-Tukey algorithms on the same data run on an IBM 7090 computer	161
68.	Test interferogram as plotted by the computer	164

FIGURES (Continued)

69.	Transform of test interferogram as computed and plotted by the computer	165
70.	Difference between sum and integral for different sampling frequencies of the interferogram	168
71.	Flow Chart of Direct Sum Method	170
72.	Flow Chart of Cooley-Tukey Method	174
A-1.	The 55 to 56 cm^{-1} region of the water vapor spectrum	A-5

1. INTRODUCTION

It is the purpose of this report to summarize the experience and results obtained with the Aerospace Corporation two-beam, double-beam lamellar-grating interferometer.

The history and status of two-beam interferometry, sometimes called Fourier transform spectroscopy or autocorrelation spectroscopy, up to October 1965 has been summarized by Loewenstein (Ref. 1), and the interested reader is referred to his article for a comprehensive survey. Briefly, Fourier transform spectroscopy, which had its inception in the works of Michelson (Ref. 2), has proved to be a valuable tool in the investigation of the far-infrared region (FIR) of the electromagnetic spectrum. Fellgett (Refs. 3, 4) has shown that, when detector noise is the limiting factor, the gain in signal to noise (S/N) of an interferometer over a conventional single-slit dispersive spectrometer is $\sqrt{N}/2$, where N is the number of spectral elements in the region studied. This is called the multiplex or Fellgett advantage.

There are two types of two-beam interferometers used in the infrared (IR). The classic Michelson interferometer, which utilizes division of amplitude to produce the two interfering beams, has been developed by Gebbie (Ref. 5) for use in the FIR. J. Connes (Ref. 6) has also used a Michelson for low-level intensity studies in the middle- and near-IR. Recently, J. Connes and P. Connes (Ref. 7) have reported on truly spectacular spectra of Mars and Venus in the near-IR using a Michelson interferometer. In the FIR, Bell (Refs. 8, 9) and Chamberlin, et al. (Ref. 10) have exploited the fact that in a Michelson interferometer the interfering beams are well separated in space before recombination. This allows placing reflective or absorbing samples in one arm of the Michelson interferometer and thus obtaining phase information.

A second type of interferometer, the lamellar grating interferometer, produces the two interfering beams by dividing the wave front (thus avoiding experimental difficulties typical of a beamsplitter). This interferometer has been developed by Strong and Vanasse (Refs. 11-13). A comparison between these two types of interferometers and a conventional grating spectrometer has been reported by Richards (Ref. 14). Recently a high resolution lamellar grating has been described by Hall, et al. (Ref. 15). It is an FIR instrument which has a double-beam differencing mode of operation that helps alleviate the dynamic range problem.

The present report consists of a brief survey of the theory of two-beam interferometry with emphasis on the experimental techniques necessary for obtaining the interferometric data. A brief discussion of some idealized cases is presented to familiarize the reader with interferograms (the raw data from interferometers) and their direct interpretation in some simple cases. Next, the instrumentation of the two-beam, double-beam lamellar grating is described and the advantages and disadvantages of its double-beam differencing mode of operation discussed. The next section consists of experimental results obtained with this instrument. Included are the measurement and analysis of pure rotational spectra, linewidth measurements and pressure shifts, index of refraction measurements of gases, optical constants for solids in the FIR, and the fabrication and performance of narrow bandpass filters for the FIR. Some of these results have been published, others are being prepared for publication, and some are preliminary in nature (and in these cases the conclusions drawn must be considered somewhat speculative). The next section deals with some of the more important experimental errors encountered in two-beam interferometry and how these errors are reflected in the spectrum. Also in this section are discussed some of the problems we have encountered which are peculiar to two-beam interferometry (and some peculiar to our instrument) and how their eventual solution will undoubtedly lead to a higher S/N ratio

for FIR interferometry. The last section deals with the computer programs and options that are necessary and useful to convert the interferogram into the more familiar spectrum. Included is a discussion and listing (FORTRAN) of the conventional "direct sum" Fourier cosine transform program and the less flexible, but much faster, Cooley-Tukey program.

II. THEORY

There are many excellent treatments (Refs. 6, 12, 16-20) that cover with varying degrees of rigor the theory and practice of two-beam interferometry. In this section we shall only summarize the theory and then discuss a few simple theoretical examples which will be useful in understanding the experimental results in Section IV.

Consider a beam of monochromatic electromagnetic energy which is passed through a two-beam interferometer. The intensity $F'(x)$ detected would have the following form (Ref. 21).

$$F'(x) = I + I \cos 2\pi x\nu \quad (1)$$

where I is the average intensity (i. e., the average of $F'(x)$), x is the optical path difference generated by the interferometer of one of the interfering beams with respect to the other, and $\nu (= \lambda^{-1})$ is the wavenumber of the radiation. If instead of monochromatic energy we have a band of wavenumbers, then Eq. (1) may be generalized

$$F'(x) = \int_0^{\infty} I(\nu) d\nu + \int_0^{\infty} I(\nu) \cos 2\pi x\nu d\nu \quad (2)$$

The first integral is a constant and is the total intensity of the spectrum $I(\nu)$ (which also equals $F'(\infty)$). In terms of $F'(x)$ it is seen to be $(1/2)F'(0)$ by evaluating Eq. (2) at $x = 0$. Thus

$$F'(x) - \frac{1}{2} F'(0) = \int_0^{\infty} I(\nu) \cos 2\pi x\nu d\nu = F(x) \quad (3)$$

In the literature $F(x)$ is called the interferogram or interferogram function, as is $F'(x)$. To avoid confusion we shall call $F(x)$ the interferogram function and $F'(x)$ the interferogram.

$F(x)$ is the Fourier Cosine Transform (FCT) of $I(v)$. It then follows that if $F(x)$ is Fourier cosine transformed, the result will be $I(v)$. That is, aside from a multiplicative constant and recognizing that $F(x)$ is an even function of x ,

$$I(v) = \int_0^\infty F(x) \cos 2\pi vx dx \quad (4)$$

In this form Eq. (4) is of limited practical importance. In general, if $F(x)$ is known, a rather large computer is needed to calculate $I(v)$, and Eq. (4) must be put into a form for which a computer program can be written. Analog computers have been used¹ but usually with digital input data. It is usually digital computers that are used to solve Eq. (4) for $I(v)$. We therefore consider only the requirements for $F(x)$ in digital form that will lead to an accurate representation of $I(v)$.

Let $F(x)$ be measured at points x_0, x_1, x_2, \dots , then

$$I(v) \approx \sum_{m=0}^{\infty} F(x_m) \cos(2\pi x_m v) \Delta x_m$$

which reduces to, if all the Δx_m are equal and x_0 is at $x = 0$,²

¹A number of papers describing such computers were given at the "Colloque Sur Les Methodes Nouvelles de Spectroscopie Instrumentale," April 25-29, 1966, Bellevue, France. Many of these papers are scheduled for publication in the Journal de Physique early in 1967.

²This is very convenient for computer programming and for speed in the computer calculation. See Section VI.

$$I(v) = \Delta x [F(0)/2 + \sum_{m=1}^N F(m\Delta x) \cos(2\pi m\Delta x v)] \quad (5)$$

Now it is necessary to see how closely this summation will approximate the true $I(v)$. This has been discussed by Strong and Vanasse (Ref. 12). Making use of sampling theorems from information theory, they obtain if

$$\Delta x \leq \frac{1}{2v_c} \quad (6)$$

where v_c is the highest wavenumber having non-zero energy in the spectrum, then $I(v)$ is completely determined.³

This relation is quite important as Δx should be as large as possible in order to allow more time to measure each $F(m\Delta x)$. We anticipate the discussion of Section V by pointing out it is better to spend more time measuring the $F(m\Delta x)$ with the largest allowed Δx than it is to measure a larger number of the $F(m\Delta x)$ for a shorter time each using a smaller Δx . What happens when Δx is chosen too large is discussed in Section V. It is also apparent that if the spectral range of interest extends to v_a , then v_c should be chosen (by filtering, etc.) as close to v_a as is compatible with good S/N.

Now, what is the effect on $I(v)$ when the sum (or integral) is not carried out to infinity? An infinitely long (analog or digital) interferogram is a physical

³This is a sufficient, but not necessary, condition. Connes (Ref. 6) has shown that if the spectral range of v being passed by the interferometer lies between v_1 and v_2 , it is possible to choose $\Delta x = [2(v_2 - v_1)]^{-1}$ or somewhat smaller, but certainly $\geq (2v)^{-1}$. Also if the double-beam differencing technique is used (see Section III) and if the highest observed absorption is at v_c , then one can choose $\Delta x = (2v_c)^{-1}$ (really a bit smaller since the feature will in general have finite width) even though there is energy passed by the instrument at higher wavenumber.

impossibility. There are two important questions to consider: First, in the absence of noise, what is the effect of the truncation of the interferogram, i.e., taking the integration out to $x_{\max} = L$ or the sum out to $m = L/\Delta x$? This is answered later in this section where the scanning function of the two-beam interferometer is discussed. The second question concerns the effect of noise. This is discussed in Section V.

Except to the practitioners of the art of two-beam interferometry, raw interferometric data, i.e., the interferograms, appear strange and unsuggestive. We shall now discuss some simple (idealized) examples of interferograms and their interpretation. This material provides the background for interpretation of the experimentally observed interferograms discussed in Section IV.

The simplest broadband $I(\nu)$, such as a source would present, is $I(\nu) = I_0 \nu_c$, a constant up to ν_c , and zero beyond. Substitution into Eq. (2) yields

$$F'_1(x) = I_0 \nu_c [1 + (\sin y/y)]$$

where $y = 2\pi x \nu_c$.

A more realistic source function would be one with zero or little energy at low wavenumber (because of the blackbody radiation law), rising toward larger ν , then falling to zero at ν_c (due to the filtering optics).

A function meeting this requirement is

$$I(\nu) = 6I_0 \left[\left(\frac{\nu}{\nu_c} \right) - \left(\frac{\nu^2}{\nu_c^2} \right) \right].$$

The factor 6 is included so that both $I(\nu)$ functions considered here have the same total intensity between 0 cm^{-1} and $\nu_c \text{ cm}^{-1}$.

Substituting into Eq. (2), we obtain

$$F'_2(x) = I_0 v_c \left[1 + \frac{3}{y^2} \left(\frac{\sin y}{y} - \frac{\cos y + 1}{2} \right) \right]$$

with y defined as before.

For small values of x , $F'_1(x)$ and $F'_2(x)$ fluctuate rapidly, but the amplitudes are damped such that both $F'(x)$ curves approach asymptotically the horizontal straight line, $F'(x) = I_0 v_c$. The $F'_1(x)$ falls off as $(2\pi x v_c)^{-1}$, whereas $F'_2(x)$ falls off more sharply, approximately as $(2\pi x v_c)^{-2}$. In each case, however, after only moderate x has been reached, the $F'(x)$ curves become essentially straight lines. This is what is observed experimentally. The $F'_1(x)$ and $F'_2(x)$ are shown in Fig. 1, with $v_c = 100 \text{ cm}^{-1}$. Thus when an absorbing medium, such as a gas whose molecules have a dipole moment, is placed in the infrared beam, any variation of the $F(x)$ curve from a straight line (for intermediate and large values of x) may be attributed to the absorbing medium.

Now let us consider what sort of interferogram a single absorption line with Lorentz line shape would look like. Let

$$I(v) = I_0(v) e^{-Y(v)}$$

where

$$Y(v) = \frac{A\epsilon l}{(v - v_0)^2 + \epsilon^2}$$

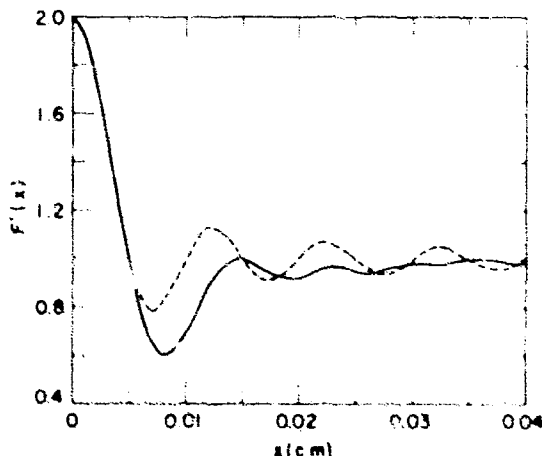


Fig. 1. Interferograms for "source-like" $I(v)$. Line curve $I(v) = 6I_0 [(v/v_c) - (v^2/v_c^2)]$, dotted curve $I(v) = I_0$, a constant. $F'(x)$ is plotted in units of $I_0 v_c$ ($v_c = 100 \text{ cm}^{-1}$).

where A is a constant (independent of ν), l the absorbing path length, ϵ the linewidth parameter (which for weak absorption is the half-width at half-maximum intensity), ν the wavenumber, and ν_0 the resonant wavenumber.

Then

$$F'(x) = \int I_0(\nu) e^{-\gamma(\nu)} d\nu + \int I_0(\nu) e^{-\gamma(\nu)} \cos 2\pi x \nu d\nu$$

Expanding the exponential in a power series we obtain

$$\begin{aligned} F'(x) &= \int I_0(\nu) d\nu + \int I_0(\nu) \cos 2\pi x \nu d\nu + \int I_0(\nu) \sum_{m=1}^{\infty} \frac{(-\gamma)^m}{m!} d\nu \\ &\quad + \int I_0(\nu) \sum_{m=1}^{\infty} \frac{(-\gamma)^m}{m!} \cos 2\pi x \nu d\nu \end{aligned}$$

The first and second integrals are merely the source interferogram. As discussed previously, this yields essentially a constant contribution to $F'(x)$ for intermediate and large values of x . The third integral is a constant and represents the intensity removed from the beam as a result of absorption. The fourth integral will give the deviation of the interferogram from a straight line at intermediate and large values of x and thus information about the absorbing line.

Now in order to avoid overly cumbersome mathematical expressions let us simplify the above expression by neglecting all except the first terms in the summation. A more general treatment may be found in the literature (Ref. 22). This will be a good approximation for weakly absorbing lines and will yield a qualitative picture for absorption lines of similar shape. Therefore

$$F'(x) = F'_s(x) - \int \frac{I_o(v)A\epsilon l}{(v - v_o)^2 + \epsilon^2} dv - \int \frac{I_o(v)A\epsilon l}{(v - v_o)^2 + \epsilon^2} \cos 2\pi x v dv$$

where $F'_s(x)$ is the interferogram of the source.

Now $[(v - v_o)^2 + \epsilon^2]^{-1}$ is a sharply peaked function (as long as $v_o \gg \epsilon$) and has large values in the region $v \approx v_o$. Thus small error will be made in the following approximations: (a) set $I_o(v) \approx I_o(v_o)$, and (b) extend the limits of integration to $\pm \infty$, so

$$\begin{aligned} F'(x) &= F'_s(x) - I_o(v_o)A\epsilon l \left[\int_{-\infty}^{\infty} \frac{dv}{(v - v_o)^2 + \epsilon^2} + \int_{-\infty}^{\infty} \frac{\cos 2\pi x v_o dv}{(v - v_o)^2 + \epsilon^2} \right] \\ &= F'_s(x) - I_o(v_o)A\epsilon l \pi (1 + e^{-2\pi x \epsilon}) \cos 2\pi x v_o \end{aligned} \quad (7)$$

The effect of the single absorption line is given by the second term and its dependence on x by the term in brackets, as shown in Fig. 2. The amplitude of this factor, $I_o(v_o)A\epsilon l\pi$, is the intensity removed from the beam by the absorbing line, and in general it is quite small in comparison with the total incident intensity. Thus, $F'_s(x)$ will be only slightly modified by a single absorption line. As an illustration, for $l = 15$ cm, $p \approx 400$ Torr, the FIR absorption spectrum of CO between 15 and 115 cm^{-1} (~ 20 lines, not just one) removes less than 5% of the incident intensity. This means that the variation of $F'(x)$ about its average value $(1/2)F'(0)$ will be quite small (less than 5% at best) and according to the above treatment, if the lines have approximately Lorentzian shape, will decay exponentially. Making ϵ smaller, which can be done for CO by lowering the pressure, will make the argument of the damping exponential smaller, but of course the integrated intensity will also become smaller ($A \propto \text{pressure}$). This is a characteristic problem

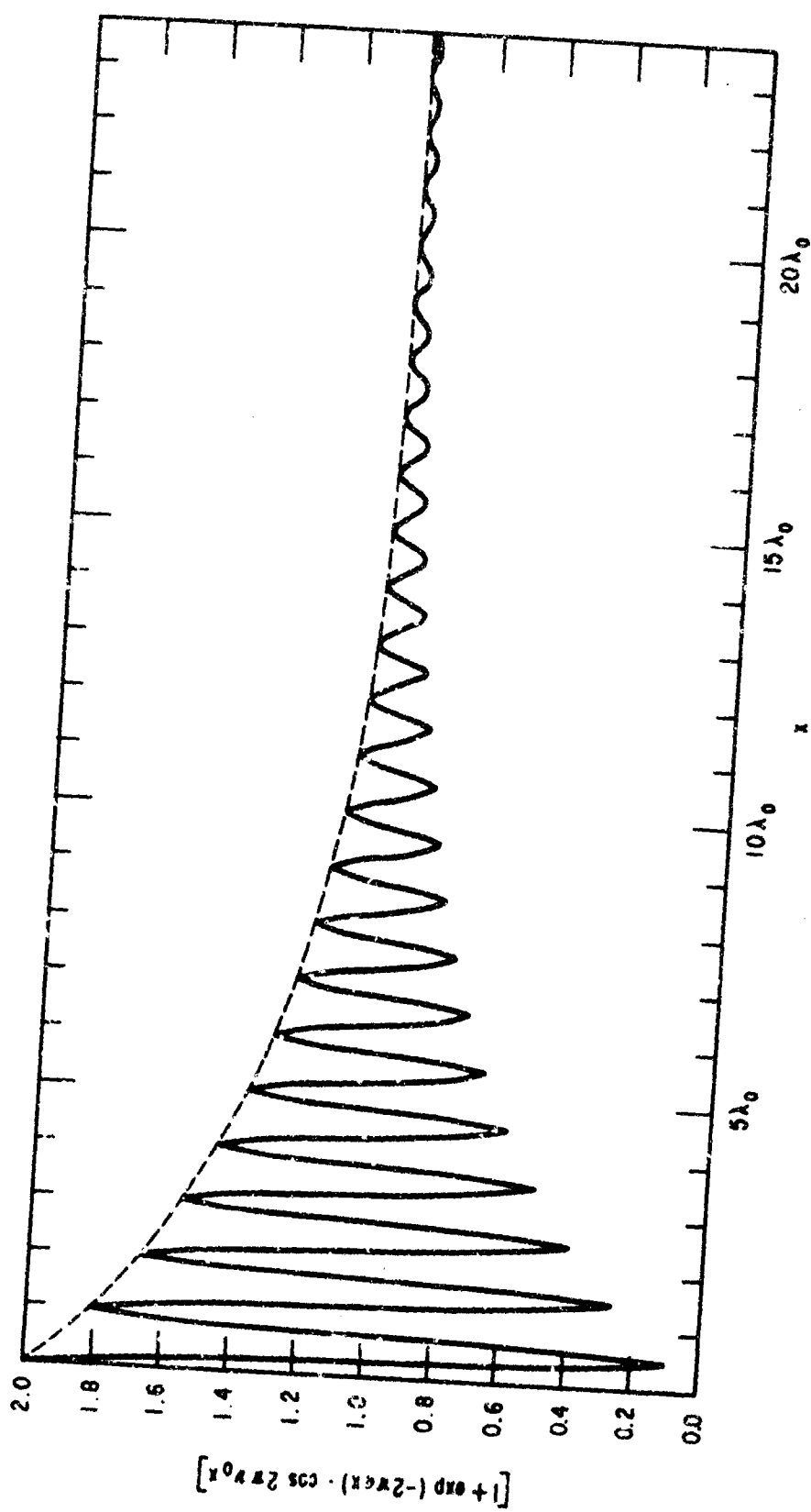


Fig. 2. Interferogram of a line with a Lorentz shape.

of absorption interferometry and is called the "dynamic range" problem. How it has been solved is discussed in Section III.

Another simple example is the interferogram generated by a spectrum which consists of evenly spaced (in cm^{-1}) lines. The theoretical interferograms can be obtained by summing over the absorption line contribution in Eq. (7). Let the ν_0 's be designated ν_1 (lowest), $\nu_2, \nu_3, \dots, \nu_m$ (highest) and be equally spaced such that

$$\nu_1 = \nu_2 - \nu_1 = \nu_3 - \nu_2 = \dots = \nu_m - \nu_{m-1} = \delta\nu$$

or in terms of λ

$$\lambda_1 = \frac{1}{2}\lambda_2 = \frac{1}{3}\lambda_3 = \dots = \frac{1}{m}\lambda_m$$

The varying part of the interferogram will be a sum of contributions such as that shown in Fig. 2. When $x = \lambda_1 (=1/\delta\nu)$, then $x = 2\lambda_2 = 3\lambda_3 = \dots = m\lambda_m$, so all the cosine contributions will have a maximum. Likewise, when $x = 2\lambda_1 (=2/\delta\nu)$, then also $x = 4\lambda_2 = 6\lambda_3 = \dots = 2m\lambda_m$, and again all the cosines will have their maximum value. The same situation occurs at $x = 3\lambda_1, 4\lambda_1, \dots$. Thus, significant variations of $F'(x)$ about its average value ($1/2$) $F'(0)$ are expected when $x = m\lambda_1 = m/\delta\nu$. Such features, called signatures in interferometry, have been observed in the FIR interferograms of linear (Ref. 23) and diatomic (Ref. 24) molecules. This will be further amplified and discussed in Section IV.

We now come to the question of finite or truncated interferograms. For this topic it is natural to inquire what is the scanning function of a two-beam interferometer. The scanning function of a spectrometer or interferometer may be thought of as the output spectrum of the instrument when a monochromatic line is the input. Thus

$$I(v) = \delta(v_0)$$

and

$$F(x) = \int \delta(v_0) \cos 2\pi x v dv = \cos 2\pi x v_0$$

Now suppose we FCT $F(x)$ out to $x = L$, rather than $x \rightarrow \infty$. Then

$$I_L(v) = L \left[\frac{\sin 2\pi L(v - v_0)}{2\pi L(v - v_0)} \right] \equiv L \operatorname{sinc} 2\pi L(v - v_0) \quad (8)$$

and this is the scanning function of a two-beam interferometer. This is shown in Fig. 3. The $I_L(v)$ does have its largest maxima at $v = v_0$, but its resemblance to $\delta(v_0)$ is not too good for finite L .⁴ Perhaps most annoying (to the spectroscopist at any rate) are the extraneous sidelobes, or feet, whose amplitudes decay as $\sim (v - v_0)^{-1}$. The two sidelobes adjacent to the central maxima are not small and, as seen in Fig. 3, are about (first minima to second maximum) 34% of the peak value at $v = v_0$. The width of the scanning function is determined by L and the first minima are at $v - v_0 \approx \pm 0.715(L)^{-1}$. The relative amplitudes of the sidelobes do not depend on L . In contrast, the scanning function for a conventional grating spectrometer is of the form $(\operatorname{sinc})^2$ which has much smaller sidelobes.

We are now in a position to discuss resolution. Resolution is a somewhat arbitrary criterion, usually stated in terms of how well two equally intense lines appear separated in an output spectrum. The Rayleigh criterion for a diffraction grating spectrometer is that two lines of equal intensity

⁴To within a multiplicative factor $I_L(v) \rightarrow \delta(v_0)$ as $L \rightarrow \infty$. See W. Heitler, Quantum Theory of Radiation (Clarendon Press, Oxford, 1954), Chapter II, page 66.

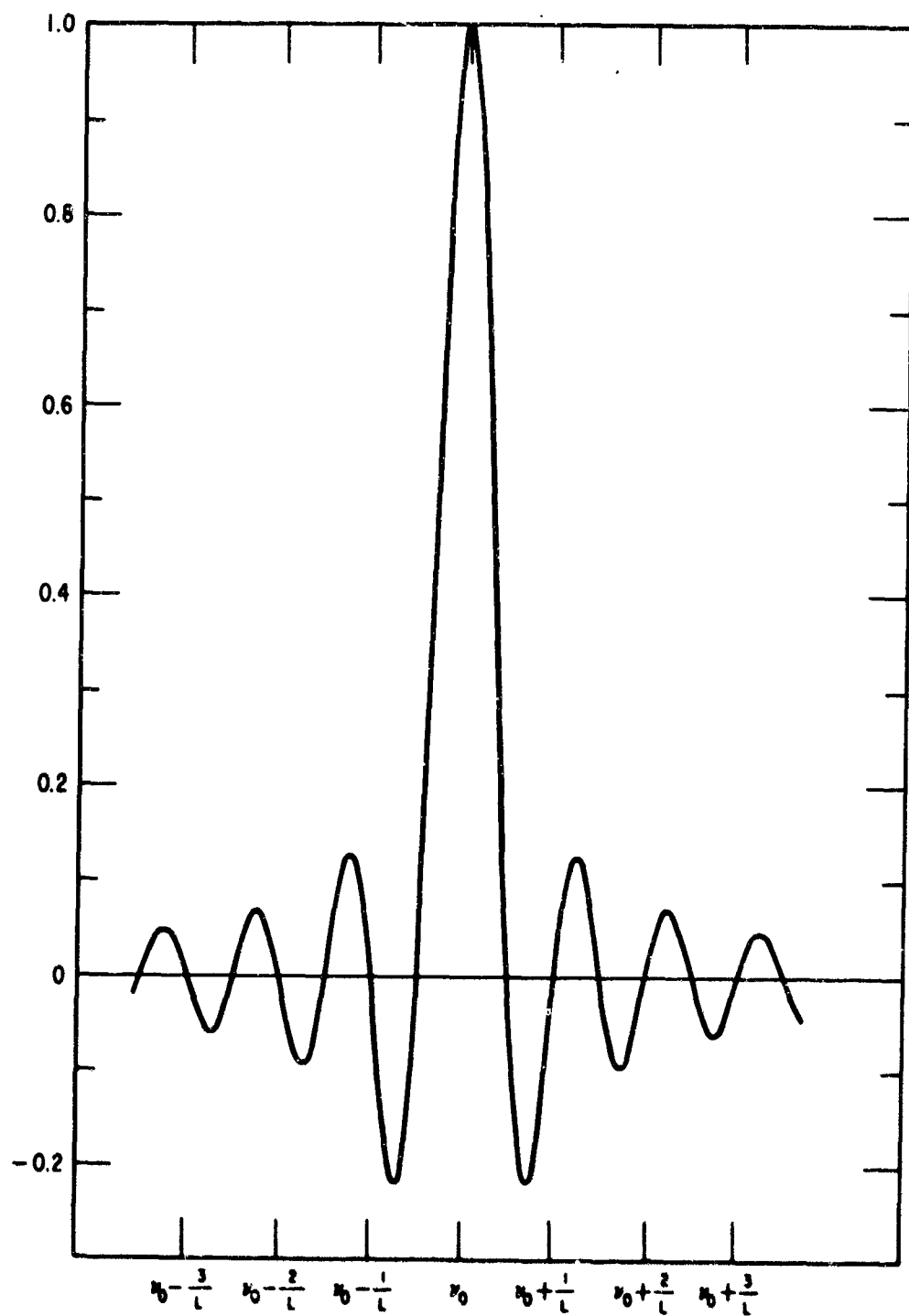


Fig. 3. The scanning function of a two-beam interferometer.

should be considered to be just resolved when the principal intensity maximum of one coincides with first intensity minimum of the other. On this basis there will be a dip of intensity of 18.9% between the two lines. Figure 4 shows two such lines separated by $\Delta\nu \approx 0.715(L)^{-1}$, i.e., applying the first part of the Rayleigh criterion to two lines as would be seen by a two-beam interferometer. The dip in intensity between the two lines is considerably less than 18.9%. Strong and Vanasse (Ref. 12) have introduced the modular resolution criterion and it is

$$(\Delta\nu)_{\text{modular}} = L^{-1} \quad (9)$$

This, of course, is more conservative than $\Delta\nu = 0.715(L)^{-1}$, and two lines separated by this $\Delta\nu$ are shown in Fig. 5. The dip in intensity between the two lines is greater than 18.9%. Additional reasons for preferring the modular resolution criterion are given later in Section IV.

The sidelobe problem appears to be serious, especially as compared with its almost negligible importance in a grating spectrometer. It is possible to suppress these sidelobes by apodization. Essentially, apodization consists of multiplying the interferogram function by a monotonically decreasing function of x such that $F(L) = 0$. The theory and practice of apodization has been discussed by Filler (Ref. 25). One of the disadvantages of apodization is lower resolution.

Indiscriminate apodization can be, and usually is, useless. It is instructive to consider what effect the scanning function has upon a line of finite width (lines with zero width are quite unphysical). One can show by convolution theory that a line whose shape is given by $f(v)$ will appear in the output spectrum as $f(v)*S(v)$, i.e., the convolution of $f(v)$ with $S(v)$ as the scanning function. We shall again consider a line with a Lorentz shape.

$$I(v) = \frac{A\epsilon}{(v - v_0)^2 + \epsilon^2}$$

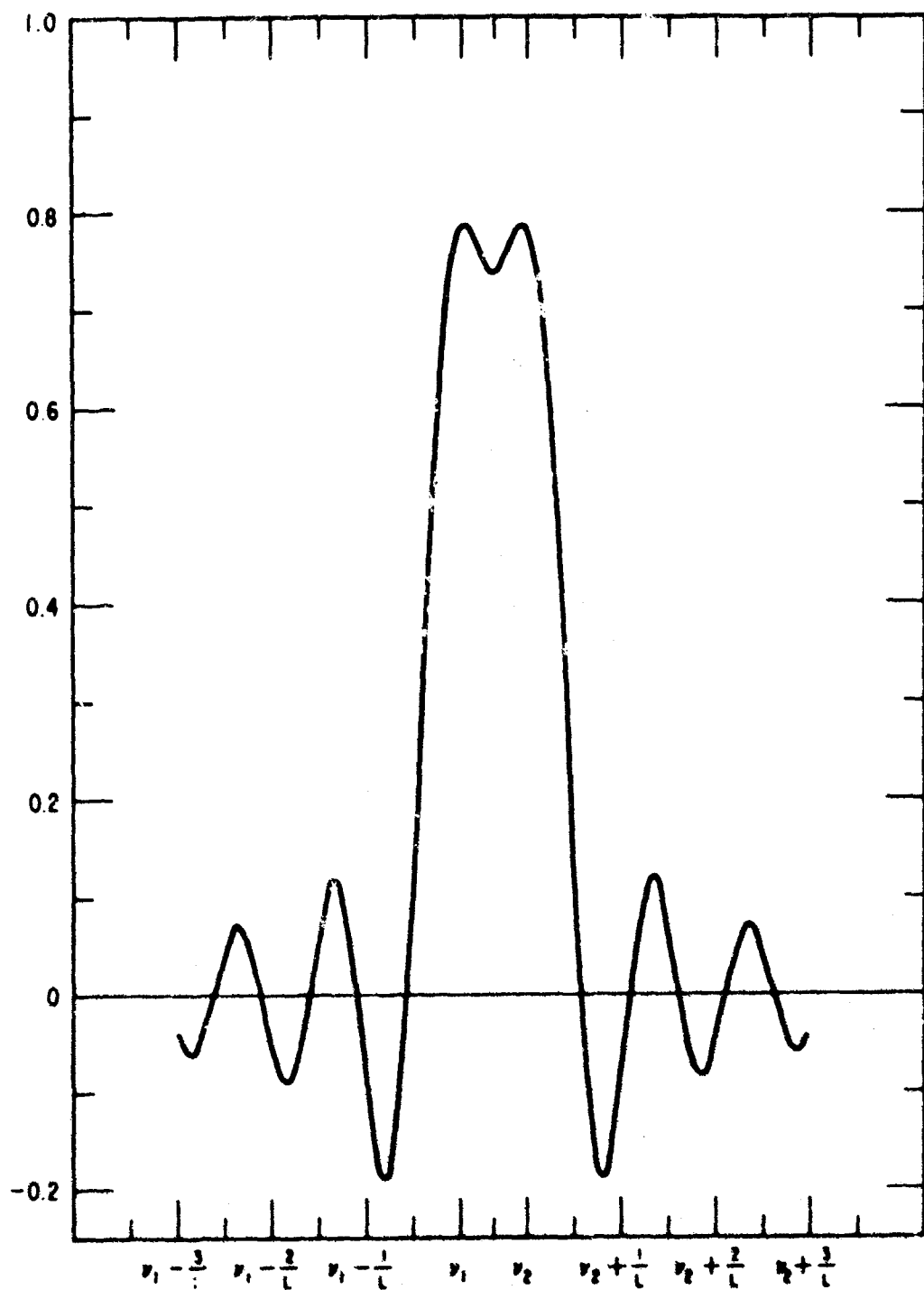


Fig. 4. Two δ function lines separated by $0.715(L)^{-1}$ as would be seen by a two-beam interferometer which has been scanned out to $x_{\max} = L$.

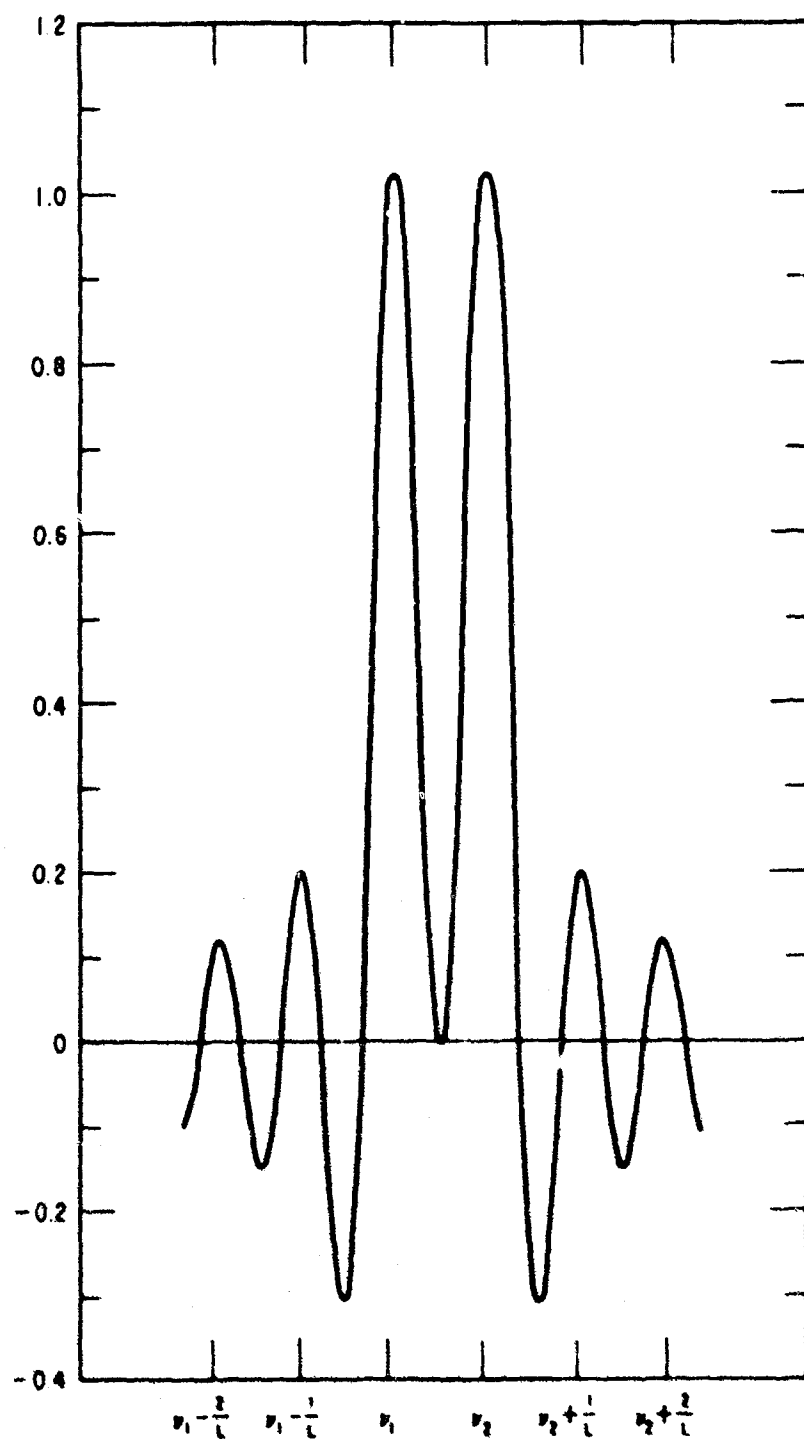


Fig. 5. Two δ function lines separated by $(L)^{-1}$ as would be seen by a two-beam interferometer which has been scanned out to $x_{\max} = L$.

$$F(x) = \pi A e^{-2\pi x \epsilon} \cos 2\pi x_0$$

Now if $F(x)$ is FCT (or $I(v)$ is convolved with $S(v)$) out to $x = L$, we obtain

$$I_L(v) = I(v) \left\{ 1 - e^{-2\pi L \epsilon} \left[\cos 2\pi L(v - v_0) - \left(\frac{v - v_0}{\epsilon} \right) \sin 2\pi L(v - v_0) \right] \right\} \quad (10)$$

When $L \rightarrow \infty$, it is obvious $I_L(v) \rightarrow I(v)$ as it should. Also to within a multiplicative constant, $I(v) \rightarrow \delta(v_0)$ as $\epsilon \rightarrow 0$ and $I_L(v) \rightarrow \text{sinc } 2\pi L(v - v_0)$ as $\epsilon \rightarrow 0$. For finite L , the exponential term and the term it multiplies describes the distortion of the line from its true shape. Figures 6, 7, and 8 are plots of Eq. (10) for $L\epsilon = \infty, 3/4$, and $1/2$. On the scale of these plots, the case $L\epsilon = 1$ would appear identical to $L\epsilon = \infty$. In general, the maximum intensity of $I_L(v) = I_L(v_0)$ differs from $I(v_0)$ as

$$I_L(v_0) = I(v_0) (1 - e^{-2\pi L \epsilon})$$

(On the graphs, A is chosen such that $I(v_0) = 1$.) For $L\epsilon = 3/4$, the feet are just becoming discernible and the maximum intensity, $I_L(v_0)$ differs from $I(v_0)$ by $\sim 0.8\%$. For $L\epsilon = 1/2$, the sidelobes are now quite apparent and $I_L(v_0)$ is $\sim 4.6\%$ weaker than $I(v_0)$.

Let us define

$$\Delta I(v) = I(v) - I_L(v)$$

and furthermore let

v_1 = the value of v where $\Delta I(v)$ has its first minima, and

v_2 = the value of v where $\Delta I(v)$ has its second maxima (the first maxima is of course at $v = v_0$).

Now we define

$$I_F = \Delta I(\nu_2) - \Delta I(\nu_1)$$

so that I_F measures the maximum sidelobe intensity. A plot of $I_L(\nu_0)/I_F$ versus $L\epsilon$ is shown in Fig. 9. This curve rises quite steeply as a function of $L\epsilon$, i.e., as the width of the scanning function (governed by L) approaches ϵ , the sidelobe intensity decreases very rapidly. As an example of its usefulness, suppose the S/N in the spectrum is 100/1; then there is no point in making $I_L(\nu_0)/I_F$ much greater than 100/1, which means $L\epsilon \sim 0.81$. For $L\epsilon \sim 0.81$, the interferogram $e^{-2\pi x\epsilon} \cos 2\pi x\nu_0$ will be down to $e^{-2\pi(0.81)}$ of its value at $x = 0$, which is down by a factor of 162. The use of this curve when noise in the interferogram is considered is discussed in Section V.

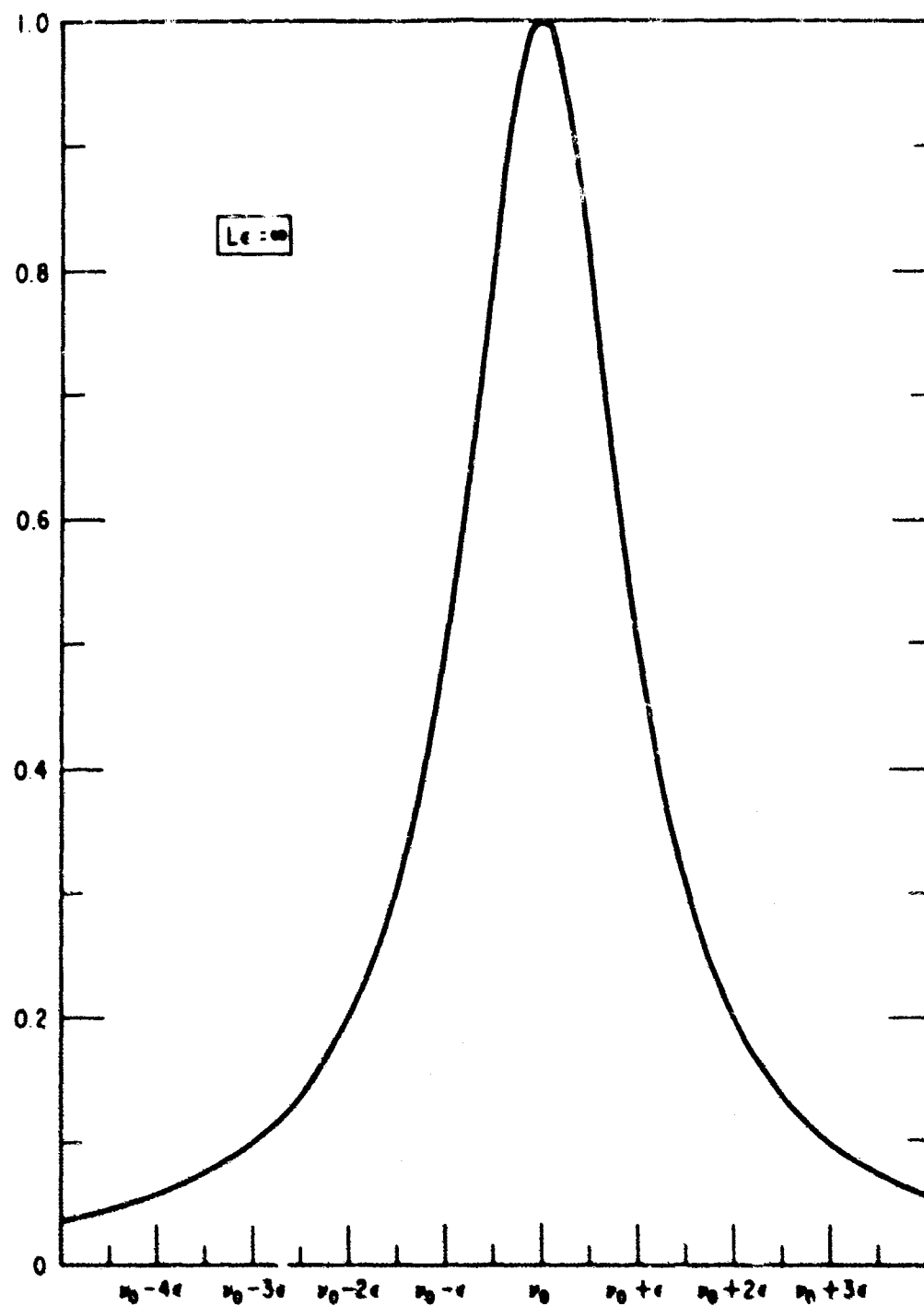


Fig. 6. The Lorentz line shape.

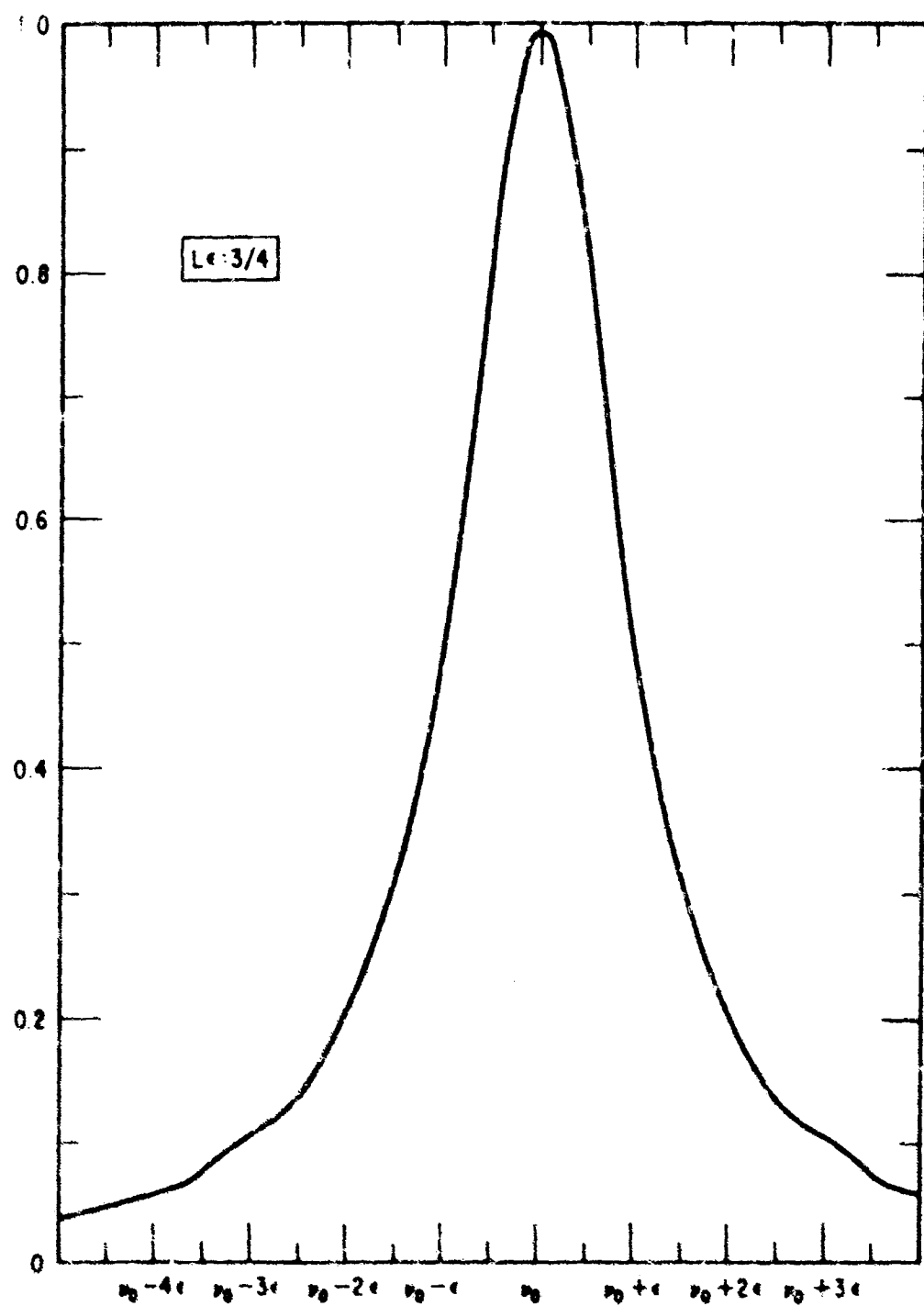


Fig. 7. Plot of $I_L(v)$ for a Lorentz line with $L\epsilon = 3/4$.

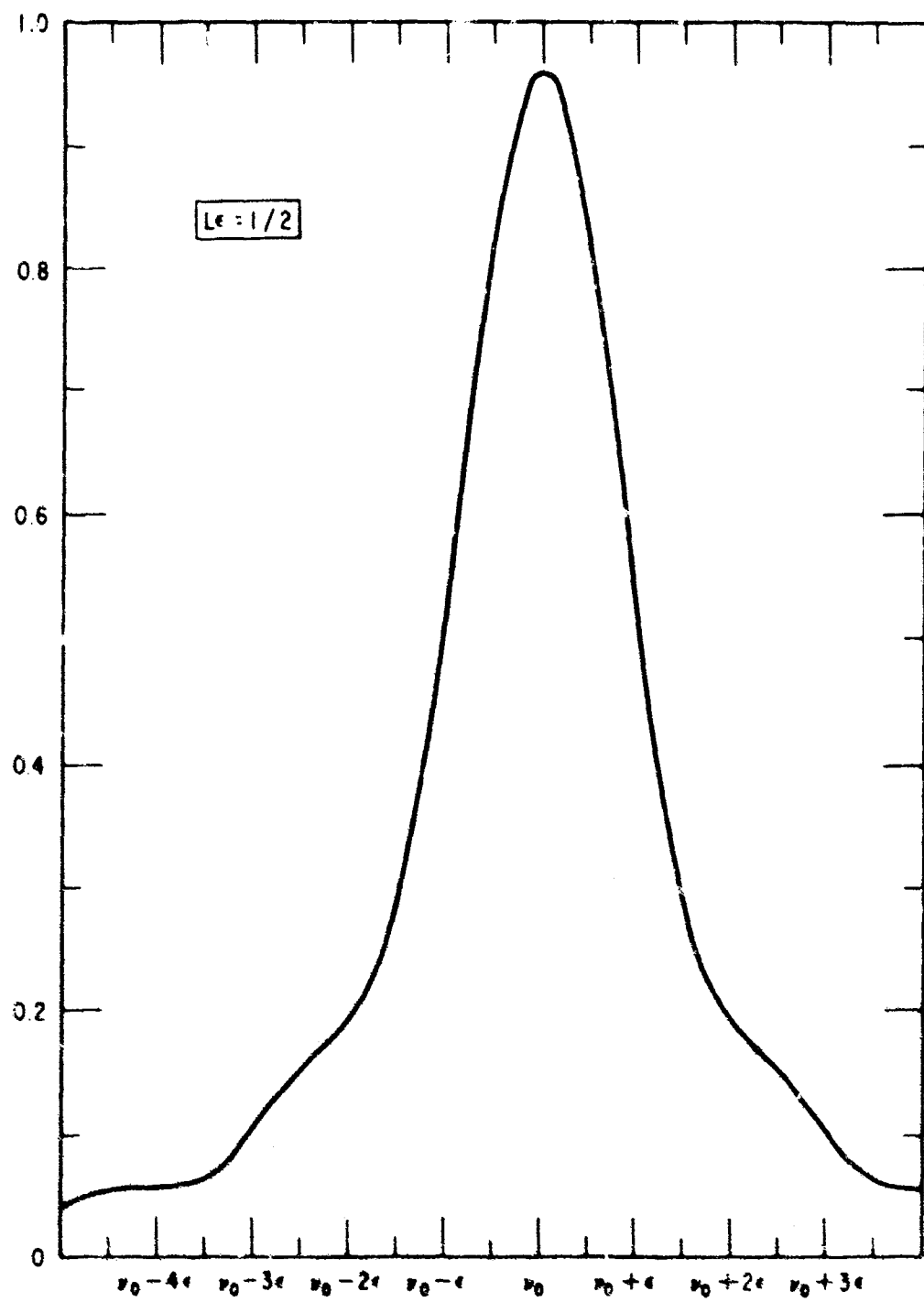


Fig. 8. Plot of $I_L(v)$ for a Lorentz line with $Le = 1/2$.

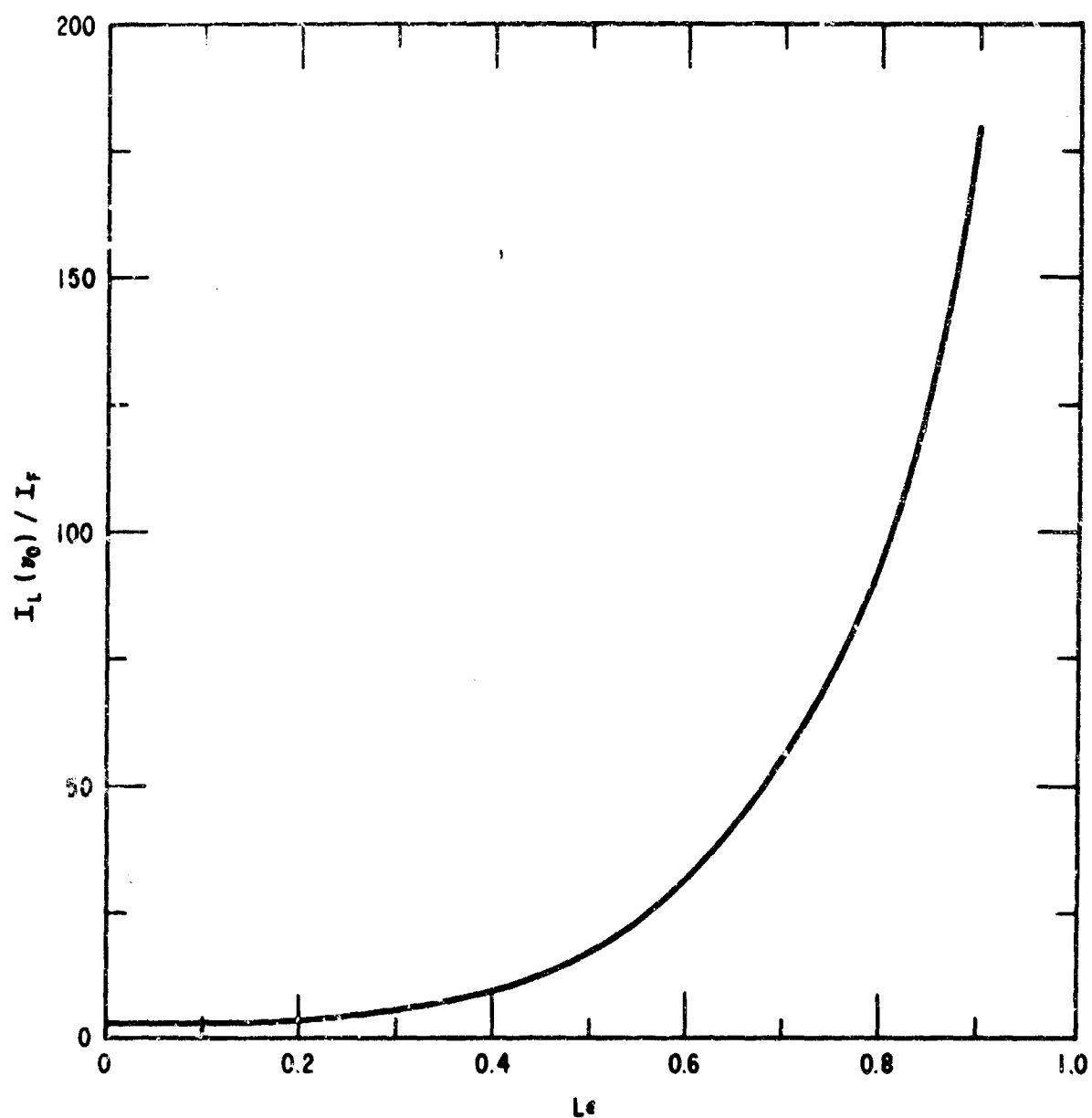


Fig. 9. Plot of $I_L(v_0)/I_F$ versus Le .

III. DESCRIPTION OF THE INSTRUMENT

A. OPTICS

The optical diagram of the lamellar grating interferometer is shown in Fig. 10. The source of radiation is a high-pressure, 85-W fused quartz

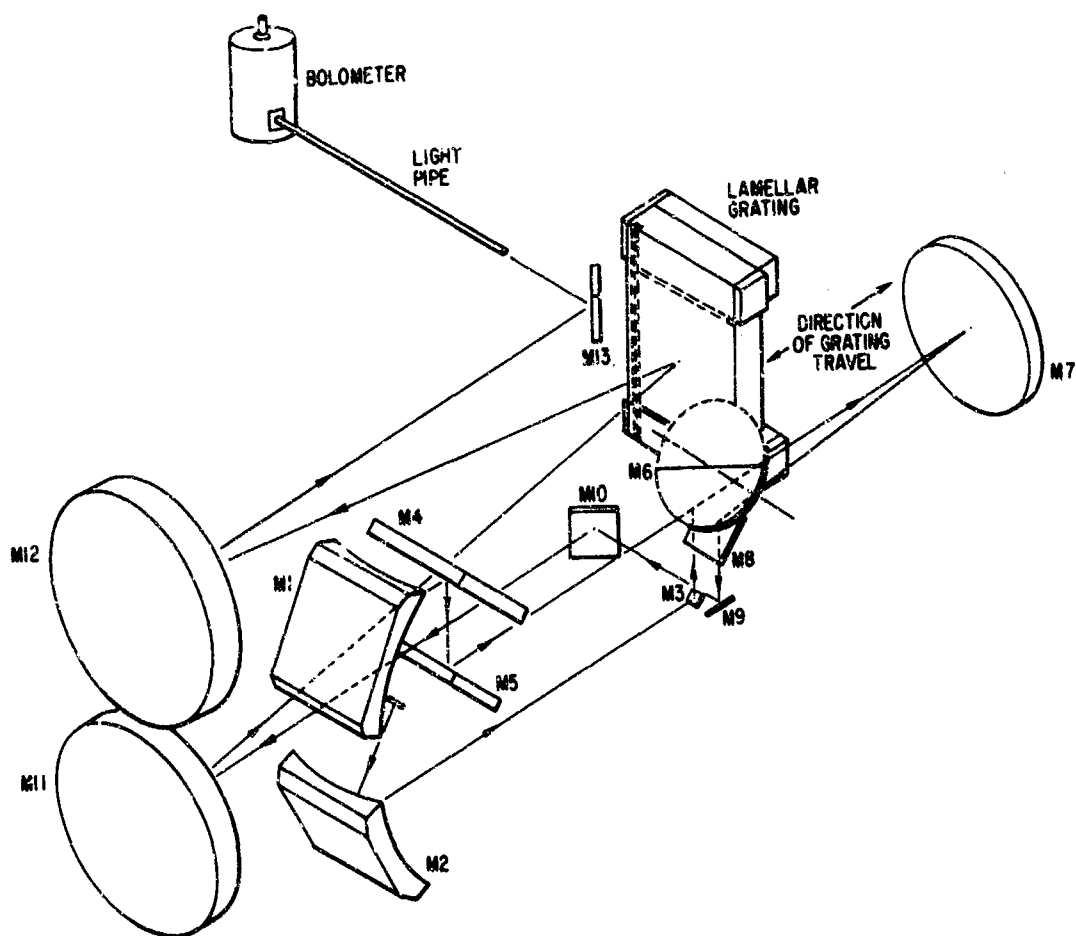


Fig. 10. Lamellar grating interferometer optical diagram.
The foci of the ellipsoids M_1 and M_2 are between
 M_5 and M_6 (sample beam) and at M_3 (reference
beam), respectively.

mercury arc lamp (G. E. H85A3) with the outer glass envelope removed. The arc is mounted in a water-cooled housing with two cutouts through which the reference and sample beams emerge. The two beams are caught and focused by two ellipsoidal mirrors M_1 and M_2 . The upper or sample beam is folded by two flats M_4 and M_5 and then passed through the sample chamber. Mirror M_5 is a polished aluminum flat to match the reflectance of the aluminum chopper wheel M_6 . The beam comes to a focus in the middle of the sample chamber allowing the use of minimum size samples. The focus is a circle of 0.95 cm diam. The lower or reference beam passes under the sample chamber and comes to a focus on the flat M_3 . Flat M_3 is located on a six-position slide assembly which allows changing between the mirror and any of five 2.5-cm diam samples for reflection studies from outside the tank without breaking the vacuum in the chamber. The flat M_3 folds up the reference beam perpendicular to the sample beam. The two beams are then recombined by the polished aluminum semicircular chopper mirror M_6 which rotates at 19 cps. To match precisely the intensities of the two beams, motorized iris diaphragms have been placed in equivalent positions in both beams approximately 18 cm before the first focus.

Mirror M_7 is a 33-cm diam spherical mirror which refocuses the combined beams. A limiting aperture, which reduces the angular spread of the beam by a factor of 2, can be moved into place in front of M_7 from outside the tank. This feature is of great use in studies of solid samples. After striking M_8 and M_9 , the beam is refocused on the circular entrance aperture (not shown in the figure) of the interferometer proper. The size of the aperture is determined by the high-frequency radiation cutoff of the system (Ref. 12).

The interferometer optics consist of two 45.7-cm diam spherical mirrors and the lamellar grating. The two spherical mirrors are arrayed in a Czerny-Turner configuration which allows the grating to be used in parallel light in the zeroth order.

The lamellar grating consists of two sets of interleaving plane mirrors, as shown in Fig. 11. There are 24 facets in each set, each facet being 0.635 cm wide and 30.5 cm long, giving a total area of 30.5×30.5 cm for the grating. The grating is made of Pyrex.⁵ The individual facets of each grating are flat and coplanar to two fringes of the 5461 Å line of Hg, except for the outside facets of each grating, which deviate by about four fringes. These four facets have been blanked off to eliminate distortions in the interferograms caused by their optical imperfections.

After the optical path difference has been introduced by the grating, the beam is reflected to the second Czerny-Turner mirror, which after being folded by the diagonal flat M_{13} (scatter grating), refocuses it on the exit aperture mounted on the end of a light pipe. Flat M_{13} is adjustable from outside the tank to permit the final alignment to be made in vacuum. This is desirable because nearly all the FIR energy is absorbed by water vapor in the air. The size of the exit aperture is the same as the entrance aperture. The circular light pipe, 65 cm in length, takes the beam to the wall of the vacuum tank where a gallium-doped germanium bolometer (Texas Instruments) is mounted. The detector operates at 4.2°K and has a sensitive area of 5×5 mm.

One of the severe problems of the FIR is radiation purity. The mercury arc lamp emits orders of magnitude more energy in the ultraviolet (UV), visible, and near-IR. Eliminating this high-frequency radiation requires an elaborate array of transmission and reflection filters. However, in interferometry the problem is not nearly as difficult as in conventional dispersive spectroscopy. Filtering is accomplished in this instrument by the following means: At positions M_9 and M_{13} , coarse (<20 lines/mm) gratings are placed, which provide the high-frequency cutoff filtering of the source radiation. Wavelengths shorter than approximately 1.5 times the

⁵ Manufactured by Davidson Optronics of West Covina, Calif.



Fig. 11. Front view of the lamellar grating. At the right is the chopper assembly, the back side of M₈ and the six-position slide assembly on which M₃ is mounted. Mirror M₁₀ is just below the grating; M₁₃, which is replaced by a scatter grating after alignment, is above the grating. Also shown (in front of M₃) are the filter wheel and variable diaphragm.

blaze wavelength of the grating are thrown out of the beam at the blaze angle of the grating. To longer wavelengths, the gratings appear as plane mirrors. By changing these gratings, the high-frequency cutoff can be changed. Two identical gratings in series sharpen the cutoff. Various sets of gratings are available to vary the high-frequency cutoff. In addition to filtering by the two scatter plate gratings, there is filtering by black polyethylene and crystalline quartz. A sheet of black polyethylene is located between the source and chopper in front of the sample area on the grating side of the source housing after mirrors M_5 and M_2 . This cuts down the UV and visible light entering the sample chamber and helps to eliminate the sometimes deleterious effects of UV light on samples under study. If gas samples are to be studied, they must be contained in a conventional gas cell that has windows offering two more filtering positions. Wedged crystalline quartz windows are used. To compensate for the absorption in the sample beam, two nearly identical pieces of crystalline quartz are placed in the reference beam. These are located between M_3 and M_6 on a four-position filter wheel controlled from outside the tank. In the other three positions of the filter wheel are an opaque shutter for blanking off the reference beam, an open hole for studies where the filtering of crystalline quartz is not wanted, and one additional space where any other compensation filter can be placed (e.g., polyethylene). The crystalline quartz absorbs the intermediate IR radiation of the source. The quartz pieces in the reference beam are slightly thinner -- by a few hundredths of a millimeter -- than those on the sample cells. The four-position filter wheel can be rotated about an axis perpendicular to the optic axis. This allows the effective thickness of the filters to be varied to obtain a precise equivalence of both beams, which is necessary to ensure complete balance of the spectral transmission of both beams. Slight deviations in balance lead to anomalies in intensity for the region of zero optical path difference.

Figure 11 shows the lamellar grating and mirrors M_3 , M_6 , M_8 , M_{10} and M_{13} . Figure 12 shows a side view of the interferometer. Figure 13



Fig. 12. Side view of the interferometer. At the left is the source housing and optics. The side view of the chopper is in the center of the figure. A "swing-away" limiting diaphragm can be seen in front of mirror M_7 . The interferometer is on a dolly with rails matching those in the vacuum tank (extreme left).

gives an overall view of the interferometer. The sample chamber slides into position between the source housing and the chopper wheel. The sample chamber has been put in place on the left side and the light pipe attached to the bolometer on the right side. The bolometer is located in an elbow just outside the hole from which the light pipe is protruding. All electrical and cooling water connections are made by vacuum-tight connectors in the bulkhead at the lower left.



Fig. 13. The interferometer in place in the vacuum tank. The light pipe can be seen protruding from the right-hand side of the chamber wall. The sample chamber is in place on the left side (appears black). The rails upon which the instrument rides are at the bottom and the electrical cooling water connections at the bottom left. The diameter of the vacuum tank is 1.68 m.

B. MECHANICS

The interferometer is mounted on a heavy steel box frame which is kinematically supported in a vacuum chamber. Thus deflections in the vacuum chamber walls will not alter the alignment of the optics.⁶ Evacuation is necessary to eliminate the strong water vapor absorption in the FIR. A 10-in. vacuum pump system can evacuate the chamber with all the apparatus inside to a pressure of 10^{-5} Torr in a few hours. Liquid-nitrogen trapping helps to remove the last traces of water vapor. Figure 14 shows the vacuum tank and the electronics console.



Fig. 14. Electronic console and vacuum tank

⁶The interferometer frame and mirror mounting were manufactured by American Astrophysics, Monrovia, Calif. The vacuum chamber was manufactured by Advance Tank and Manufacturing Company, Gardena, Calif.

The sample chamber can be isolated from the rest of the vacuum chamber by gate valves, which also function as ports through which the sample beam passes. With the gate valves closed, the sample chamber can be brought up to atmospheric pressure without impairing the vacuum in the main chamber for rapid change of samples. By closing one of the gate valves, single-beam interferograms of the reference beam can be obtained.

Access ports have been provided in the chamber walls to allow minor adjustments to be made from outside the chamber without rolling out the entire interferometer. The entire interferometer can be lowered down on wheels which ride on rails for servicing outside the chamber. A matching set of rails on a dolly mate with these rails, and the interferometer can be rolled out onto the dolly.

The entire vacuum chamber is vibrationally isolated from the floor by air suspension mounts under each of the six legs. These mounts isolate the chamber from vibration and shock down to a few cycles per second, eliminating spurious modulation due to external vibration.

The heart of the interferometer is the grating and its drive system. The lower set of facets of the grating is mounted on a movable platform suspended from a stationary platform holding the upper set of facets by three flexure hinges similar to those used by Strong (Ref. 13). These three hinges theoretically allow the lower platform to move in a perfectly parallel fashion with respect to the upper platform. Unfortunately, torsional oscillations and pitch, roll, and yaw errors of the order of 1 arc-deg necessitated further constraint. A flat, parallel-sided steel bar was installed below the lower platform. Two sets of ball race bearings were attached to the lower platform contacting the bar on its two vertical surfaces in order to eliminate torsional oscillations and reduce the pitch and yaw errors to less than ± 1 arc sec over 83 mm of travel. The errors in pitch and yaw are smoothly varying functions of the travel and are the worst at the extreme

end of the travel. The roll error, not important optically, was reduced to below the point where scraping of the facets was a danger. Since the platform rises through an arc about 0.1 in. during the travel, no restraint could be applied to this motion.

The grating platform is driven by a stepping motor which has 200 steps per revolution. The use of a stepping motor eliminates coasting and allows fine control of the drive by controlling the drive pulse rate to the motor. The stepping motor is geared down by very low backlash gears. The drive is transmitted to the grating platform by means of a precision lead screw and a pin riding on the driver nut. The entire platform is pre-loaded to ensure that the driver nut always rides on the same side of the lead screw. The drive system is capable of moving the grating platform in increments less than 0.5μ .

The relative position of the two sets of facets is measured by two separate systems, coarse and fine. The coarse system is capable of measuring the absolute position of the facets to within 1 mm over the entire path. The fine system can measure the absolute position of the facets to $\pm 1.5\mu$ over a 2 mm cycle. The two complementary systems together can measure the absolute position of the facets to $\pm 1.5\mu$ over the entire path. The position of zero optical path difference can be determined to an accuracy of better than $\pm 1.5\mu$. Relative to this position there is a constant precision of better than $\pm 1.5\mu$ for the location of any point over the entire range of travel. Unfortunately, the error varies in a periodic manner, which leads to apparent "ghosts" in the spectra obtained. This is discussed in Section V. A change in the method of measuring grating position is being planned, employing a laser interferometer.

The coarse system uses a synchro to determine the position of the grating platform. Approximately one revolution of the synchro corresponds to the full travel of the grating platform.

The fine system uses a linear metric Inductosyn scale (Farrand Controls, Inc., Valhalla, New York) to determine the position of the grating platform. This system, similar to those used on automatic milling machines, measures position by means of the inductive coupling between a stationary set and moving set of linear pole patterns. The moving set, supported on a glass blank, is mounted on the side of the grating platform. The stationary set is mounted on the grating platform immediately opposite the moving set on the side support member. The stationary set is 250 mm long, allowing its use over the full travel of the grating platform. Figure 15 shows a back view of the lamellar grating. The Inductosyn scales can be seen at the right and the drive system underneath the grating platform.

The grating platform has a maximum travel of 10.0 cm., of which 6.3 cm are useful, 0.3 cm on one side of the coplanar position of the grating and 8.0 cm on the other side. A travel of 8.0 cm is equivalent to an optical path difference of 16.0 cm, giving a modular resolution of 0.063 cm^{-1} . The intensity passed by the interferometer as a function of the optical path difference generated by the interferometer, known as the interferogram, is, in theory, symmetric about the coplanar position. In practice we have found this will not be true unless the incident parallel beam is strictly perpendicular to the grating facets in the azimuth perpendicular to the grating grooves. The incident beam does, of course, deviate from perpendicularity in the azimuth parallel to the grating grooves because of the Czerny-Turner optical system. This means that the optical path difference generated is not $2d$ (d = geometrical separation of two sets of facets), but rather $2d \cos \alpha$, where α is the angle between incident beam and the normal to the facet faces. The angle is approximately 9 deg and it is measured with a theodolite to an accuracy of ± 15 arc sec, which is sufficiently accurate to eliminate it as a source of systematic error in the measurement of optical path difference. The normals of the two sets of gratings are made parallel by adjusting the gratings in their mounts while monitoring the adjustment with a comparison autocollimator capable of detecting deviation from parallelism of less than

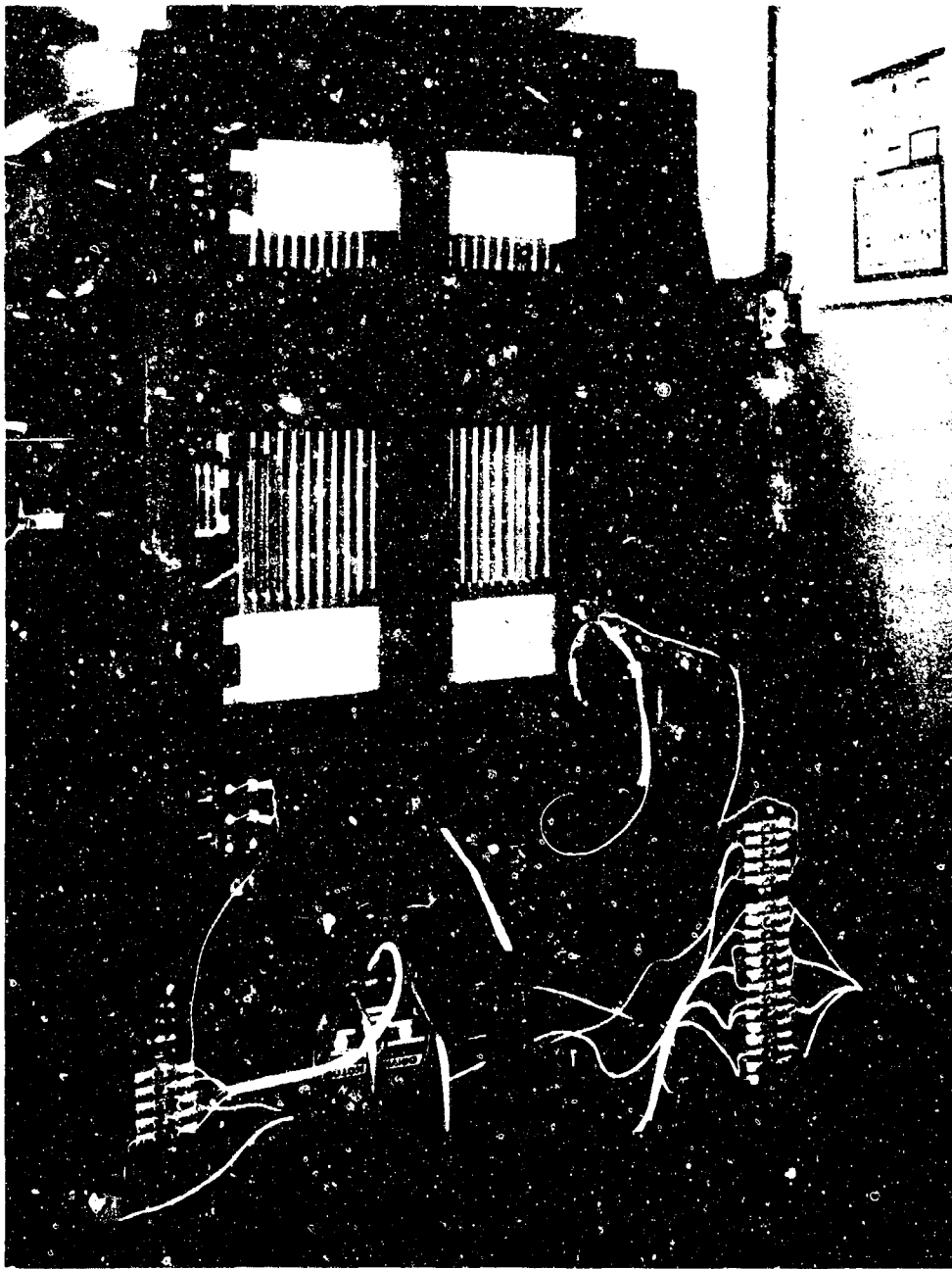


Fig. 15. Back view of lamellar grating. The flexure hinge supporting the movable platform is visible in the middle of the figure. There are two more flexure hinges in the front of the platform. On the right are the linear inductosyn plates. The drive system can be seen below the movable platform.

1 arc sec. The entire usable travel of the grating (8.3 cm) has been monitored and is rechecked after any adjustment with this comparison auto-collimator. With these precautions, very symmetric interferograms are obtained.

C. ELECTRONICS AND DATA RECORDING SYSTEM

The interferogram is not recorded continuously, but is sampled at equally spaced increments. The system is designed to sample at multiples of 10μ in optical path difference. The actual sampling interval is dictated by the highest frequency present and has been discussed previously.

The grating is allowed to sample each point for 2 to 8 sec to improve the S/N. During this time the output of the detector, suitably amplified and synchronously detected, is fed into a voltage-to-frequency converter that converts the voltage output linearly into a frequency which is then counted for the gate or sampling time. At the end of this time, the number of counts (0 to 9999) accumulated in the counter and the number of the point are punched on paper tape and printed on a digital printer. The grating then advances to the next point, and the process is repeated. This process is continued until the entire interferogram has been punched out on the paper tape. This tape output is then processed by the data reduction center and the Fourier cosine transformation is computed yielding the frequency spectrum. The digital printer output can be used to check for errors in the input data to the computer. Unfortunately, the use of punched paper tape has not been entirely satisfactory. We are in the process of converting to punched cards.

The grating drive system has been designed to operate in several different modes. These range from a completely manual mode to a completely automatic sampling mode. Other modes of the grating drive system are: the automatic mode, in which the grating will proceed to and remain at any position dialed into the controls; and the manual mode, in which the grating can be moved under direct control of the operator and thus is useful

for survey work.

Figure 16 is a block diagram of the grating drive and data recording systems. The strip chart record is used primarily for visual indication of performance during a run. The oscilloscope is used in a similar fashion.

The interferogram can be recorded either single-beam or double-beam. In double-beam operation, the outputs of the reference and sample beams are differenced automatically by the broadband ac preamplifier following the detector. This difference signal is recorded. In single-beam operation, one of the two beams is blanked off. As has been discussed previously, there is a problem of "dynamic range" in absorption interferometry. Double-beaming circumvents this problem. In double-beaming two beams are used, one of which passes through the sample cell (sample beam) and the other through a matched reference cell (reference beam); then the sample beam intensity (or signal) is subtracted from the reference beam intensity (or signal). When this is done, most of the information about the spectral distribution of energy from the source is lost, but such information may be recovered by a prior or subsequent recording of single-beam interferograms of the source alone. In practice, this is not difficult or inconvenient as the single-beam source interferogram need run out only to a 3- to 5-mm optical path difference and can be obtained in a time interval short compared with the higher resolution double-beam interferograms where the optical path difference typically runs out to 100 to 160 mm.

We write the appropriate equations for the intensity passed by the interferometer for the reference and sample beams:

$$\text{reference beam: } F'_r(x) = \frac{1}{2} F'_r(0) + \int_0^{v_c} I_r(v) \cos 2\pi xv dv$$

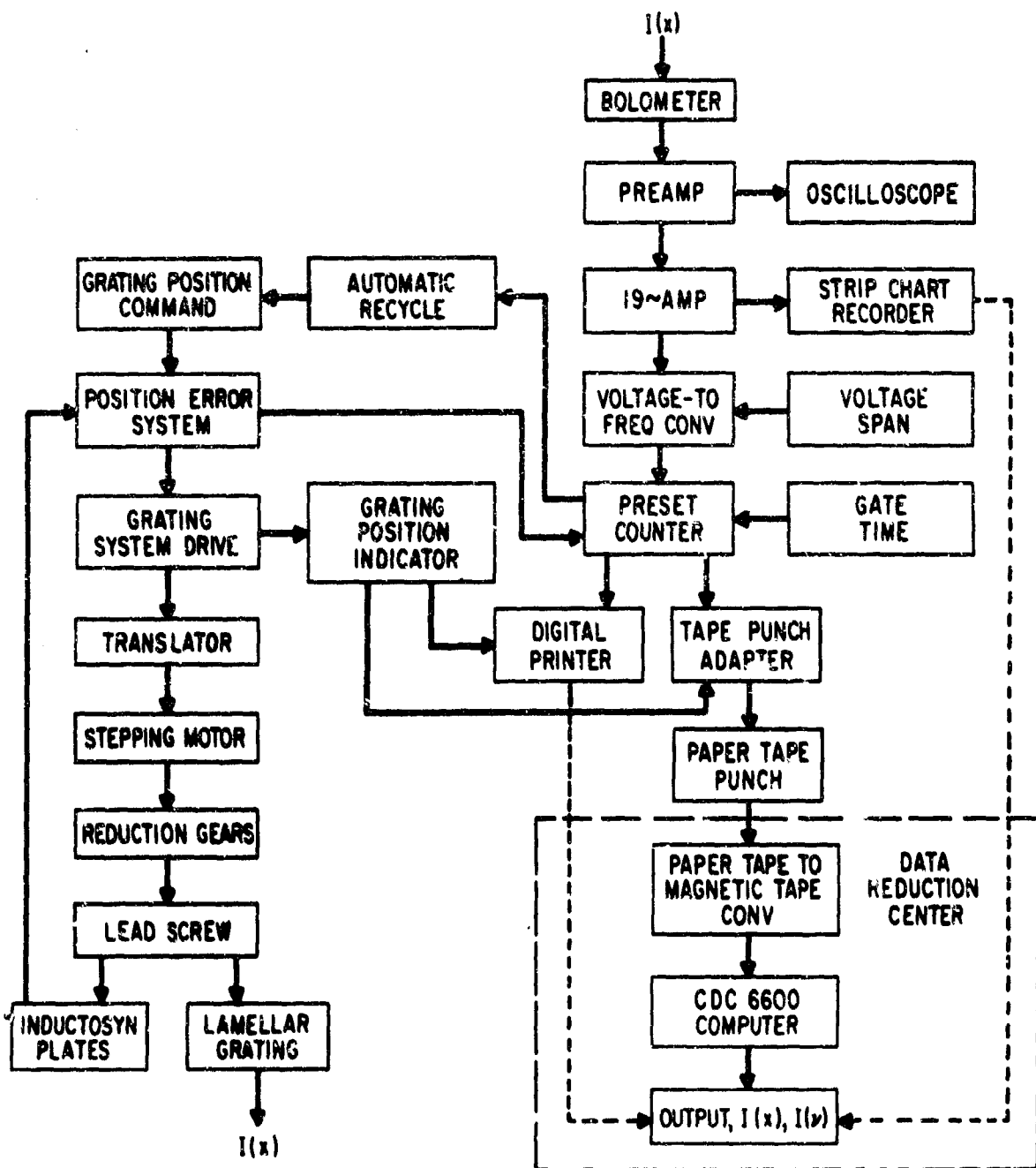


Fig. 16. Block diagram of lamellar grating interferometric system.

$$\text{sample beam: } F'_s(x) = \frac{1}{2} F'_s(0) + \int_0^{v_c} I_s(v) \cos 2\pi x v dv$$

where all the symbols have their previous meaning, and the subscripts r and s refer to the reference and sample beam, respectively. Differencing these equations and transposing the constant term to the left side, we obtain the double-beam interferogram function, $F_{r-s}(x)$:

$$F_{r-s}(x) \equiv F'_r(x) - F'_s(x) - \frac{1}{2} [F'_r(0) - F'_s(0)] = \int_0^{v_c} [I_r(v) - I_s(v)] \cos 2\pi x v dv \quad (11)$$

With matched beams and no sample, the detector will see essentially a dc signal that will not be amplified by the broadband ac preamplifier. In practice, because of the finite dimensions of the chopper (chopping is not done at a focus, see Fig. 10), there is ripple in the signal at the chopping frequency; however, the ripple is nearly 90 deg out of phase with any true signal and is largely filtered out by the phase lock amplifier.

To balance the beam, it is necessary to have matched spectral distribution of energy in the two beams. The total intensity is matched by a motorized iris in each beam (set back ~18 cm from the focus). Making the beams spectrally equivalent is more difficult to achieve since there must be equal filtering in each beam. For gas spectroscopy, a cell is required in the sample beam (usually quartz windows are used) so that an equivalent set of windows must be inserted in the reference beam. As mentioned previously, they may be rotated through small angles to provide a variable thickness of quartz. This is necessary because of wedging of windows (to prevent a troublesome channel spectrum) and optical inhomogeneity of the windows. In practice, perfect balance is not obtained, but with the above-mentioned modifications, near perfect balance can be obtained everywhere

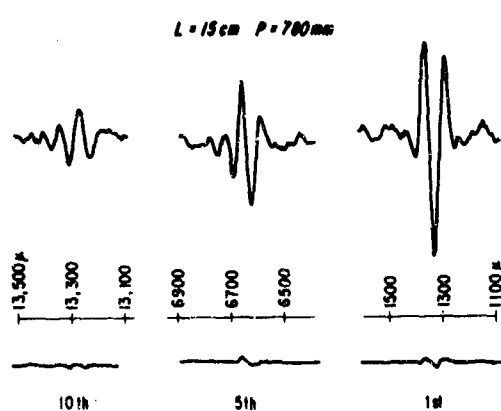


Fig. 17. Single-beam (lower) and double-beam (upper) interferometric features of the pure rotational spectrum of carbon monoxide.

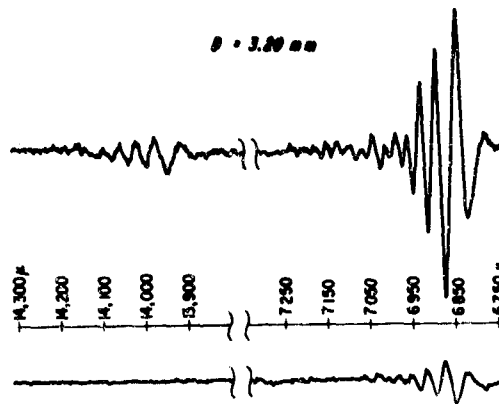


Fig. 18. Single-beam (lower) and double-beam (upper) interferometric features of the channel spectrum of a plane parallel window of crystalline quartz.

except in the region of $x = 0$. The unbalance there is ~ 20 times the noise level of the instrument.

The Fourier cosine transform of the left side of Eq. (11) will yield $[I_r(v) - I_s(v)]$, the difference between the reference beam spectrum and the sample beam spectrum. Thus an absorption spectrum appears as though it were an emission spectrum. As discussed above, the source (reference beam) spectrum can be easily obtained from single-beam runs.

The advantages of double-beam differencing over single-beam operation can be discussed in terms of Figs. 17 and 18, which compare single-beam and double-beam interferograms of carbon monoxide and quartz, all obtained with the central maximum at full scale. As can be seen, the "dynamic range" problem has been greatly alleviated by double-beam differencing.

IV. RESULTS

A. HIGH RESOLUTION SPECTROSCOPY OF GASES

1. CARBON MONOXIDE

A portion of the double-beam interferogram of the pure rotational spectrum of carbon monoxide (CO) is shown in Fig. 19. The absorption path length was 15 cm, and the pressure in the gas cell was 732 Torr. Had this interferogram been obtained single beam, keeping the central maxima full scale, the features due to the pure rotational spectra of CO would be down in intensity by a factor of ~ 15 .

Carbon monoxide is diatomic and therefore its pure rotational spectrum consists of almost evenly spaced lines (in cm^{-1}). As discussed in Section II, its pure rotational interferogram should have signatures spaced at equal intervals in x , the optical path difference. These signatures are apparent in Fig. 19, and the reciprocal of their spacing gives an average value of $2B_0$ (the separation of the lines in cm^{-1}). It is also seen that the signatures are distorting with larger optical path difference. Qualitatively, the first large minimum is losing amplitude and the second minimum

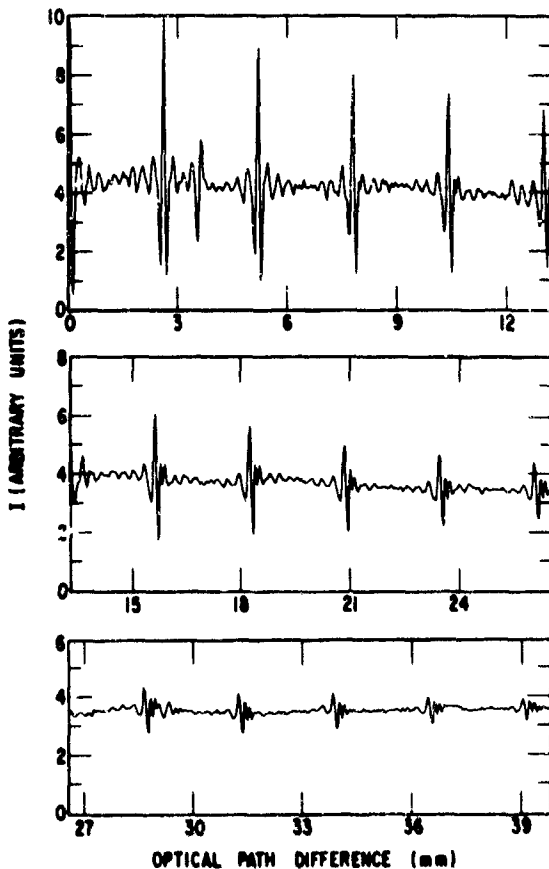


Fig. 19. The pure rotational double-beam interferogram of CO. The evenly spaced features are characteristic of diatomic and linear molecules.

is gaining, which is due to the fact that the pure rotational spectrum of CO is not made up of uniformly spaced lines, but rather lines that converge at higher wavenumber because of centrifugal distortion. This leads to the distortion of the signatures. If the lines had been diverging, the appropriate lobes would have lost and gained amplitude in the reverse order. Also, it is seen that signatures decay very rapidly in amplitude, over and above that caused by the distortion of the signatures, and this is due to the finite width of the absorption lines. In this interferogram \sim 25 signatures were observable before they were lost in the noise. At lower pressures one would of course expect to see more signatures (lines are narrower), and in fact at $p = 202$ Torr we have seen the 61st signature at $x \approx 16$ cm. Finally, there is an extra signature at $x \approx 3.6$ mm. That is caused by a channel spectrum generated in the quartz envelope of our source. It produces a cosine modulation in the spectrum. We have found that by proper editing of the interferogram, the channel spectrum can be eliminated. This problem is discussed further in Section V.

Figure 20 shows the result of performing the Fourier cosine transformation on the CO interferogram, that is, the pure rotational spectrum of CO between 19 and 100 cm^{-1} . The dashed line is the approximate envelope of the source spectrum (absorption goes up) and would be the place to which a 100% absorbing line would go. The variation in the base line is the channel spectrum mentioned previously. These features are quite broad and are not mistaken for the much sharper pure rotational lines of CO. The wave-numbers for the pure rotational spectrum of CO can be determined quite accurately from microwave (Ref. 26) and near-IR (Ref. 27) data; therefore, the measurement of this spectrum will not be discussed further, although it was very useful for calibration purposes.

It is, however, important to look at the line shape. As is well known in interferometry, if even a small error is made in the measurement of optical path differences (see Section V), shifts of the lines and serious

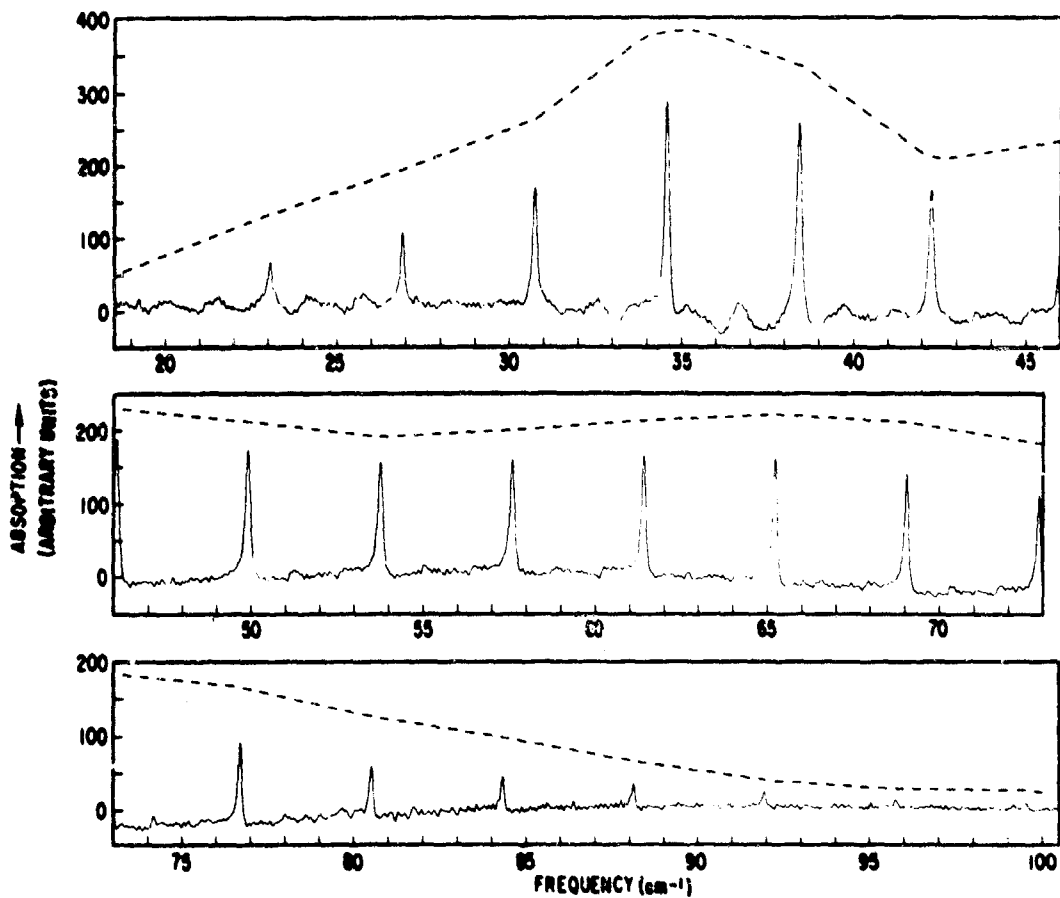


Fig. 20. The pure rotational spectrum of CO. The intensity scale is arbitrary, but the dashed line indicates the approximate intensity contour of the source. The cosinusoidal variation of the base line, especially noticeable at low wave-number, arises from the channel spectrum due to the lamp envelope.

distortion of line shapes occur. Figure 21 shows a typical result from our interferometer. Shown is the $J = 16 \rightarrow 17$ transition of CO. The open circles are the intensity points as given by the computer. The line looks and is very symmetric. In order to examine the line shape more closely, the first derivative of this line shape was computed (open squares). It has the expected shape, but there is about a 7% difference between the maxima and minima. If the line had been perfectly symmetric these would have been

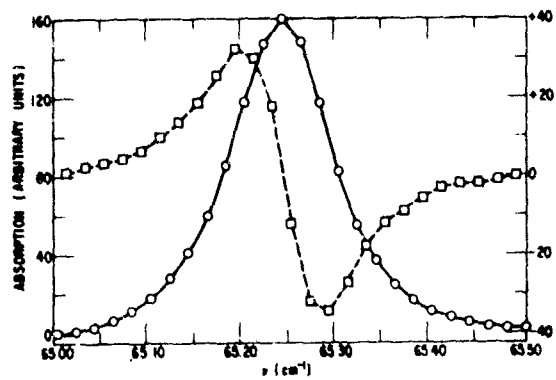


Fig. 21. The $J = 16 \rightarrow 17$ transition of CO. The circles are intensity points computed from the interferogram. The squares are the first derivative points computed from the intensity points.

equal but of opposite sign. This excellent symmetry of line shape and reasonably good first derivative shape have encouraged us to pursue line shape measurements, and this will be discussed later in this section. Also if the line were perfectly symmetric, the extrema of the first derivative curve would be equidistant (in cm^{-1}) from v_0 . These wavenumber intervals were measured for a number of CO spectra, and a typical set of results is shown in Table I.

The lines measured spanned the

region 26 to 81 cm^{-1} . In the first column, J_L is the lower state rotational quantum number, $(\Delta v_D)_-$ is the wavenumber interval between v_0 and the extrema of the first derivative curve on the low wavenumber side of v_0 , and $(\Delta v_D)_+$ is the corresponding interval on the high wavenumber side. The last column gives the differences (δ) between $(\Delta v_D)_-$ and $(\Delta v_D)_+$. The agreement between these two quantities is quite good; the average value of δ , without regard to sign, is $2.3 \times 10^{-3} \text{ cm}^{-1}$ and in our opinion is a good indication of the accuracy in measurement attainable with our instrument (at least for isolated lines with reasonably good S/N). The differences, δ , are of random sign, thus indicating that any error in locating $x = 0$ in the interferogram is negligible (see Section V).

At this point it is worthwhile examining interferograms from another point of view (Ref. 28). In a recent series of articles Gordon (Ref. 29) has developed the theory concerning the information obtained when the band shapes of IR and Raman bands are Fourier-transformed. Of particular interest is his treatment for pure rotational absorption. His development

Table 1. First Derivative Extremes (Referenced to v_0) for the Pure Rotational Lines of Carbon Monoxide^a

J_L	$(\Delta v_D)_-$, cm ⁻¹	$(\Delta v_D)_+$, cm ⁻¹	$\delta = (\Delta v_D)_- - (\Delta v_D)_+$, cm ⁻¹
6	0.0477	0.0441	+0.0036
7	0.0498	0.0562	-0.0064
8	0.0570	0.0539	+0.0031
9	0.0649	0.0618	+0.0031
10	0.0590	0.0593	-0.0003
11	0.0649	0.0669	-0.0020
12	0.0593	0.0567	+0.0026
13	0.0611	0.0625	-0.0015
14	0.0615	0.0589	+0.0026
15	0.0599	0.0603	-0.0004
16	0.0531	0.0550	-0.0019
17	0.0502	0.0526	-0.0024
18	0.0539	0.0525	+0.0014
19	0.0496	0.0471	+0.0025
20	0.0516	0.0527	-0.0011

^a From an interferogram with absorbing path = 15 cm, p = 608 Torr.

shows that if a pure rotational absorption band, suitably normalized to unit area, is Fourier-transformed (frequency to time) then the dipole moment correlation function $\langle \underline{u}(0) \cdot \underline{u}(t) \rangle$ is obtained. Gordon interprets this correlation function (in the classical limit) as follows:

"Imagine that one could observe the microscopic re-orientation of a single molecule in a system of many molecules in thermal equilibrium. Suppose that at a time "0" the dipole of this molecule points along a direction $\underline{u}(0)$. Then we follow the thermal motions of the molecule and at a time later we measure the projection of $\underline{u}(t)$ on the original direction : $\underline{u}(0) \cdot \underline{u}(t)$. Now we make this measurement again and again, picking out different reference times "0". Finally, we average all of these trajectories $\underline{u}(0) \cdot \underline{u}(t)$ to obtain the correlation function $\langle \underline{u}(0) \cdot \underline{u}(t) \rangle$."

An interferogram is the FCT of the spectrum and is the intensity passed by the interferometer measured as a function of the optical path difference generated by the interferometer. The optical path difference is linearly related to the time of retardation by the velocity of light; thus, interferograms may be easily converted from the optical path difference scale to the time retardation scale by dividing by the velocity of light. Early interferograms (Refs. 23, 24) are complicated by the fact that features of the interferogram corresponding to the absorption of the sample are superimposed on the source interferogram. By using a "double-beam" (reference and sample beam) two-beam interferometer, we can to a large extent subtract the source interferogram, and suitably normalize the resulting interferogram so that it corresponds to the dipole moment correlation function described by Gordon (the correspondence is not exact, see Ref. 30). A portion of such an interferogram is shown in Fig. 22 for gaseous CO ($p = 678$ Torr, and absorption path length = 15 cm).

The interpretation of the interferogram on the basis of wavelength and optical path difference has been given previously (Ref. 23, 31) and the interpretation on the basis of frequency and time is easily seen from

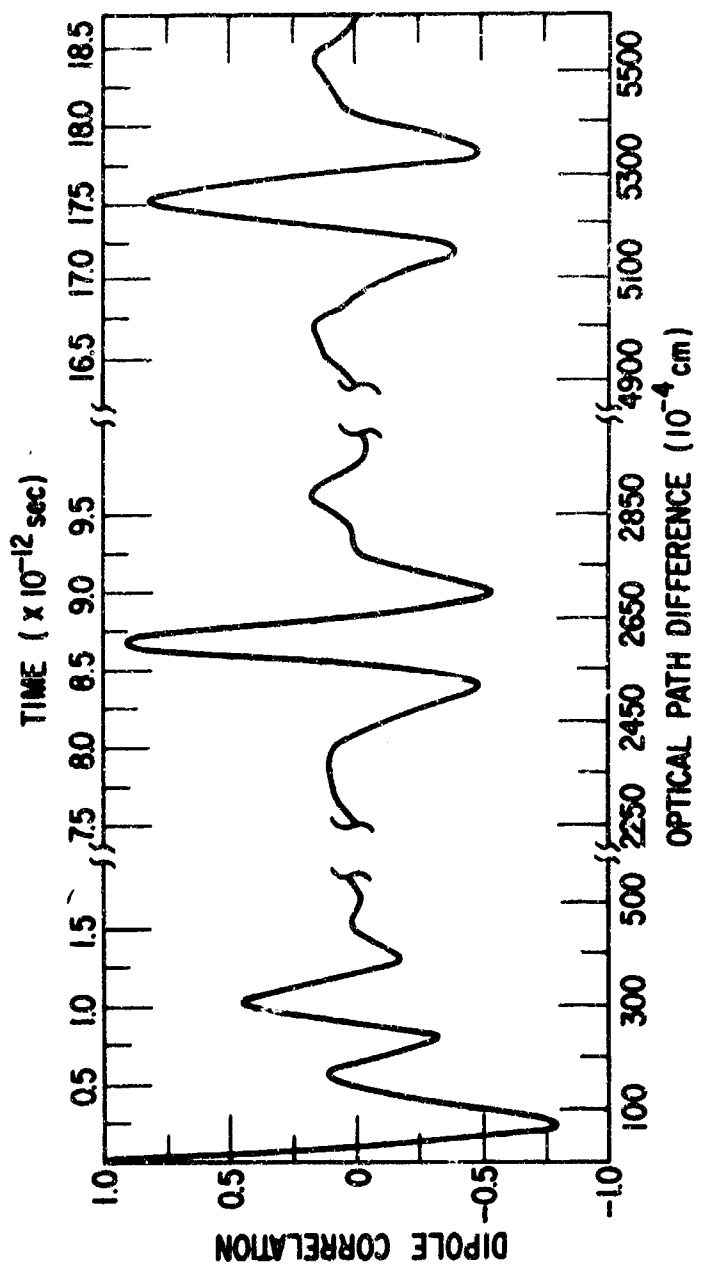


Fig. 22. A portion of the pure rotational, double-beam interferogram of CO. The optical path difference is related to the retardation time by the velocity of light.

Gordon's development. In the semiclassical limit at a time $t = 0$, a molecule in the J th angular momentum state ($= \hbar [J(J+1)]^{1/2} / I = \hbar J / I$, where I is the moment of inertia of the molecule) is perfectly correlated (with the system and itself) since $t = 0$ is chosen as the reference point. After the time of one revolution has passed the correlation will now be less (or even negative), since molecules in other different angular momentum states ($0, 1, 2, \dots, J-1, J+1, J+2, \dots$) will have made more or less revolutions. After times longer than the time of average rotation, the correlation function will oscillate (with decreasing amplitude) about the zero value. However, in the case of diatomic and linear molecules we can expect the correlation function to become significantly positive again for times longer than the average rotational period. This will happen when the molecule in the J th state has made J rotations, then the molecules in any other J' state will have made J' rotations, and if the system has not been disturbed the state of the system at this time will duplicate (neglecting translation) the state of the system at $t = 0$. Also, on the basis of this interpretation, smaller but quite significant negative correlations are expected just before and after the large (~ 1) positive correlation. This behavior is shown quite clearly in Fig. 22. For CO a large positive-correlation occurs at $t \sim 8.7 \times 10^{-12}$ sec, the dipole correlation function attaining the value ~ 0.90 at this time. Extending the argument to longer times shows that the correlation function should show the same behavior at integer multiples of this time. Indeed, the interferogram from which Fig. 22 was taken showed 24 such features (out to $t \sim 2 \times 10^{-10}$ sec). Two general observations may be made about these features (called signatures in interferometry).

First, the correlation peak for any given signature is always less than the one preceding it. This is understandable, using a semiclassical approach. Comparing the state of the system at $t = 0$ with some later time t' , we see that some of the molecules will have had their rotational motion interrupted (by inelastic collisions, or even elastic collisions, that disturb

the phase of the rotation), and thus these molecules will be uncorrelated (on the average). At moderately low pressures and above, this collisional type interruption is the main contribution to the breadth of the spectral line. In fact, it is possible to analyze the fall-off of intensity (or correlation factor) of these signatures for line-width parameters.

Second, the signatures are not symmetric about the maximum positive correlation. The negative correlation just before the large positive correlation is less negative than the one just after. This is because no molecule is perfectly rigid but rather distorts when rotating (centrifugal distortion); therefore, even in the semiclassical limit the angular velocities of the various states are not integer multiples of the lowest rotating state but rather converge slightly, since the moment of inertia increases slightly for each higher state of angular momentum.

Quantum mechanically the above arguments would have to be modified since it is not the rotational frequencies that are observed, but rather the differences in rotational frequencies (usually $\Delta J = \pm 1$). It is expected that the more rigorous argument will lead to much the same interpretation.

2. DEUTERIUM CHLORIDE

A portion of the pure rotational interferogram of deuterium chloride (DCl) is shown in Fig. 23. The expected signatures characteristic of diatomic and linear molecules are seen out to $x \approx 2.5$ cm. Between 2.5 and 3.0 cm there are still variations in the interferogram, but no signatures are apparent. After about 3.2 cm the signatures reappear, although they are broader and down considerably in intensity. This is interpreted as due to the isotopic splitting of the pure rotational spectrum of DCl, due to the two chlorine isotopes Cl³⁵ and Cl³⁷. DCl is essentially a mixture of two molecular species DCl³⁵ and DCl³⁷. The rotational constants for the two molecules are slightly different; thus, the interferogram consists of two sets of signatures that, at small x (low resolution) are in step (superpose constructively), at larger x are out of step (superpose destructively), and at

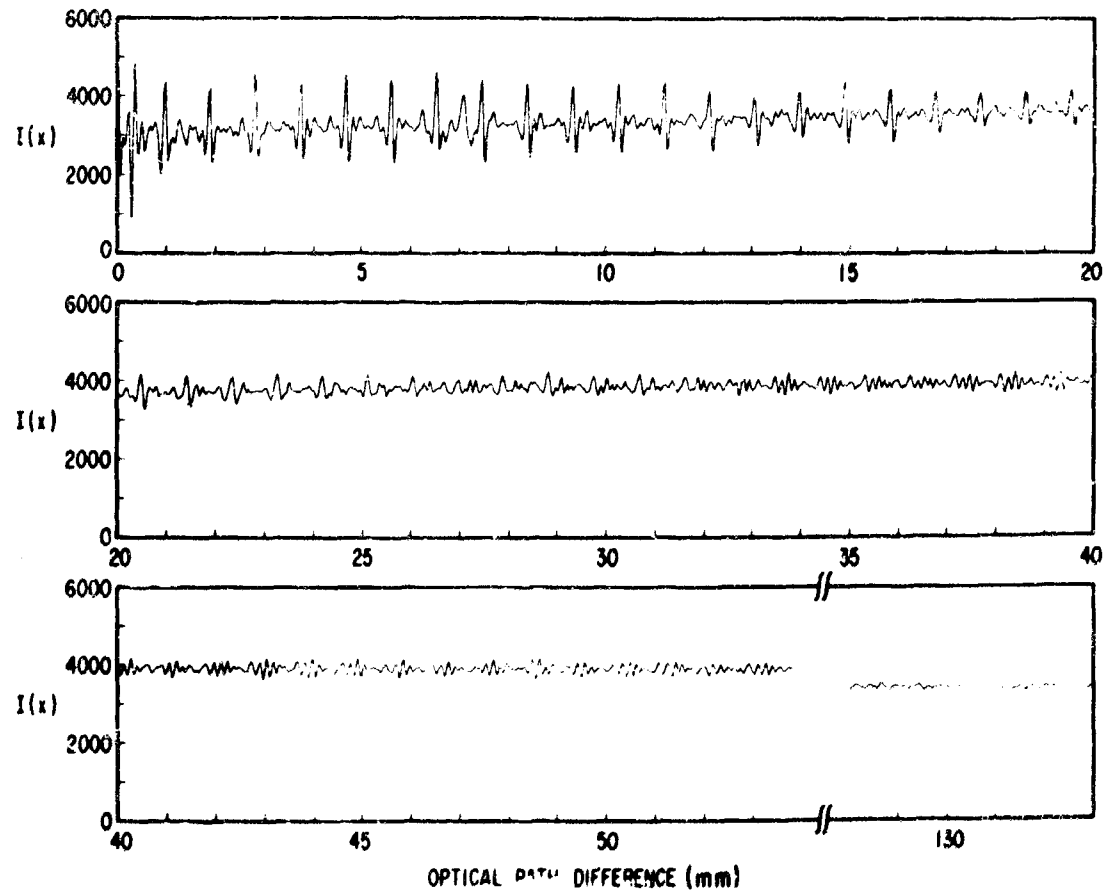


Fig. 23. The pure rotational, double-beam interferogram of DCI.

still larger x get back in step. one lobe removed. The fact that this phenomenon is observed in the interferogram indicates that at least some of the isotopic lines in the DCl^{35} and DCl^{37} pure rotational spectrum are resolved.

Two other comments are in order. The last part of the interferogram ($x \approx 13.5$ cm) is shown, and the estimated signal (true variation about average value of $I(x)$) to noise is about one. Also, there is a drift downward (in intensity) of the interferogram. This is instrumental in nature and is unimportant, since a long term drift (in x) corresponds to extremely low wavenumber (frequency) components in the spectrum (0 to $\sim 2 \text{ cm}^{-1}$).

In Fig. 24 are shown selected regions of the pure rotational spectrum of DCl . The $J = 1 \rightarrow 2$ (21.5 cm^{-1}), $J = 2 \rightarrow 3$ (32.3 cm^{-1}), and $J = 3 \rightarrow 4$ (43.0 cm^{-1}) regions are shown. The $J = 2 \rightarrow 3$ transition is clearly split, and it is evident that the resolution displayed is better than the separation of the lines, which is 0.094 cm . The $J = 1 \rightarrow 2$ is not split but is definitely asymmetric. The calculated splitting is 0.063 cm^{-1} (Refs. 32, 33). The theoretical resolution of this run was 0.074 cm^{-1} . It is clear from the more than adequately split $J = 2 \rightarrow 3$ transition and the unresolved but definitely asymmetric $J = 1 \rightarrow 2$ transition that the theoretical resolution is closely approached.

3. NITRIC OXIDE

Nitric oxide (NO) has been of great scientific interest because of its unique property of being a stable diatomic molecule having an odd number of electrons. (The pure rotational spectrum of NO is reported in Ref 34.) The ground state of NO is a $^2\pi$ state which is split into $^2\pi_{1/2}$ and $^2\pi_{3/2}$ components by spin-orbit interaction. The splitting is small ($\approx 122 \text{ cm}^{-1}$), resulting in appreciable population of both components at room temperature. The consequence of this splitting in the pure rotational spectrum of NO is the appearance of two series of lines that can be assigned to the two components of the $^2\pi$ state. Rotational constants can be derived for both series, but because of the perturbation by the low-lying electronic state the constants

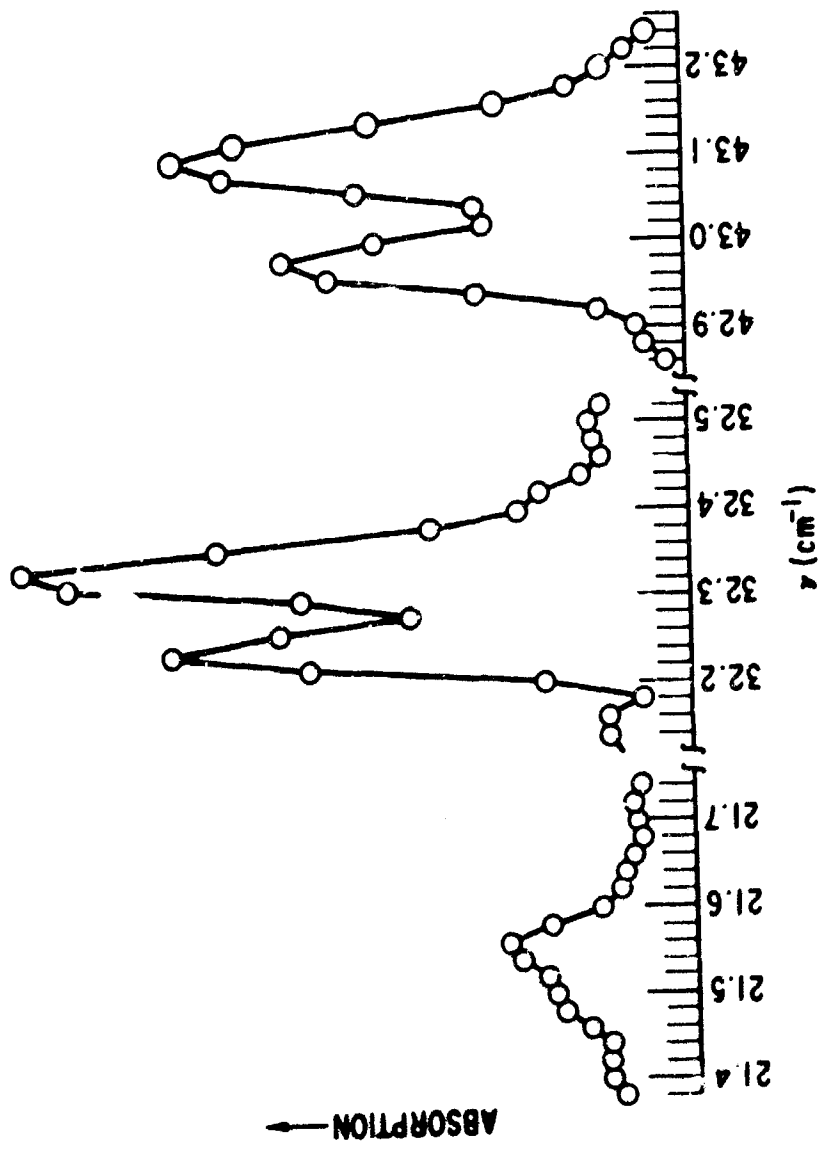


Fig. 24. Selected regions of the pure rotational spectrum of DCl. The calculated splitting of the $J = 1 \rightarrow 2$ (21.5 cm^{-1}) doublet is 0.063 cm^{-1} ; for the $J = 2 \rightarrow 3$ (32.2 cm^{-1}) doublet is 0.094 cm^{-1} ; and for the $J = 3 \rightarrow 4$ (43.0 cm^{-1}) is 0.126 cm^{-1} .

so derived are only effective constants which are combinations of the usual rotational constants and additional terms due to the spin-orbit perturbation.

The microwave spectrum of NO was reported by Gallagher and Johnson (Ref. 35), who determined the effective molecular constants for the $^2\Pi_{1/2}$ state and calculated the constants for the $^2\Pi_{3/2}$ state. Favero, Mirri, and Gordy (Ref. 36) more recently have reported the millimeter wave spectrum of the $^2\Pi_{3/2}$ state and derived constants for it. Recently there has been a great deal of work in the near- and intermediate-IR spectral regions. Arcas, et al. (Ref. 37) studied the 3-0 band of NO with a precision of $\sim 0.03 \text{ cm}^{-1}$. Olman, et al. (Ref. 38) studied this band and also the 2-0 band with a precision of about 0.01 cm^{-1} . Meyer, et al. (Ref. 39) studied the 2-0, 3-0, and 4-0 bands with a precision of better than 0.01 cm^{-1} . James and Thibault (Ref. 40) studied the fundamental region with a precision comparable to that of Olman, et al. Palik and Rao (Ref. 41) reported results obtained in the FIR spectral region with a precision of about 0.05 cm^{-1} .

There is significant disagreement in values of the effective constants as determined by the numerous experimenters, and, in particular, the effective rotational constants determined in previous IR investigations (Refs. 37-41) differ significantly from those determined in microwave investigations (Refs. 35, 36).

Therefore, in order to resolve the discrepancies between microwave and IR results, it was decided to re-investigate the pure rotational spectrum of NO at high resolution. The line positions were determined once with high resolution ($\approx 0.06 \text{ cm}^{-1}$) and were corroborated by a lower resolution ($\approx 0.1 \text{ cm}^{-1}$) run. The precision of the line positions is estimated to be about 0.003 cm^{-1} except at the high and low extremes of the spectrum where the S/N was poorer.

The parameters for the high resolution run are as follows: The interferogram was digitally sampled at $40-\mu$ optical path difference increments. Each point was sampled for 7 seconds to improve the S/N. The

maximum optical path difference generated was 160 mm. A total of 4000 points were recorded in the interferogram. The transformed spectrum was computed at 0.02 cm^{-1} interval.

Air Products and Chemicals NO of 99.0% purity was used. The gas was additionally purified by passing through a dry ice-acetone trap. The sample was slightly contaminated by NO_2 as was evidenced by its pale yellow color when viewed through the cell. Some of the weak unidentified features in the spectrum may be due to NO_2 absorption. The sample was contained in a 15-cm path length cell with crystalline quartz windows at a pressure of 399 Torr at room temperature (298°K).

Figure 25 shows selected regions of the interferogram. Many qualitative features of the pure rotational spectrum of NO can be deduced directly from the interferogram. First, it can be seen that there are actually two sets of signatures (denoted by the "a" and "b" sequence) that are well separated beyond about 30-mm optical path difference. It follows from this that the spectrum will consist of two sets of almost uniformly spaced lines, the spacing for the "a" sequence being larger than that for the "b" sequence. Second, the "a" sequence is distorting (smearing out) more rapidly than the "b". It follows then that lines corresponding to the "a" set will show a greater convergence (because of centrifugal distortion and higher order terms) than those of the "b" set. Finally, adjacent signatures in each set are nearly inverted copies of each other, which indicates that the quantum number J in the energy level expression is nonintegral. In fact, since adjacent signatures are completely inverted with respect to each other, J is half-integral.

Figure 26 shows the spectrum computed from the interferogram shown in Fig. 25. The relative intensities of the lines are influenced by the envelope of the source output spectrum and are not true indications of the band contour. The source output spectrum has been discussed previously. This run was not calibrated for intensity, but the shape of the source spectrum is very similar to that shown in Fig. 20.

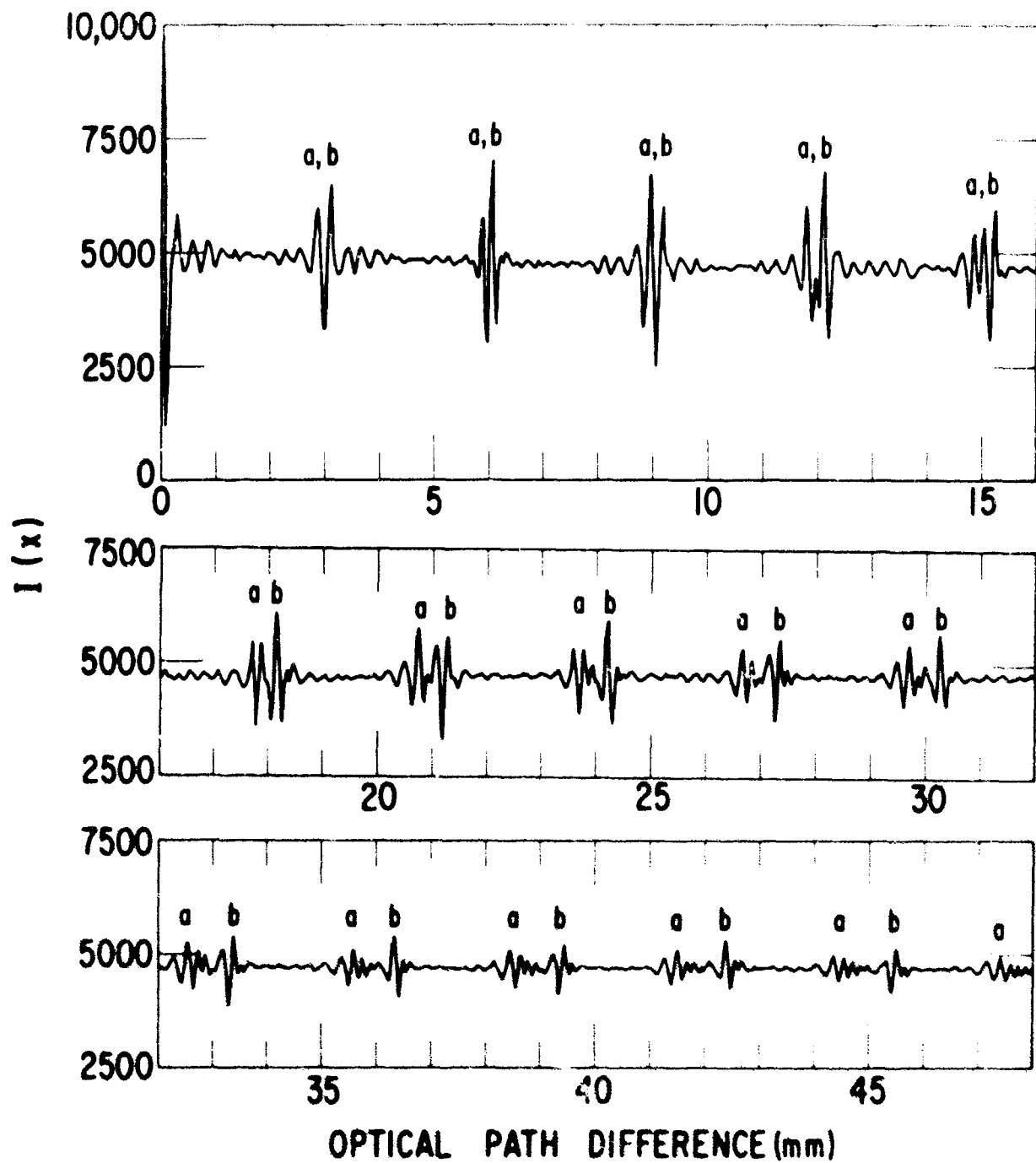


Fig. 25. The pure rotational, double-beam interferogram of NO up to $x = 4.8$ cm.

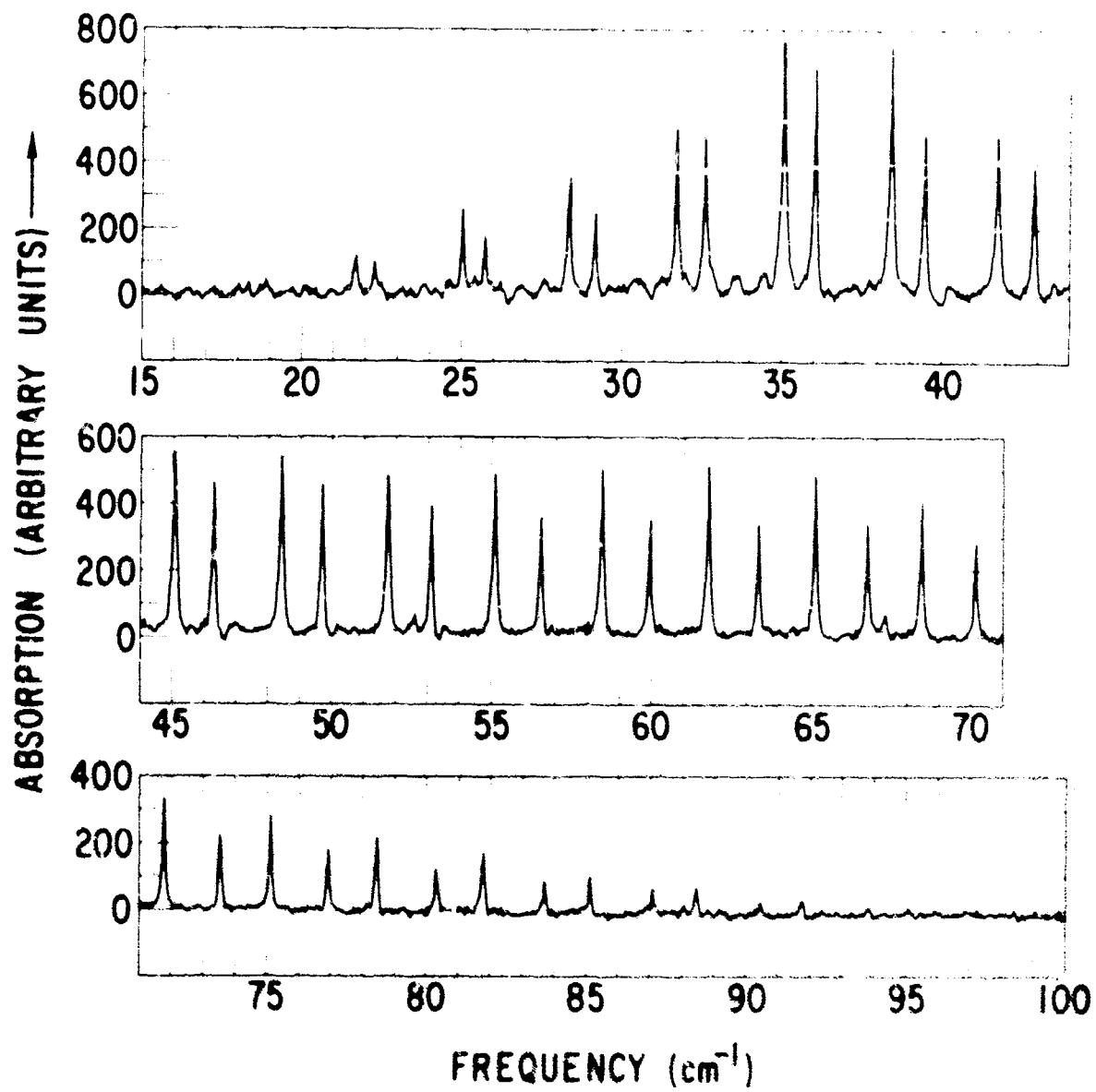


Fig. 26. The pure rotational spectrum of NO.

Table 2 lists the frequencies of the lines observed and their assignments, together with deviations from frequencies calculated using constants derived from analyses of these data. Frequencies of peak absorption were computed by the method of zero slope from the 0.02 cm^{-1} interval computer output. As mentioned above, the accuracy of the observed frequencies is $\pm 0.003 \text{ cm}^{-1}$. The frequencies are quoted to 0.0001 cm^{-1} . Little confidence is placed in the last figure, but it is included to offset roundoff errors in the comparison with calculated values. Transitions not used in the least squares analyses are enclosed in parentheses.

Table 2. Observed Frequencies and Deviations of Calculated Frequencies of Nitric Oxide

J + 1/2	$^2\pi_{1/2}$			$^2\pi_{3/2}$		
	Observed, cm^{-1}	(obs-calc) ^a $\times 10^4, \text{cm}^{-1}$	(obs-calc) ^b $\times 10^4, \text{cm}^{-1}$	Observed, cm^{-1}	(obs-calc) ^a $\times 10^4, \text{cm}^{-1}$	(obs-calc) ^b $\times 10^4, \text{cm}^{-1}$
5	(18.392) ₆	+25	+24	(18.907) ₉	-73	-78
6	21.731 ₇	-19	-20	22.350 ₀	+12	-18
7	25.075 ₄	-16	-17	25.784 ₆	-9	-16
8	28.422 ₅	+21	+21	29.220 ₃	+22	+15
9	31.764 ₀	+8	+7	32.648 ₇	0	-6
10	35.107 ₁	+8	+8	36.078 ₇	+16	+11
11	38.450 ₃	+14	+14	39.502 ₇	-3	-7
12	41.793 ₂	+21	+21	42.926 ₅	+2	0
13	45.132 ₂	-7	-7	46.346 ₃	-4	-5
14	48.475 ₃	+11	+11	49.763 ₉	-2	-2
15	51.814 ₁	-7	-7	53.178 ₈	+5	+7
16	55.155 ₂	+6	+6	56.588 ₂	-9	+6
17	58.492 ₃	-12	-12	59.996 ₀	-6	-1
18	61.829 ₈	-17	-16	63.399 ₁	-10	-4
19	65.167 ₆	-5	-5	66.800 ₈	+8	+15
20	68.501 ₉	-15	-14	70.198 ₅	+25	+31
21	71.837 ₃	+3	+4	73.586 ₉	-11	-5
22	75.166 ₉	-17	-17	76.973 ₃	-25	-21
23	78.499 ₀	+7	+7	80.357 ₀	-25	-25
24	81.828 ₁	+27	+26	83.740 ₄	+14	+9
25	85.150 ₀	+1	0	87.114 ₄	+2	-10
26	(88.478) ₄	+71	+69	(90.482) ₆	-26	-47
27	(91.784) ₅	-48	-51	(93.856) ₅	+47	+12

^aLeast squares analysis determining B_o , D_o , and H_o

^bLeast squares analysis holding B_o at microwave value ($^2\pi_{1/2}$, Ref. 35;
 $^2\pi_{3/2}$, Ref. 36) and determining D_o and H_o .

The data were analyzed by computing a least squares fit to the following power series in $(J + 1)$:

$$\nu = 2B_o(J + 1) - (4D_o - 2H_o)(J + 1)^3 + 6H_o(J + 1)^5 \quad (12)$$

where ν is the frequency of the transition, J the quantum number of the lower state, B_o the effective rotational constant, D_o the effective centrifugal distortion constant, and H_o the effective higher order distortion constant, which is not negligible for NO. Least squares analyses were made on each series and on the difference frequencies between the two states. It is felt that the difference frequencies are more accurate than the frequencies themselves, since the differences tend to minimize any errors in the wavenumber scale such as might be generated by a phase error in the interferogram.

The first line in Table 3 shows the result of these analyses. The errors given are 95% confidence intervals. The differences between the observed frequencies and those calculated using the constants determined by

Table 3. Effective Rotational Constants of Nitric Oxide (in cm^{-1})

Reference	$B_o^{\text{eff}}(\pi_{1/2})$	$B_o^{\text{eff}}(\pi_{3/2})$	$\Delta B_c^{\text{eff}}(\pi_{3/2} - \pi_{1/2})$	$D_o^{\text{eff}}(\pi_{1/2})$
-- This work	1.6718614 ± 0.000081	1.720178 ± 0.000062	0.048323 ± 0.000057	$(3.4 \pm 3.0) \times 10^{-7}$
-- This work ^a	[1.6718614]	[1.7196531]	[0.04779172]	$(3.6 \pm 1.4) \times 10^{-7}$
-- This work ^b	[1.6718614]	[1.7202435]	[0.04838213]	$(3.6 \pm 1.4) \times 10^{-7}$
35 Microwave	1.6718614	1.7196531		1.13×10^{-6}
36 Microwave		1.7202435		
40 Near-IR	1.67229 ± 0.00025	1.72014 ± 0.00025		$(7.728 \pm 3.5) \times 10^{-7}$
37 Near IR	1.67199	1.71958		1.77×10^{-6}
38 Near-IR	1.67233 ± 0.00019	1.72012 ± 0.00018		$(1.6 \pm 0.3) \times 10^{-6}$
39 Near-IR	1.67223	1.72002		1.5×10^{-6}
41 FIR	1.6720	1.7198		1.8×10^{-6}

these analyses are shown in the third and sixth columns of Table 2. The average deviations from frequencies used in the analyses for either state are about $\pm 0.0012 \text{ cm}^{-1}$. Since the analyses reproduced the microwave rotational constants so well, it was decided to use the microwave values of the effective B_o 's and perform least squares analyses for the effective D_o 's and H_o 's. The results of these analyses are shown as the second and third lines in Table 3. The second line is the result of using Gallagher and Johnson's (Ref. 35) values for both $B_o(^2\pi_{1/2})$ and $B_o(^2\pi_{3/2})$. The assumed values are given in brackets. The constants of the $\pi_{3/2}$ state derived by the analysis reproduced the observed frequencies with significantly greater deviations of a nonrandom character than the constants given in the first line, indicating that the value of $B_o(^2\pi_{3/2})$ calculated by Gallagher and Johnson is in error. The third line is the result of using Gallagher and Johnson's (Ref. 35) value of $B_o(^2\pi_{1/2})$ and Favero, Mirri, and Gordy's (Ref. 36) value of $B_o(^2\pi_{3/2})$. The constants derived from these analyses

Table 3, Continued

$D_o^{\text{eff}}(^2\pi_{3/2})$	$\Delta D_o^{\text{eff}}(^2\pi_{3/2} - ^2\pi_{1/2})$	$H_o^{\text{eff}}(^2\pi_{1/2})$	$F_o^{\text{eff}}(^2\pi_{3/2})$	$\Delta H_o^{\text{eff}}(^2\pi_{3/2} - ^2\pi_{1/2})$
$(10.24 \pm 0.23) \times 10^{-6}$	$(9.90 \pm 0.21) \times 10^{-6}$	$(-1.42 \pm 0.29) \times 10^{-9}$	$(+1.00 \pm 0.23) \times 10^{-9}$	$(+2.42 \pm 0.21) \times 10^{-9}$
$(8.51 \pm 0.40) \times 10^{-6}$	$(8.14 \pm 0.40) \times 10^{-6}$	$(-1.40 \pm 0.18) \times 10^{-9}$	$(-0.51 \pm 0.53) \times 10^{-9}$	$(+0.89 \pm 0.54) \times 10^{-9}$
$(10.46 \pm 0.12) \times 10^{-6}$	$(10.10 \pm 0.10) \times 10^{-6}$	$(-1.40 \pm 0.18) \times 10^{-9}$	$(+1.19 \pm 0.15) \times 10^{-9}$	$(+2.59 \pm 0.14) \times 10^{-9}$
10.64×10^{-6}				
$(10.70 \pm 0.19) \times 10^{-6}$		-2.091×10^{-9} (calc)	$+2.093 \times 10^{-9}$ (calc)	
9.77×10^{-6}				
$(9.5 \pm 0.3) \times 10^{-6}$				
9.3×10^{-6}				
10.0×10^{-6}				

^a Constants derived by assuming the microwave values of B_o from Ref. 35 and performing least squares calculations to determine D_o and H_o .

^b Constants derived by assuming the microwave value of $B_o^{\text{eff}}(^2\pi_{1/2})$ from Ref. 35 and $B_o^{\text{eff}}(^2\pi_{3/2})$ from Ref. 36 and performing least square calculations to determine D_o and H_o .

have significantly smaller confidence intervals and reproduce the observed frequencies as well as the complete analysis. The differences between the observed frequencies and those calculated using the constants given in the third line are given in the fourth and seventh columns of Table 2. The average deviations for either state are about 0.0012 cm^{-1} , the same as for the complete analysis.

The values of the difference constants are also included in Table 3. It should be noted that the confidence limits are smaller than for either state separately. This corroborates the belief that the difference frequencies are known better than the frequencies themselves. Finally, Table 3 includes a tabulation of constants derived by other experimenters given the spectral region in which data were obtained.

Once the values of the effective constants have been determined, the unperturbed ground state rotational constants can be obtained from them. Using the formulation developed by James and Thibault (Ref. 40) the true constants are given by

$$B_o = 1/2 (B_{o1} + B_{o2} - 3D_o)$$

$$D_o = 1/2 (D_{o1} + D_{o2})$$

$$H_o = 1/2 (H_{o1} + H_{o2})$$

Table 4. Rotational Constants of Nitric Oxide

$$B_o = 1.696008 \pm 0.000072 \text{ cm}^{-1}$$

$$D_o = (5.29 \pm 0.27) \times 10^{-6} \text{ cm}^{-1}$$

$$H_o = (-2.1 \pm 2.6) \times 10^{-10} \text{ cm}^{-1}$$

where the subscripts 1 and 2 denote the $^2\Pi_{1/2}$ and $^2\Pi_{3/2}$ states, respectively. The constants obtained from these relations are given in Table 4. The errors quoted are approximately 95% confidence limits.

One constant of NO which is of great interest is the spin-orbit coupling constant, A_o . The conventional relation (Ref. 40) used for calculating A_o is

$$B_{o2} - B_{o1} = \frac{2B_o^2}{[A_o(A_o - 4B_o)]^{1/2}}$$

Using the values of these constants given in Tables 2 and 3, one obtains a value of A_o of 122.49 cm^{-1} . But, as James and Thibault (Ref. 40) have pointed out, this formulation is incorrect. They derived a rather extensive series of equations from which the correct value of A_o can be obtained. Unfortunately these equations depend strongly on the values of D_{o1} , D_{o2} , and D_o , constants which have not been well determined. Using these equations for A_o , a value of 128.6 cm^{-1} is obtained. Little confidence can be placed in this value, however, for reasons stated above. Information obtained in the vibrational spectrum of NO, namely the difference in band origins of the satellite band and the ${}^2\pi_{3/2} - {}^2\pi_{3/2}$ band, gives a direct measure of δ_o . The value of A_o is very sensitive to this parameter. A_o is related to δ_o by the following equation (Ref. 39):

$$A_o = \left[\delta_o^2 + 3(B_o + \frac{3}{2}D_o)^2 \right]^{1/2} + 2B_o$$

Using James and Thibault's (Ref. 40) value of δ_o , 119.732 cm^{-1} , and the values of B_o and D_o from Table 3, one obtains a value of A_o of 123.1600 cm^{-1} . The accuracy of this value is limited by the precision with which δ_o is known. The inaccuracies of the other constants are in the fifth and greater decimal places.

Included in Table 3 are values of the effective rotational constants obtained in the other investigations. It should be noted that our value of

$B_o(^2\pi_{1/2})$ reproduces the microwave value of Gallagher and Johnson (Ref. 35) well within our experimental uncertainty. Our uncertainty does not bracket any of the other IR values of this constant. It should be pointed out that in two of the near-IR investigations (Refs. 38, 40) the data were not analyzed using the well-known combination difference relations⁷, but rather were directly analyzed in terms of a power series in J whose coefficients are combinations of upper and lower state constants. This type of analysis suffers the usual drawbacks of data fitted to a high order polynomial, many coefficients of which are small. The other near-IR investigations (Refs. 37, 39) did use combination relations.

Our value of $B_o(^2\pi_{3/2})$ is bracketed by the two microwave values and does not overlap either within our uncertainty. No uncertainty was quoted with either microwave value. We are very close to the value of Favero, et al. (Ref. 35). However, when the microwave values of the effective B_o 's were used in the least squares analyses of our data, only the effective B_o of Favero, et al. (Ref. 35) gave good agreement with observed frequencies and, importantly, the agreement using their value of $B_o(^2\pi_{3/2})$ was no different than that using our value.

The values of the centrifugal distortion constants are much less accurately determined. In general, the value of $D_o(^2\pi_{3/2})$ agrees with other values, $\approx 10 \times 10^{-6} \text{ cm}^{-1}$. The uncertainty of this value is of the same order as that given for other values. However, the value of $D_o(^2\pi_{1/2})$ is considerably lower than any other. This value is the least well determined of all the effective constants. One overriding factor with respect to both D_o and H_o is that our data are the only data accurate enough to allow significant

⁷ Because many of the lines in the vibration-rotation bands were not resolved or were blended with overlapping water vapor lines, the authors of Refs. 38 and 40 felt there were insufficient combination relations involving unblended lines to permit an accurate analysis.

determinations of the effective higher order distortion constants, H_o . Our values of the effective H_o 's agree in sign with the calculated values of James and Thibault (Ref. 40). Their data were not accurate enough to permit a significant experimental determination of these constants.

4. WATER VAPOR

H. M. Randall's 1938 review article (Ref. 42) on FIR spectroscopy aptly described the FIR absorption spectrum of water vapor as "a complex and apparently chaotic arrangement of lines." Since the first observation by Wright and Randall (Ref. 43) in 1933 of a water vapor spectrum in which rotational structure beyond 100μ was resolved, the pure rotational spectrum of water vapor has served as a test of instrumental performance and a background with which nonvacuum spectrometers have had to contend.

Early workers (Refs. 43-45) in the FIR spectral region were able to achieve a resolution of up to 0.5 cm^{-1} in their observations of the spectrum of water vapor. However, using those results the energy levels, and hence rotational constants, could not be determined as accurately as possible from the near-IR vibration-rotation spectrum. Therefore, observations of the pure rotational spectrum of water vapor were used only for illustrations of instrumental performance and secondary frequency calibrations for the FIR. No further analysis of the spectra was attempted. Genzel and Eckhardt (Ref. 46) first reported the very far (beyond 200μ) IR spectrum of water vapor in 1954. Since then there have been many papers (Refs. 47-55) on the FIR spectrum of water vapor; however, none with resolution comparable to that obtainable in the near-IR vibration-rotation spectrum. Four separate measurements of the spectrum were made using a cell with 15-cm absorbing path length and with pressures of 7.5, 10.0 (2 runs), and 16.5 Torr at room temperature (298°K). The modular resolution of the four runs was between 0.06 and 0.09 cm^{-1} .

The parameters for the runs are as follows. The interferograms were digitally sampled at $40-\mu$ optical path difference increments. Each

point was sampled for 5 to 7 seconds (constant for a given run) to improve the S/N. The maximum optical path difference generated was between 114 and 160 mm. Between 2850 and 4001 points were recorded in each interferogram. The transformed spectrum was computed at approximately 0.02 cm^{-1} intervals.

Figure 27 shows the spectrum from 5 to 125 cm^{-1} computed from one of the interferograms. This spectrum was obtained with 10.0 Torr pressure (298°K) in a 15-cm cell and has a modular resolution of 0.063 cm^{-1} . The relative intensities of the lines are influenced by the envelope of the source output spectrum and are not true indications of actual intensities. These runs were not calibrated for intensity, but the shape of the source spectrum is very similar to that shown in Fig. 20.

Below the spectrum are shown the calculated (Ref. 56) frequencies and relative intensities for pure rotational transitions of water vapor using the energy level scheme of Gates, et al. (Ref. 57). These relative intensities have not been normalized to the source spectrum.

Figure 28 shows details of two portions of the spectrum illustrating the resolution attained. Figure 28a shows the triplet at 38 cm^{-1} . The calculated separation of the $5_{41} - 6_{34}$ (38.642_1 cm^{-1}) and $3_{12} - 3_{21}$ (38.791_6 cm^{-1}) transitions is 0.149 cm^{-1} . Figure 28b shows the doublet at 59 cm^{-1} . The calculated separation of two components is 0.0678 cm^{-1} . These results are the first published to resolve this doublet.

Table 5 lists the frequencies of the lines (in cm^{-1}) observed and their assignment, together with calculated frequencies, calculated relative intensities (Ref. 56), and observed relative strength. The calculated frequencies were computed from energy levels determined in this study. The calculated relative intensities are normalized to 100 for the $3_{03} - 3_{12}$ transitions at 36.6055 cm^{-1} , the line of greatest apparent intensity in our spectra. The relative strengths are rough guides of apparent intensity, and therefore precision, of the lines as observed in our spectra. Whenever possible,

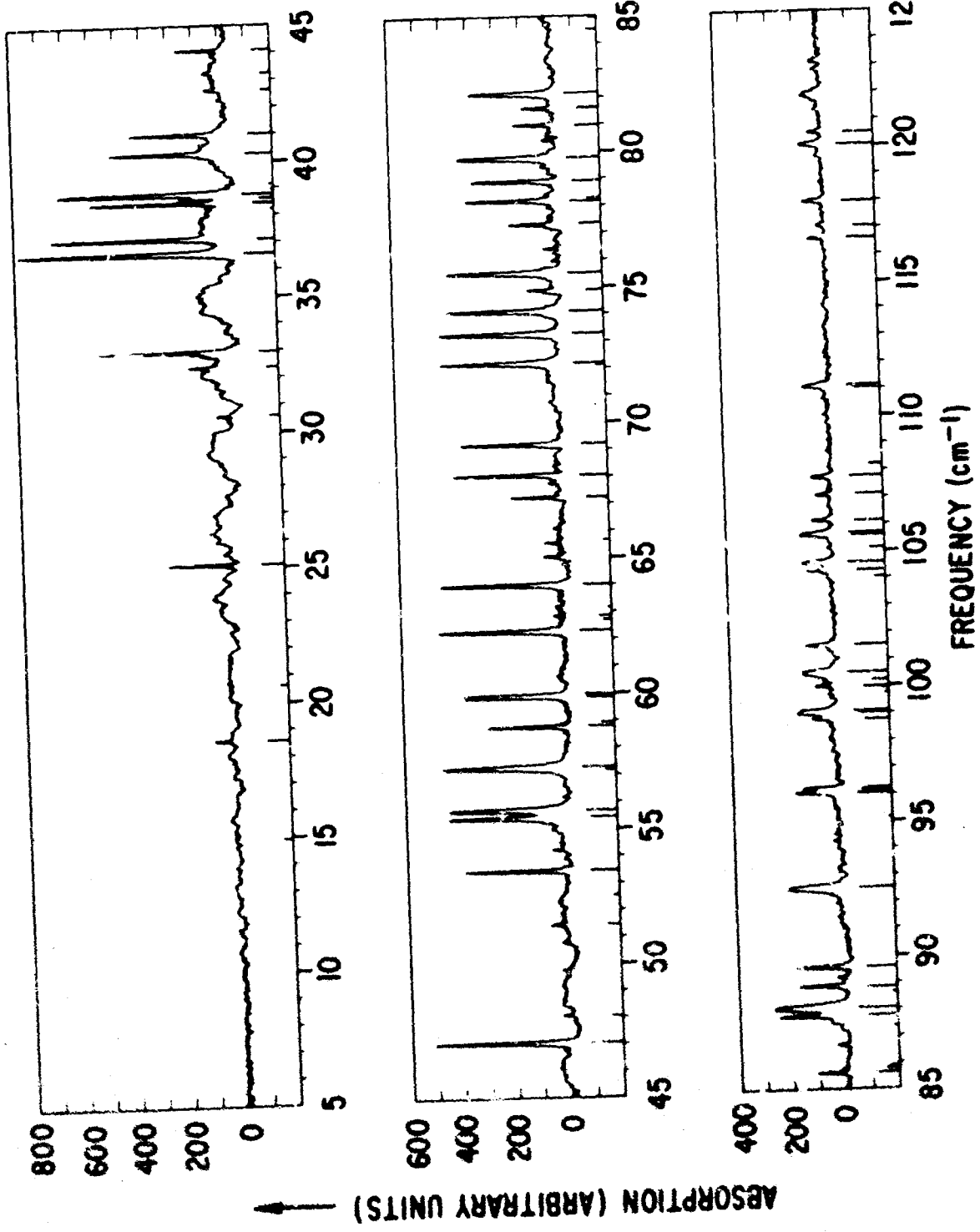


Fig. 27. The pure rotational spectrum of water vapor.

Table 5. Pure Rotational Transitions of Water Vapor

Observed Frequency, cm ⁻¹	Calculated Frequency, cm ⁻¹	Relative Strength	Calculated Relative Intensity	Assignment
18.570 ₆ (47)*	(18.570 ₆)**	M	13.7	$^1_{01} \rightarrow ^1_{10}$
25.085 ₅ (19)	(25.085 ₅)	S	15.1	$^2_{02} \rightarrow ^2_{11}$
30.556 ₈ (45) ²	30.560 ₁	W	0.8	$^3_{31} \rightarrow ^4_{22}$
32.365 ₅ (42)	32.364 ₉	W	1.2	$^4_{31} \rightarrow ^5_{24}$
32.951 ₂ (10)	(32.951 ₂)	S	6.6	$^1_{11} \rightarrow ^2_{02}$
36.605 ₅ (15)	(36.605 ₅)	S	100.0	$^3_{03} \rightarrow ^3_{12}$
37.137 ₁ (7)	(37.137 ₁)	S	4.4	$^0_{00} \rightarrow ^1_{11}$
38.465 ₀ (3)	38.468 ₂	S	10.9	$^2_{21} \rightarrow ^3_{12}$
38.642 ₁ (79)	38.64 ₃	W	2.2	$^5_{41} \rightarrow ^6_{34}$
38.791 ₆ (18)	(38.791 ₆)	S	108.6	$^3_{12} \rightarrow ^3_{21}$
40.283 ₀ (10)	(40.283 ₀)	S	43.6	$^4_{13} \rightarrow ^4_{22}$
40.987 ₃ (6)	(40.987 ₃)	S	20.9	$^2_{11} \rightarrow ^2_{20}$
42.633 ₀ (34) ²	42.62 ₂	W	0.7	$^6_{52} \rightarrow ^7_{43}$
43.250 ₀ (34) ²	43.24 ₈	W	0.8	$^7_{34} \rightarrow ^8_{27}$
44.098 ₉ (20)	(44.09 ₉)	M	5.2	$^5_{32} \rightarrow ^6_{25}$
47.052 ₉ (29)	(47.05 ₃)	S	135.7	$^5_{14} \rightarrow ^5_{23}$
48.060 ₂ (58)	(48.060 ₂)	W	1.0	$^6_{33} \rightarrow ^7_{26}$
51.437 ₆ (57)	51.433 ₈	W	1.4	$^5_{42} \rightarrow ^6_{33}$
53.444 ₆ (20)	(53.444 ₆)	S	54.3	$^4_{04} \rightarrow ^4_{13}$
55.406 ₃ (16)	(55.406 ₃)	S	79.1	$^2_{12} \rightarrow ^2_{21}$
55.704 ₆ (78)	(55.704 ₆)	S	113.0	$^1_{01} \rightarrow ^2_{12}$
57.269 ₀ (31)	(57.269 ₀)	S	175.7	$^2_{12} \rightarrow ^3_{03}$
58.772 ₂ (32)	(58.772 ₂)	S	34.5	$^6_{24} \rightarrow ^6_{33}$
58.903 ₀ (79) ³	58.89 ₀	W	1.5	$^6_{42} \rightarrow ^7_{35}$

Table 5. (cont)

Observed Frequency, cm ⁻¹	Calculated Frequency, cm ⁻¹	Relative Strength	Calculated Relative Intensity	Assignment
59.871 ₂ (48)	(59.871 ₂)	S	41.8	6 ₁₅ → 6 ₂₄
59.939 ₃ (44)	(59.93 ₉)		63.3	7 ₂₅ → 7 ₃₄
62.300 ₈ (19)	(62.30 ₁)	S	149.2	5 ₂₃ → 5 ₃₂
62.871 ₃ (-) ¹	62.84 ₃	W	1.3	7 ₅₂ → 8 ₄₅
64.010 ₄ (31)	[64.028 ₂] [64.04 ₀]	S	55.3 22.2	3 ₁₃ → 3 ₂₂ 4 ₃₂ → 5 ₂₃
67.240 ₈ (26)	(67.24 ₀)	M	12.0	8 ₂₆ → 8 ₃₅
68.059 ₈ (42)	(68.059 ₈)	S	57.1	4 ₂₂ → 4 ₃₁
69.191 ₈ (24)	(69.191 ₈)	S	30.1	3 ₂₂ → 4 ₁₃
72.186 ₁ (16)	(72.186 ₁)	S	116.5	2 ₀₂ → 3 ₁₃
73.259 ₁ (32)	(73.259 ₁)	S	127.4	3 ₂₁ → 3 ₃₀
74.108 ₀ (30)	(74.10 ₈)	S	206.0	5 ₀₅ → 5 ₁₄
74.875 ₃ (73)	(74.87 ₅)	M	4.1	7 ₄₃ → 8 ₃₆
75.523 ₂ (24)	(75.523 ₂)	S	233.4	4 ₁₄ → 4 ₂₃
77.313 ₈ (38)	[77.32]***	M	12.8	9 ₃₆ → 9 ₄₅
78.193 ₆ (30)	(78.19 ₃)	S	101.6	7 ₁₆ → 7 ₂₅
78.914 ₇ (26)	(78.914 ₇)	S	47.4	3 ₂₂ → 3 ₃₁
79.775 ₄ (19)	(79.775 ₄)	S	180.8	3 ₁₃ → 4 ₀₄
80.997 ₅ (37)	[81.00]	M	18.0	9 ₂₇ → 9 ₃₆
81.617 ₅ (43)	(81.61 ₈)	M	11.0	8 ₃₅ → 8 ₄₄
82.152 ₈ (28)	(82.152 ₆)	S	222.1	4 ₂₃ → 4 ₃₂
85.629 ₅ (37)	(85.62 ₉)	M	11.1	6 ₄₃ → 7 ₃₄
85.783 ₄ (-) ¹	[85.80]	W	1.8	11 ₃₈ → 11 ₄₇
87.759 ₄ (32)	(87.759 ₄)	S	78.1	5 ₂₄ → 5 ₃₃

Table 5. (cont)

Observed Frequency, cm ⁻¹	Calculated Frequency cm ⁻¹	Relative Strength	Calculated Relative Intensity	Assignment
88.077 ₄ (261) [†]	88.079 ₁	S	706.8	3 ₀₃ → 4 ₁₄
88.877 ₁ (51)	(88.87 ₈)	M	70.0	7 ₃₄ → 7 ₄₃
89.581 ₈ (51)	(89.581 ₈)	M	86.2	5 ₁₅ → 5 ₂₄
92.515 ₅ (245) [†]	92.540 ₃	M	262.0	1 ₁₀ → 2 ₂₁
96.067 ₂ (99)	(96.06 ₇)	M	198.7	6 ₂₅ → 6 ₃₄
96.212 ₈ (32)	{ 96.186 ₈ 96.24 ₆ }	M	{ 69.7 40.6 }	6 ₀₆ → 6 ₁₅ 6 ₃₃ → 6 ₄₂
98.800 ₆ (40)	(98.800 ₆)		21.8	5 ₃₃ → 6 ₂₄
99.066 ₈ (179)	{ 99.024 ₀ 99.14 ₀ }	M	{ 83.9 275.8 }	1 ₁₁ → 2 ₂₀ 4 ₂₃ → 5 ₁₄
100.021 ₀ (54)	{ [99.96] [99.98] }	W	{ 1.4 23.7 }	11 ₄₇ → 11 ₅₆ 8 ₁₇ → 8 ₂₆
100.521 ₉ (256)	{ [100.23] 100.55 ₅ }	M	{ 3.1 975.5 }	10 ₂₈ → 10 ₃₇ 4 ₁₄ → 5 ₀₅
101.523 ₄ (84)	(101.52 ₃)	M	160.5	5 ₃₂ → 5 ₄₁
104.288 ₄ (61)	(104.288 ₄)	W	44.4	4 ₃₁ → 4 ₄₀
104.570 ₅ (39)	(104.570 ₅)	M	359.0	4 ₀₄ → 5 ₁₅
105.113 ₃ (-) ¹	(105.12)	W	2.2	8 ₅₄ → 9 ₄₅
105.637 ₆ (79)	{ 105.59 ₀ 105.65 ₈ }	M	{ 136.5 237.2 }	4 ₃₂ → 4 ₄₁ 6 ₁₆ → 6 ₂₅
106.139 ₀ (65)	(106.139 ₀)	W	58.0	5 ₃₃ → 5 ₄₂
107.075 ₆ (96)	(107.075 ₆)	W	47.7	7 ₂₆ → 7 ₃₅
107.738 ₂ (54)	(107.73 ₈)	W	148.2	6 ₃₄ → 6 ₄₃
111.120 ₂ (139)	{ 111.10 ₁ 111.128 ₀ }	M	{ 33.5 172.9 }	7 ₃₅ → 7 ₄₄ 2 ₁₁ → 3 ₂₂

Table 5. (cont)

Observed Frequency, cm ⁻¹	Calculated Frequency, cm ⁻¹	Relative Strength	Calculated Relative Intensity	Assignment
116.595 ₉ (70)	(116.59 ₆)	W	57.7	8 ₃₆ → 8 ₄₅
117.067 ₈ (154)	[117.07]	W	13.1	9 ₄₅ → 9 ₅₄
117.966 ₆ (51)	(117.96 ₇)	W	173.6	7 ₀₇ → 7 ₁₆
120.083 ₈ (134)	(120.083 ₈)	W	418.9	5 ₁₅ → 6 ₀₆
120.504 ₉ (142)	(120.50 ₅)	W	89.2	8 ₂₇ → 8 ₃₆
121.913 ₈ (14) ²	121.90 ₃	W	1303.3	5 ₀₅ → 6 ₁₆

* () average deviation for four observations in 0.0001 cm⁻¹

** () transition used in the determination of the energy levels

*** [] calculated from the energy levels of Ref. 57

† line width very pressure sensitive, frequency quoted is from the lowest pressure observation

1 only observed in one spectrum

2 only observed in two spectra

3 only observed in three spectra

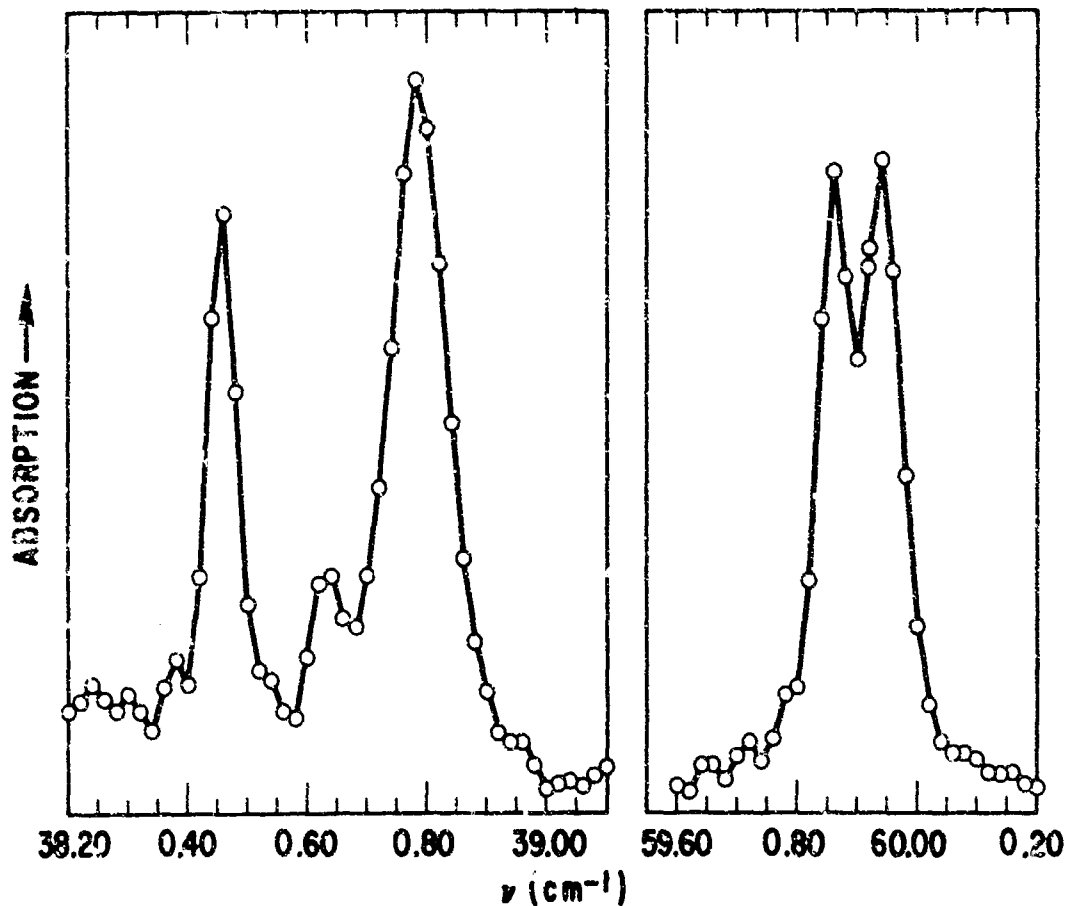


Fig. 4.8. The 38.6 and 59.9 cm^{-1} region of the pure rotational spectrum of water vapor. The circles are the intensity points computed from the interferogram.

strong and medium lines were used in the analysis. The frequencies of peak absorption were computed by the method of zero slope from the computer output. The accuracy of the observed frequencies for strong and medium lines is estimated to be $\pm 0.003\text{ cm}^{-1}$ and slightly more for the weak lines. Frequencies are quoted to 0.0001 cm^{-1} and slightly more for the weak lines. Frequencies are quoted to 0.0001 cm^{-1} only to offset roundoff errors in the analysis. Little confidence is placed in the last figure.

The transitions listed in Table 5 were assigned from calculations based on the energy levels of Gates, et al. (Ref. 57), which were the most recent

complete set of energy levels published. Once the transitions were assigned, new values of the energy levels could be determined by adding up transitions through the levels from the ground state.

Since the water molecule is a b-type asymmetric rotor, selection rules allow only ee-oo and eo-oe transitions, where e and o refer to the evenness or oddness of the limiting prolate and oblate symmetric rotor quantum numbers. This is reflected in the spectrum by two independent sets of transitions. The eo and oe sets cannot combine with the oo and ee sets. Hence, the eo and oe sets cannot combine with the ground state, which is ee. This results in the l_{01} level being the lowest state of the eo and oe levels. The energy difference between the ground state, 0_{00} , energy level and the l_{01} energy level cannot be determined directly. Fortunately, the sum rules of Fraley and Rao (Ref. 58) make possible the calculation of this parameter.

Fraley and Rao (Ref. 58) have developed a set of sum rules for orthorhombic asymmetric molecules that are very useful in the analysis of the pure rotational spectrum of water vapor. These sum rules are:

$$(-1)^J \frac{(ee + eo - oo - oe)}{J(J+1)} = A_o - \frac{1}{4} (T_{aaaa}^o + T_{aa}^o) + 3(aaaaaaaa) \\ + J(J+1) \left[\frac{1}{4} T_{aaaa}^o - 3(aaaaaaaa) \right] \\ + J^2 (J+1)^2 (aaaaaaaa) \quad (13)$$

$$(-1)^J \frac{(ee + oo - eo - oe)}{J(J+1)} = B_o - \frac{1}{4} (T_{bbbb}^o + T_{bb}^o) + \frac{1}{4} T_{bbbb}^o J(J+1) \quad (14)$$

$$(-1)^J \frac{(ee + oe - eo - oo)}{J(J+1)} = C_o - \frac{1}{4} (T_{cccc}^o + T_{cc}^o) + \frac{1}{4} T_{cccc}^o J(J+1) \quad (15)$$

$$\begin{aligned}
 \frac{(ee + oo + oe + eo)}{J(J+1)(2J+1)} = & \frac{1}{3} (A_o + B_o + C_o) - \frac{1}{60} (T_{aaaa}^o + T_{aa}^o + T_{bbbb}^o + T_{bb}^o \\
 & + T_{cccc}^o + T_{cc}^o) + \frac{1}{21} (aaaaaa) + J(J+1) \left[\frac{1}{60} (3T_{aaaa}^o \right. \\
 & \left. + 3T_{bbbb}^o + 3T_{cccc}^o - 2T_{aa}^o - 2T_{bb}^o - 2T_{cc}^o) \right. \\
 & \left. - \frac{1}{7} (aaaaaa) \right] + J^2(J+1)^2 \frac{1}{7} (aaaaaa) \quad (16)
 \end{aligned}$$

The notation ee, for example, stands for the sum of all energy levels of a given J whose limiting prolate and oblate symmetric rotor quantum numbers are both of even parity. A_o , B_o , and C_o are the rotational constants associated with each of the principal axes of the molecule. T_{aaaa}^o , T_{aa}^o , etc., are the quartic distortion constants. (aaaaaa) is the higher order distortion constant. Similar terms for (bbbbbb) and (cccccc) would be added to Eqs. (13) through (15) if analysis showed them to be necessary.

Combinations of these sum rules give four sets of four simultaneous equations, with the energy difference Δ between the 0_{oo} and 1_{ol} energy levels as one of the unknowns. This was done for the transitions presented here giving the result $\Delta = 23.7913 \pm 0.0016 \text{ cm}^{-1}$ as the average for the four sets of equations. This agrees well with the value quoted by Gates, et al. (Ref. 57) of 23.79 cm^{-1} . Having this value, we can calculate the energy of all the eo and oe levels relative to the true ground state.

Because some of the transitions observed here were analyzed as blends of very closely spaced lines and, thus, are unsuitable in the determination of energy levels and since it was desirable to extend the calculations to $J = 7$, it was necessary to use transitions observed by other experimenters. These are listed in Table 6. Two of these are microwave transitions (Ref. 59) and are more accurate than our measurements; seventeen others were

Table 6. Other Transitions Used to Derive Energy Levels

Frequency, cm ⁻¹	Calculated Frequency,* cm ⁻¹	Assignment	Ref.
0.7416830	0.74	5 ₂₃ → 6 ₁₆	59
12.68200	12.68	3 ₂₁ → 4 ₁₄	59
314.74	314.74	3 ₁₂ → 4 ₄₁	52
340.55	340.55	7 ₂₆ → 8 ₃₅	52
349.77	{ 349.79 349.79	6 ₆₁ → 7 ₇₀ 6 ₆₀ → 7 ₇₁	
384.88	384.86	6 ₁₅ → 7 ₄₄	
385.54	385.52	4 ₁₄ → 5 ₄₁	
396.44	396.43	7 ₁₇ → 8 ₂₆	
426.33	426.31	4 ₂₂ → 5 ₅₁	
431.16	431.14	5 ₁₅ → 6 ₄₂	
441.75	441.75	4 ₂₃ → 5 ₅₀	
442.09	442.10	5 ₂₃ → 6 ₅₂	
456.87	456.88	6 ₂₄ → 7 ₅₃	
472.39	472.41	5 ₂₄ → 6 ₅₁	
506.94	506.93	6 ₂₅ → 7 ₅₂	
536.25	536.26	5 ₃₂ → 6 ₆₁	
541.07	541.07	5 ₃₃ → 6 ₆₀	
554.63	554.64	6 ₃₃ → 7 ₆₂	51
567.23	567.23	6 ₃₄ → 7 ₆₁	51

*Energy levels, Ref. 57

taken from the spectra of Rao, et al. (Ref. 52) and Blaine, et al. (Ref. 51) in the 300 to 600 cm^{-1} region. These transitions were unassigned in the original papers. They were chosen and assigned on the basis of frequency and relative intensity calculations (Ref. 56) using the energy levels of Gates, et al. (Ref. 57). The transitions were chosen when calculations indicated that a single, relatively intense transition should occur well separated from its nearest intense neighbors. As can be seen in Table 6 the lines chosen agree with calculated values to within 0.02 cm^{-1} , the quoted accuracy of the other spectra. However, since the accuracy of these frequencies is lower than our measurements, the energy levels derived using these transitions are quoted to one less significant figure.

The energy levels derived from these calculations are given in Table 7, together with values obtained from near-IR vibrational-rotational spectra (Refs. 57, 60, 61). The accuracy of levels determined solely from transitions measured in this work is estimated to be $\pm 0.003 \text{ cm}^{-1}$. These energy levels are indicated by four figures after the decimal point. Energy levels which were determined using transitions from higher frequency spectra are indicated by three places after the decimal point and are estimated to be accurate to $\pm 0.02 \text{ cm}^{-1}$. The energies of the 6_{52} , 6_{51} , 6_{61} , and 6_{60} appear anomalous. Perhaps there was an error accumulating in one of the two series that became obvious only in these almost degenerate levels; or perhaps one of the transitions used in the determination of these levels was misassigned. In general, though, the agreement in the values of the energy levels between this work and the near-IR data is good.

Having determined a complete set of energy levels up to $J = 7$, we can calculate frequencies of other transitions which were not used in the calculations. Table 8 shows a comparison of observed and calculated frequencies for three microwave transitions (Ref. 59). The agreement is within the quoted accuracy of the energy levels. Also, in Table 5, a similar comparison can be made for FIR transitions. Again, the agreement is good.

Table 7. H₂O Energy Levels (cm⁻¹)

J K ₋₁ , K ₊₁	This Work	Fraley (Ref. 60)	Benedict (Ref. 61)	Gates (Ref. 57)
0 ₀₀	0.0000	.000	.00	.00
1 ₀₁	23.791 ₃	.792	.79	.79
1 ₁₁	37.137 ₁	.132	.13	.13
1 ₁₀	42.361 ₉	.366	.36	.37
2 ₀₂	70.088 ₃	.085	.08	.08
2 ₁₂	79.495 ₉	.486	.48	.48
2 ₁₁	95.173 ₈	.167	.15	.17
2 ₂₁	134.902 ₂	.890	.91	.91
2 ₂₀	136.161 ₁	.153	.15	.17
3 ₀₃	136.764 ₉	.751	.77	.77
3 ₁₃	142.274 ₄	.263	.26	.28
3 ₁₂	173.370 ₄	.353	.36	.36
3 ₂₂	206.302 ₆	.280	.28	.30
3 ₂₁	212.162 ₀	.137	.16	.15
3 ₃₁	285.217 ₃	.211	.25	.23
3 ₃₀	285.421 ₁	.410	.40	.43
4 ₀₄	222.049 ₈	.037	.04	.06
4 ₁₄	224.844 ₀	.817	.83	.83
4 ₁₃	275.494 ₄	.481	.52	.52
4 ₂₃	300.367 ₂	.333	.34	.35
4 ₂₂	315.777 ₄	.756	.73	.79
4 ₃₂	382.520 ₀	.495	.49	.52

Table 7. (cont)

$J_{K-1, K+1}$	This Work	Fraley (Ref. 60)	Benedict (Ref. 61)	Gates (Ref. 57)
4_{31}	383.837 ₂	.821	.83	.85
4_{41}	488.11 ₀	.110	.16	.10
4_{40}	488.125 ₆	.136	.17	.13
5_{05}	325.39 ₉	.328	.36	.35
5_{15}	326.620 ₃	.601	.64	.64
5_{14}	399.50 ₇	.440	.45	.46
5_{24}	416.202 ₁	.174	.18	.22
5_{23}	446.56 ₀	.487	.50	.50
5_{33}	503.961 ₅	.938	.98	.00
5_{32}	508.86 ₁	.782	.80	.81
5_{42}	610.100 ₅	.108	.12	.12
5_{41}	610.38 ₄	.334	.34	.35
5_{51}	742.10 ₇	.071	.08	.10
5_{50}	742.11 ₇	.074	.08	.10
6_{06}	446.704 ₁	.671	.66	.71
6_{16}	447.30 ₂	.231	.24	.24
6_{15}	542.890 ₉	.873	.87	.91
6_{25}	552.96 ₀	.880	.92	.92
6_{24}	602.762 ₁	.728	.67	.77
6_{34}	649.02 ₇	.952	.97	.97
6_{33}	661.534 ₃	.514	.56	.56
6_{43}	756.76 ₅	.704	.72	.75
6_{42}	757.78 ₀		.77	.78
6_{52}	888.65 ₀	.602	.61	.60

Table 7. (cont)

$j_{K-1, K+1}$	This Work	Fraley (Ref. 60)	Benedict (Ref. 61)	Gates (Ref. 57)
6 ₅₁	888.59 ₂	.635	.65	.63
6 ₆₁	1045.11 ₁	.045	.09	.07
6 ₆₀	1045.03 ₂	.045	.09	.07
7 ₀₇	586.29 ₅	.213	.28	.26
7 ₁₇	586.46 ₄	.449	.43	.48
7 ₁₆	704.26 ₂	.194	.18	.22
7 ₂₆	709.59 ₄ ₅	.558	.58	.60
7 ₂₅	782.45 ₅	.383	.41	.40
7 ₃₅	816.67 ₀ ₁	.671	.65	.72
7 ₃₄	842.39 ₄	.334	.36	.38
7 ₄₄	927.77 ₁	.723	.76	.77
7 ₄₃	931.27 ₂	.228	.23	.22
7 ₅₃	1059.63 ₂		.62	.65
7 ₅₂	1059.90 ₀	.824	.83	.85
7 ₆₂	1216.16 ₄	.199	.19	.20
7 ₆₁	1216.25 ₇	.199	.19	.20
7 ₇₁	1394.80 ₂	.815	.91	.86
7 ₇₀	1394.88 ₁	.815	.91	.86
8 ₂₇	885.64 ₂	.569	.62	.62
8 ₂₆	982.90 ₄		.92	.91
8 ₃₆	1006.14 ₇	.090	.14	.12
8 ₃₅	1050.14 ₄		.20	.15
8 ₄₅	1122.74 ₃	.694	.78	.72
8 ₄₄	1131.76 ₂		.78	.76

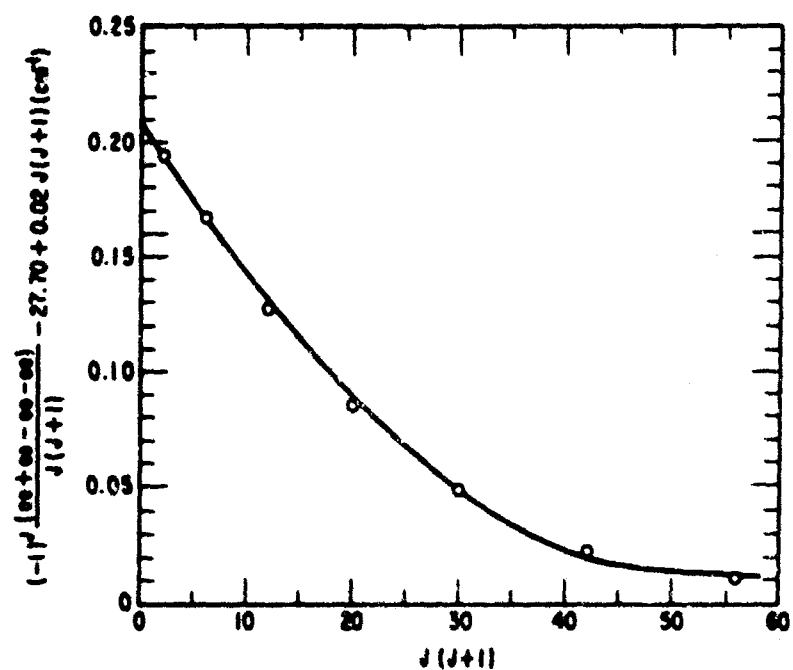


Fig. 29. The sum rule plot for the "a" axis of the water molecule. The quantity $[27.70 - 0.02 J(J+1)] \text{ cm}^{-1}$ has been subtracted from sums to make the curvature more apparent.

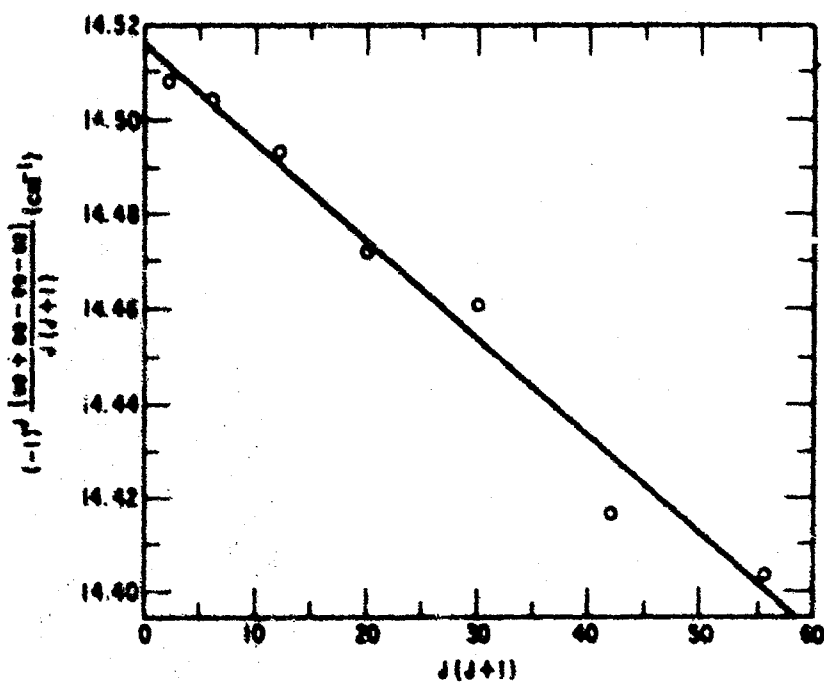


Fig. 30. The sum rule plot for the "b" axis of the water molecule.

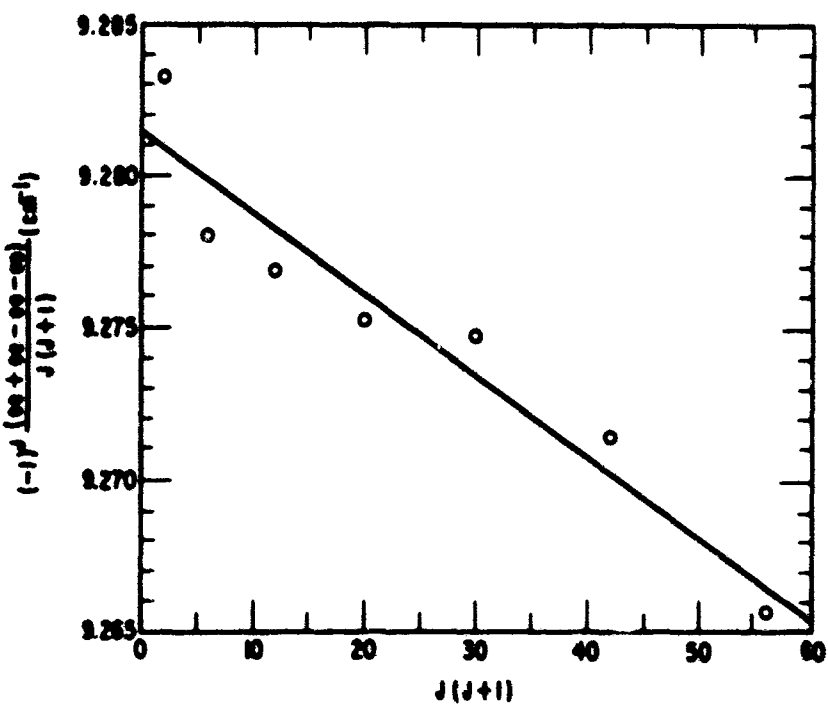


Fig. 31. The sum rule plot for the "c" axis of the water molecule.

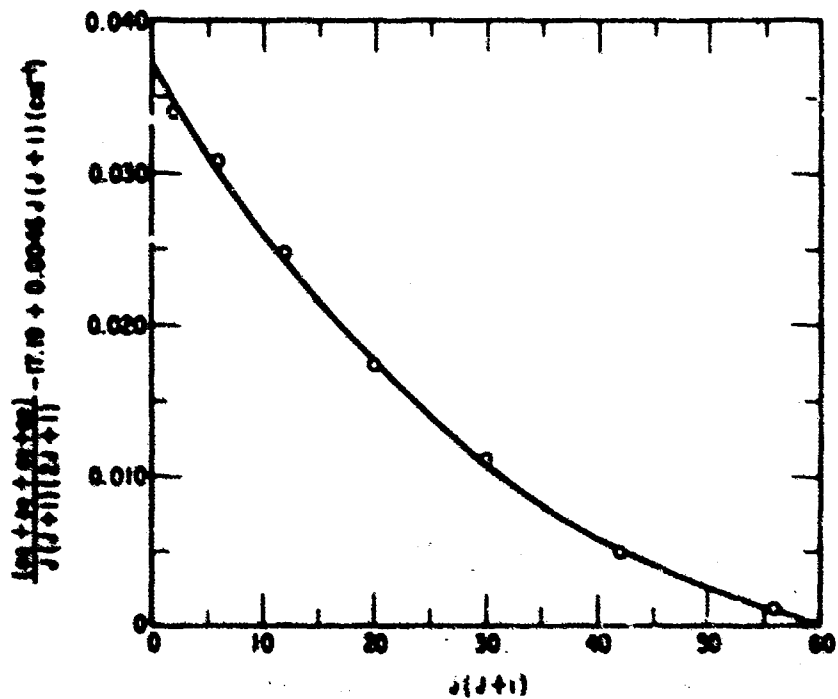


Fig. 32. The sum rule plot for the combination of all axes of the water molecule.

Table 8. Comparison of Observed and Calculated Microwave Transitions of Water Vapor

Observed (Ref. 59), cm ⁻¹	Calculated, cm ⁻¹	Assignment
6.114549	6.113 ₃	2 ₂₀ → 3 ₁₃
10.84596	10.842 ₉	4 ₂₂ → 5 ₁₅
14.94370	14.946 ₁	3 ₃₀ → 4 ₂₃

Also, with a complete set of energy levels the sum rules of Fraley and Rao can be used to determine the rotational constants. Plots of the sum rules are shown in Figs. 29 to 32. Only the plots in Figs. 29 and 32, which are associated with the a-axis of rotation, show significant curvature. This indicates that the data can give a significant value for the higher order distortion constants only for the a-axis (aaaaaaa).

Least squares fits to the sum rules shown in Eqs. (13) through (16) resulted in the values shown in Table 9. The errors quoted are 95% confidence intervals. The following formulas (Ref. 58) applicable to planar orthorhombic molecules are used to obtain the remaining quartic distortion constants and the rotational constants:

$$T_{aabb} = T_{aaaa} \left(\frac{-B_e^2}{2A_e^2} \right) + T_{cccc} \left(\frac{A_e^2 B_e^2}{2C_e^4} \right) \\ + T_{bbbb} \left(\frac{-A_e^2}{2B_e^2} \right) \quad (17)$$

Table 9. Parameters Derived from Least Squares Fits
to the Sum Rules of Fraley and Rao (cm^{-1})

$$A_o - \frac{1}{4} T_{aa}^o = 27.8801 \pm 0.0034$$

$$B_o - \frac{1}{4} T_{bb}^o = 14.5134 \pm 0.0090$$

$$C_o - \frac{1}{4} T_{cc}^o = 9.2813 \pm 0.0021$$

$$T_{aaaa}^o = -0.0084 \pm 0.0012$$

$$T_{bbbb}^o = -0.0083 \pm 0.0012$$

$$T_{cccc}^o = -0.00107 \pm 0.00027$$

$$(aaaaaa) = (6.89 \pm 0.26) \times 10^{-5}$$

$$(bbbbbb) \approx (cccccc) \approx 0$$

$$A_o + B_o + C_o = 51.6742 \pm 0.0027$$

$$T_{aa}^o + T_{bb}^o + T_{cc}^o = -0.00829$$

$$(aaaaaa) + (bbbbbb) + (cccccc) = (6.02 \pm 0.98) \times 10^{-5}$$

$$T_{aacc} = T_{aaaa} \left(\frac{C_e^2}{2A_e^2} \right) + T_{bbbb} \left(\frac{-A_e^2 C_e^2}{2B_e^4} \right) + T_{cccc} \left(\frac{A_e^2}{2C_e^2} \right) \quad (18)$$

$$T_{bbcc} = T_{aaaa} \left(\frac{-C_e^2 B_e^2}{2A_e^4} \right) + T_{bbbb} \left(\frac{C_e^2}{2B_e^2} \right) + T_{cccc} \left(\frac{B_e^2}{2C_e^2} \right) \quad (19)$$

$$T_{aa}^0 = T_{\beta\beta\gamma\gamma}^0 - T_{\gamma\gamma aa}^0 - T_{aa\beta\beta}^0 \quad (20)$$

The subscript e refers to equilibrium values of the rotational constants that are related to the ground and excited state constants by relations of the following type:

$$A_v = A_e - \sum_i a_i (v + \frac{1}{2}) \quad (21)$$

where v is the vibrational quantum number and sum is over the fundamental vibrations of the molecule. The a's and equilibrium rotational constants were evaluated by weighted least squares fits to our values of ground state constants plus approximately 40 excited-state constants given by Benedict (Ref. 62). The results of these analyses are given in Table 10. With these values of the equilibrium rotational constants, the remaining quartic distortion constants and the ground state rotational constants can be calculated. The results of these calculations are given in Table 11. The errors quoted are 95% confidence intervals. The values of the ground state rotational constants (Ref. 62) as determined from the vibrational-rotational spectrum are also included. The agreement is excellent. Also included are calculated values of the six quartic distortion constants. These were calculated from relations given by Kivelson and Wilson (Ref. 63) between vibrational force constants and the distortion constants. The force constants were determined

Table 10. Equilibrium Rotational Constants
(cm⁻¹)

	$A_e = 27.1107$		
	$B_e = 14.5922$		
	$C_e = 9.5120$		
	A	B	C
a_1	0.9168	0.2075	0.1694
a_2	-3.4957	-0.1561	0.1387
a_3	1.1418	0.1096	0.1467

from the harmonic frequencies of H₂O and D₂O given by Benedict, et al. (Ref. 64). The agreement between observed and calculated values of the quartic distortion constants is quite good. It should be noted that the six values are not linearly independent. They are linear combinations of four independent values.

5. LINE WIDTH

a. Direct From Interferogram

As was mentioned previously (Sections II and III-A) the fall-off of intensity in an interferogram is due in a large measure to the width(s) of the lines in the spectrum. If the lines of the spectrum are very nearly evenly spaced, then it will be the signatures that are damped out as $\sim \exp -2\pi x \epsilon$ (Ref. 22).

A number of interferograms (conditions of different pressures) were obtained for CO in a 15-cm absorption cell (see Fig. 19).

Table 11. Ground State Rotational Constants
of the Water Molecule

This Work	Previous Work (Ref. 62)
$A_O = 27.8761 \pm 0.0034$	27.877
$B_O = 14.5074 \pm 0.0090$	14.512
$C_O = 9.2877 \pm 0.0021$	9.285
This Work	Calculated
$T_{aaaa}^O = -0.1084 \pm 0.0012$	-0.1088
$T_{bbbb}^O = -0.0083 \pm 0.0012$	-0.00672
$T_{cccc}^O = -0.00107 \pm 0.00027$	-0.00093
$T_{aabb}^O = +0.01985$	+0.01846
$T_{aacc}^O = -0.00491$	-0.00515
$T_{bbcc}^O = -0.00108$	-0.00077
$T_{aa}^O = -0.01602$	
$T_{bb}^O = -0.02368$	
$T_{cc}^O = +0.02584$	
$[aaaaaa] = (6.89 \pm 0.26) \times 10^{-5}$	
$[bbbbbb] \approx [cccccc] \approx 0$	

NOTE: Only four of the $T_{\alpha\beta\gamma\delta}^O$ are independent, the others being linear combinations of these.

In the analysis of the signatures, the intensity was taken as the average between the largest maxima and two adjacent minima. The first through the ninth signatures were used. The zeroth signature was not used because any imbalance between the reference beam and sample beam would be most evident here (i.e., in the neighborhood of $x = 0$, zero optical path difference). Signatures beyond the ninth were not used for reasons discussed later in this section. The resulting intensities were normalized to the first signature intensity and then the natural logarithms of these relative intensities were plotted as a function of x . (The x 's were taken where the largest maximum of the signature occurred.)

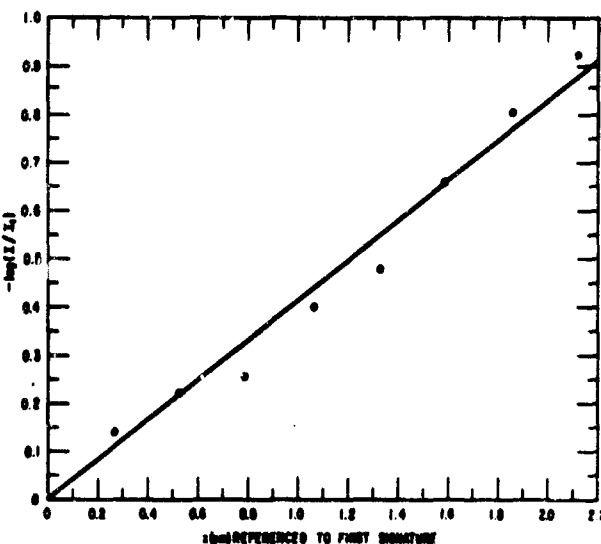


Fig. 33. The natural logarithm of the reduced optical path difference for CO ($l = 15$ cm, $p = 521$ Torr).

The resulting graph is a straight line, within the experimental error, and its slope is $2\pi\epsilon$. A typical result is shown in Fig. 33.

This procedure was carried out for four runs at pressures of 521, 440, 375, and 254 Torr. The ϵ 's obtained were: 0.065 ± 0.004 , 0.057 ± 0.003 , 0.047 ± 0.005 , and $0.033 \pm 0.004 \text{ cm}^{-1}$, respectively. These results are shown in Fig. 34, where ϵ is plotted as a function of

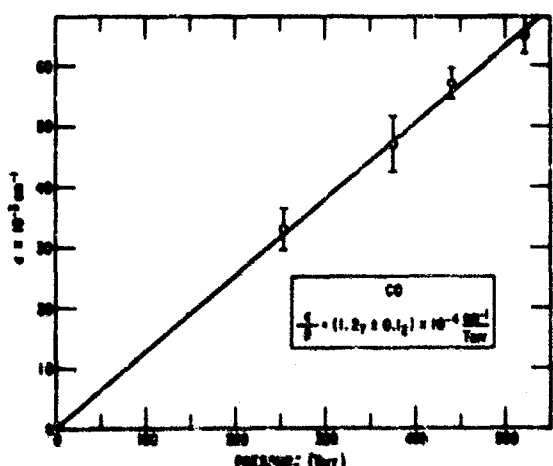


Fig. 34. Linewidth parameter versus pressure for CO.

pressure. The result is a straight line whose intercept is the origin, within experimental error. The slope is $\epsilon/p = (1.27 \pm 0.12) \times 10^{-4} \text{ cm}^{-1}/\text{Torr}$. The microwave value for ϵ/p is $(1.17 \pm 0.07) \times 10^{-4} \text{ cm}^{-1}/\text{Torr}$ and the microwave data (Ref. 65) were obtained at a pressure of less than 1 Torr. Although the two results are in agreement within the experimental error, the discussion to follow will show that the value obtained from the interferometry data should be larger than the microwave value and indeed represents an average upper limit for this parameter.

In general, this method is subject to the following systematic errors:

First, the signature shape is distorted because CO (or any other molecule for that matter) is not a rigid rotor. Thus, its pure rotational spectrum consists of lines that are not exactly equally spaced in wavenumber. (If the rotational lines were exactly equally spaced, the signatures would be symmetric and undistorted.) The lines converge slowly due to centrifugal distortion effects, and this is sufficient to distort the signatures so that the fall-off in intensity is greater than is expected from the $\exp(-2\pi x \epsilon)$ factor alone. The method used for measuring the intensities compensates for this distortion to some extent; however, comparison between calculated signature shapes including and neglecting the centrifugal stretching term indicate the intensities of the higher signatures (8th, 9th, etc.) were underestimated by ~5% (Ref. 22). The distortion of the signatures becomes more pronounced as one goes to higher signatures at larger x .

Second, the lines are assumed to be Lorentzian with a Lambert-Beer's Law for absorption. That is $I = I_0 e^{-\gamma(v)L}$ where $\gamma(v)$ is the Lorentz line shape function and L is the absorption path. In Ref. 22 it is shown that, when the exponential is expanded in a power series, the effect of the higher order terms (3rd and beyond) yields a factor that will decrease the intensity of the signatures in addition to the $\exp(-2\pi x \epsilon)$ factor. Again this becomes more important as one goes to signatures at larger x .

Because of these two errors, only signatures one through nine were used in the analysis, that is, signatures of relatively small x .

Third, in general the lines will have different widths because of possible rotational resonances (Ref. 66) and Doppler broadening. For a temperature of 295°K, $\epsilon_d(J = 0 \rightarrow 1) \sim 0.05 \times 10^{-4} \text{ cm}^{-1}$ and the $J = 19 \rightarrow 20$ transition, it will be $\sim 1.0 \times 10^{-4} \text{ cm}^{-1}$. Our measurements were at pressures corresponding to ϵ of 0.03 to 0.07 cm^{-1} ; therefore, the Doppler broadening is negligible.

Fourth, there is the problem of instrumental broadening (in interferometers due to finite entrance and exit apertures, and the usual optical problems, parallelness of the two grating faces, etc.). The corresponding problem for conventional spectrometers is a very great one and in fact extensive "slit width" corrections must be made, since often the width of the lines under investigation is much narrower than the band of radiation passed by the entrance and exit slits. From the data presented here (i.e., the fact that the ϵ vs p curve extrapolates through the origin well within the experimental error), it is apparent that any instrumental broadening is within the experimental error.

The result obtained may therefore be considered an average upper limit for the line width parameters of CO, as all the major systematic errors tend to give a larger ϵ value.

b. From the Spectrum

The preceding treatment is valid as long as each of the lines have the same line width parameter and the absorption is not too strong; even then it is applicable only to diatomic and linear molecules, and the result is an average value.⁸ The more practical and interesting cases are those where

⁸ Individual lines can be studied by using a numerical filtering technique discussed by Connes (Ref. 67). Essentially this involves convolving the interferogram (obtained between, say, 0 and $v_c \text{ cm}^{-1}$) with the mathematical function that is the Fourier transform of an ideal filter passing all the radiation between v_1 and v_2 (the region of interest) and none of the radiation outside this range. The result of this convolution is the interferogram one would have obtained if the input radiation had been physically filtered by a filter having the characteristics of the ideal filter. In this way, single lines may be studied and the necessary correction for the systematic errors may be applied more easily.

the maximum absorption is strong and the line widths do vary. The following is a discussion of some preliminary results obtained for the pure rotational spectrum of CO.

A beam of radiation traversing a length l of an absorbing medium will absorb intensity according to the well-known Lambert-Beer's Law, and the intensity passed $I(\nu)$ can be written

$$I(\nu) = I_0(\nu)e^{-\gamma(\nu)l} \quad (22)$$

where $I_0(\nu)$ is the incident intensity and $\gamma(\nu)$ is the absorption coefficient. As discussed in Section III, a two-beam interferometer operating in a double-beam differencing mode does not measure $I(\nu)$ and in fact gives little information about $I_0(\nu)$. What is measured is $I_\Delta(\nu)$, and it is

$$I_\Delta(\nu) = I_0(\nu) - I(\nu) = I_0(\nu)[1 - e^{-\gamma(\nu)l}] \quad (23)$$

Now, aside from the fact that little is known about $I_0(\nu)$ from a double-beam run, the measurement of intensities in the FIR is fraught with other difficulties (see Section V). Thus, we shall restrict ourselves to a discussion of what information is available from $I_\Delta(\nu)$, making only the assumption that $I_0(\nu)$ does not change radically⁹ over small intervals of ν . Differentiating $I_\Delta(\nu)$ with respect to ν yields

$$\frac{dI_\Delta(\nu)}{d\nu} = [1 - e^{-\gamma(\nu)l}] \frac{dI_0(\nu)}{d\nu} + I_0(\nu)e^{-\gamma(\nu)l} \left[-l \frac{d\gamma(\nu)}{d\nu} \right]$$

⁹In this respect, it has been our experience that the largest variation of $I_0(\nu)/\text{cm}^{-1}$ is caused by the channel spectrum from the lamp envelope of the source (see Section V).

and if $I_0(v)$ is a constant in the region of interest

$$\frac{dI_\Delta(v)}{dv} = -I_0 e^{-\gamma(v)t} \frac{dy(v)}{dv}$$

Differentiating again with respect to v we obtain

$$\frac{d^2 I_\Delta(v)}{dv^2} = I_0 \left[t^2 \left(\frac{dy(v)}{dv} \right)^2 - , \frac{d^2 y(v)}{dv^2} \right] e^{-\gamma(v)t} \quad (24)$$

For pure rotational spectra the Lorentz form of $\gamma(v)$ has been found to be a good approximation to the line shape, at least in the region of maximum absorption. It is given by¹⁰

$$\gamma(v) = \frac{A\epsilon}{(v - v_0)^2 + \epsilon^2} \quad (25)$$

Now the maximum of $I_\Delta(v)$ occurs when

$$\frac{dI_\Delta(v)}{dv} = 0 \quad \text{or when } v = v_0$$

Therefore, v_0 is determined by finding where the slope of $I_\Delta(v)$ is zero. Information about A or ϵ is neither determined nor required. Equation (24) yields, when set to zero,

$$\epsilon^4 - 2\epsilon^2(v - v_0)^2 + 2At(v - v_0)^2\epsilon - 3(v - v_0)^4 = 0 \quad (26)$$

¹⁰This will be a good approximation as long as $v_0 \gg \epsilon$; i.e., the lines are sharp and the pressure of the absorbing gas not so high as to make three or more body collisions important with respect to two body collisions.

The values of ν where this equation is satisfied are where $dI_{\Delta}(\nu)/d\nu$ has its maximum and minimum values. In fact, for a symmetrical line they are equally displaced about ν_0 . We define

$$\Delta\nu_D = |\nu - \nu_0|$$

for those two values of ν which satisfy Eq. (26). The quantity $\Delta\nu_D$ is the wavenumber difference between ν_0 and where $dI_{\Delta}(\nu)/d\nu$ has its extreme values. Dividing Eq. (26) by $(\Delta\nu_D)^4$ and letting $y = (\epsilon/\Delta\nu_D)$ and $Q = Al/\epsilon$, we obtain

$$y^4 - 2y^2(1 - Q) - 3 = 0 \quad (27)$$

Now Q is the maximum absorption coefficient times the absorbing path length l and, in general, may range from near zero to very large numbers. Since Q cannot be negative and $y = \epsilon/\Delta\nu_D$ is also a positive quantity, the only root of Eq. (27) having physical significance is

$$y = \{1 - Q + [(1 - Q)^2 + 3]^{1/2}\}^{1/2} \quad (28)$$

For $Q \approx 0$, the weak absorption case, $y = 3^{1/2}$ or $\epsilon = 3^{1/2} \Delta\nu_D$, which is the relation usually used in the microwave region (Ref. 68). For $Q > 0$, $\epsilon < 3^{1/2} \Delta\nu_D$.

Now Eq. (26) can be solved for ϵ if $\Delta\nu_D$, A , and l are known. Now $\Delta\nu_D$ can be measured (see discussion on the CO pure rotational spectrum in this section), and l is known from the experiment. The parameter A is a function of pressure, population of the states involved in the transition (upper state also since stimulated emission is not negligible in the FIR, a thermodynamic equilibrium is assumed however), the dipole moment of the molecule, etc. An explicit formula for A is given in Townes and Schawlow (Ref. 66). Thus

if this information is known, A may be calculated. If this is not the case, then it is still possible to get ϵ by making two runs at different values of I . Then two Eqs. (26) will result and the factor involving A can be eliminated. The resulting equation will have ϵ as a function of $(\Delta\nu_D)_1$, $(\Delta\nu_D)_2$ and the ratio (I_1/I_2) .

In practice it is necessary to correct the measured $\Delta\nu_D$, since in general the resolution of the interferometer is finite and, thus, the line shape observed will be the true line shape convolved with the scanning function of the interferometer. As might be expected, the raw $\Delta\nu_D$ (L finite) is larger than the true $\Delta\nu_D$ ($L \rightarrow \infty$). For $Af/\epsilon \ll 1$, a correction curve of the form $(\Delta\nu_D)_L/(\Delta\nu_D)_\infty$ vs $L\epsilon$ can be plotted and is shown in Fig. 35. Plotted also is $\epsilon_L/\epsilon_\infty$ vs $L\epsilon$. As is seen this quantity changes very slowly with L , and thus a reasonable value of ϵ_∞ is obtained directly from the spectrum; L is known and, therefore, the correction factor can be determined.

Such a correction curve is inadequate when (Af/ϵ) is not small compared with one. We have calculated correction curves for various values of (Af/ϵ) . A typical case is shown in Fig. 36.

Preliminary results for the pure rotational spectrum of CO are shown in Fig. 37. The results have been normalized to 1-atm pressure (assuming ϵ varies linearly proportional to pressure). The solid lines are curves from a theoretical calculation (Ref. 69) of self-broadened line widths for linear molecules.

Because the dipole moment of CO is so small (0.112 Debye), it is the quadrupole moment Q that is responsible (at least for low J) for the pressure broadening. Although the data points have considerable scatter, a value of Q somewhat less than 4×10^{-26} esu is indicated.

6. ABSORPTION OF GASES IN THE MEDIUM PRESSURE RANGES (~1-10 atm).

The preliminary results of line width measurements have pointed out the desirability of making measurements at higher pressures. In the low to medium pressure range (where only two body collisions are important)

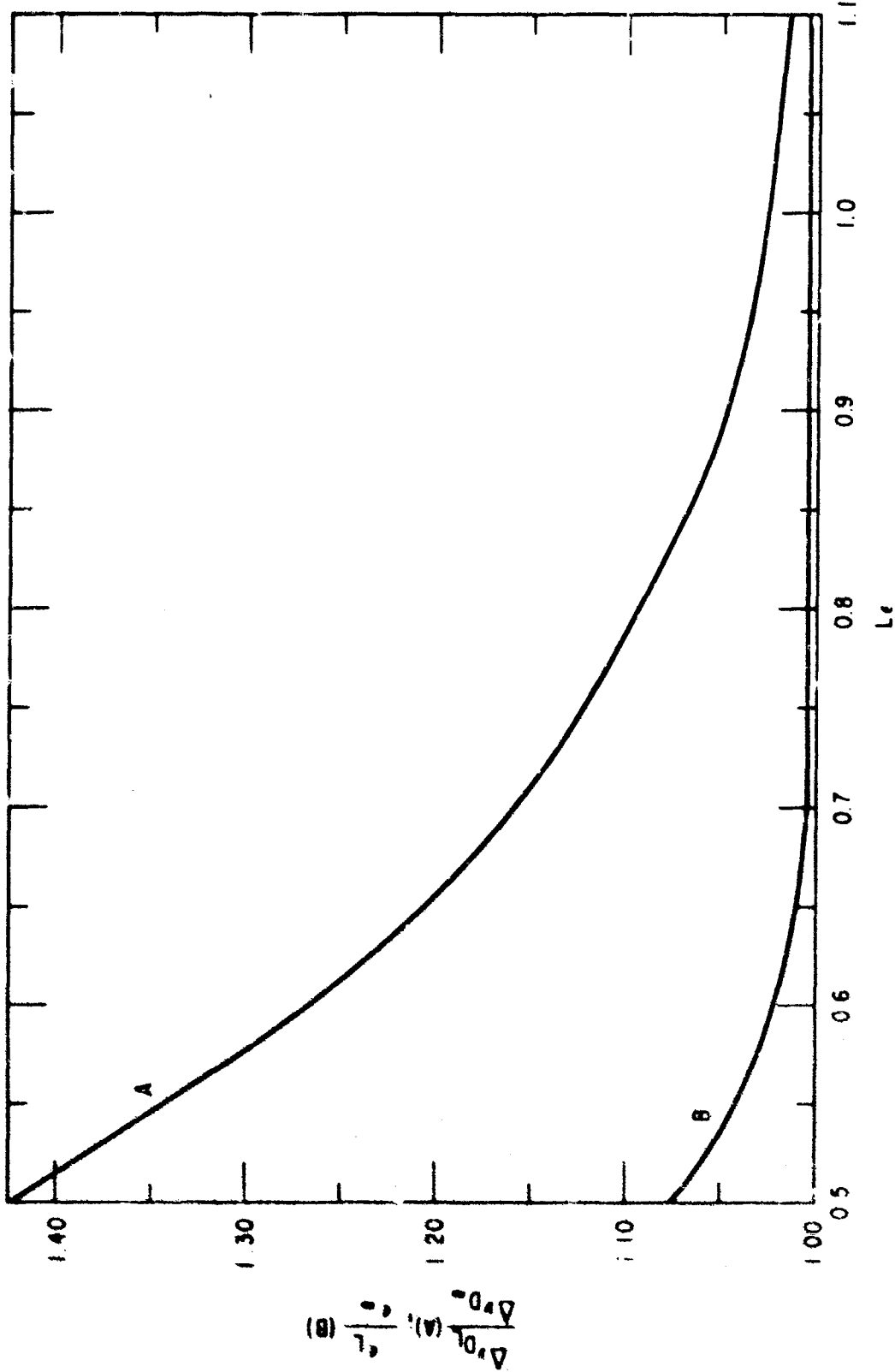


Fig. 35. Correction curve for (Δv_D) due to finite resolution for weakly absorbing lines, curve A. Curve B is the variation of $\epsilon_L/\epsilon_\infty$. See text.

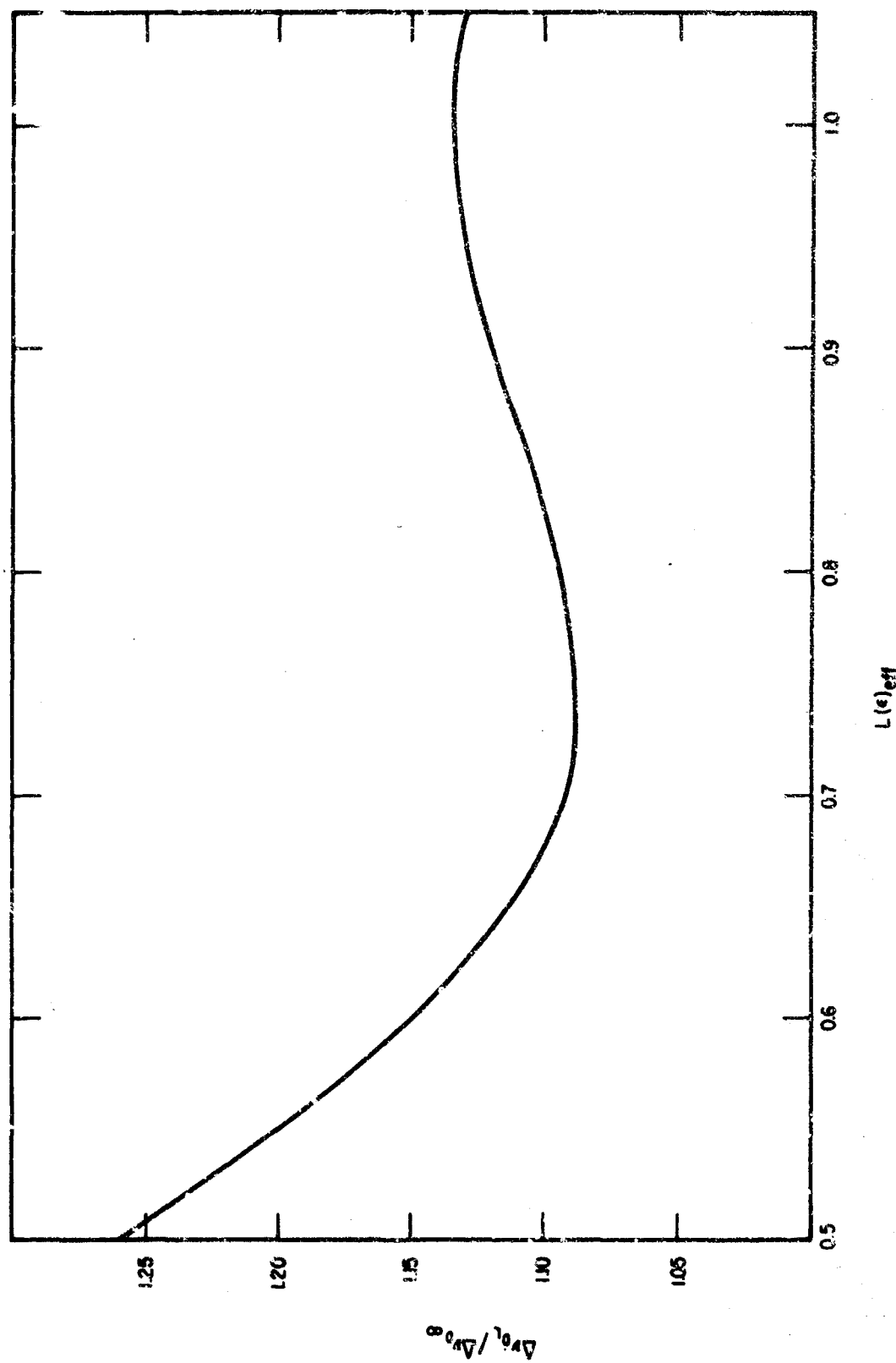


Fig. 36. Correction curve for $(\Delta\nu D)$ due to finite resolution for medium absorbing lines ($A\ell / \epsilon = 3, 2813$).

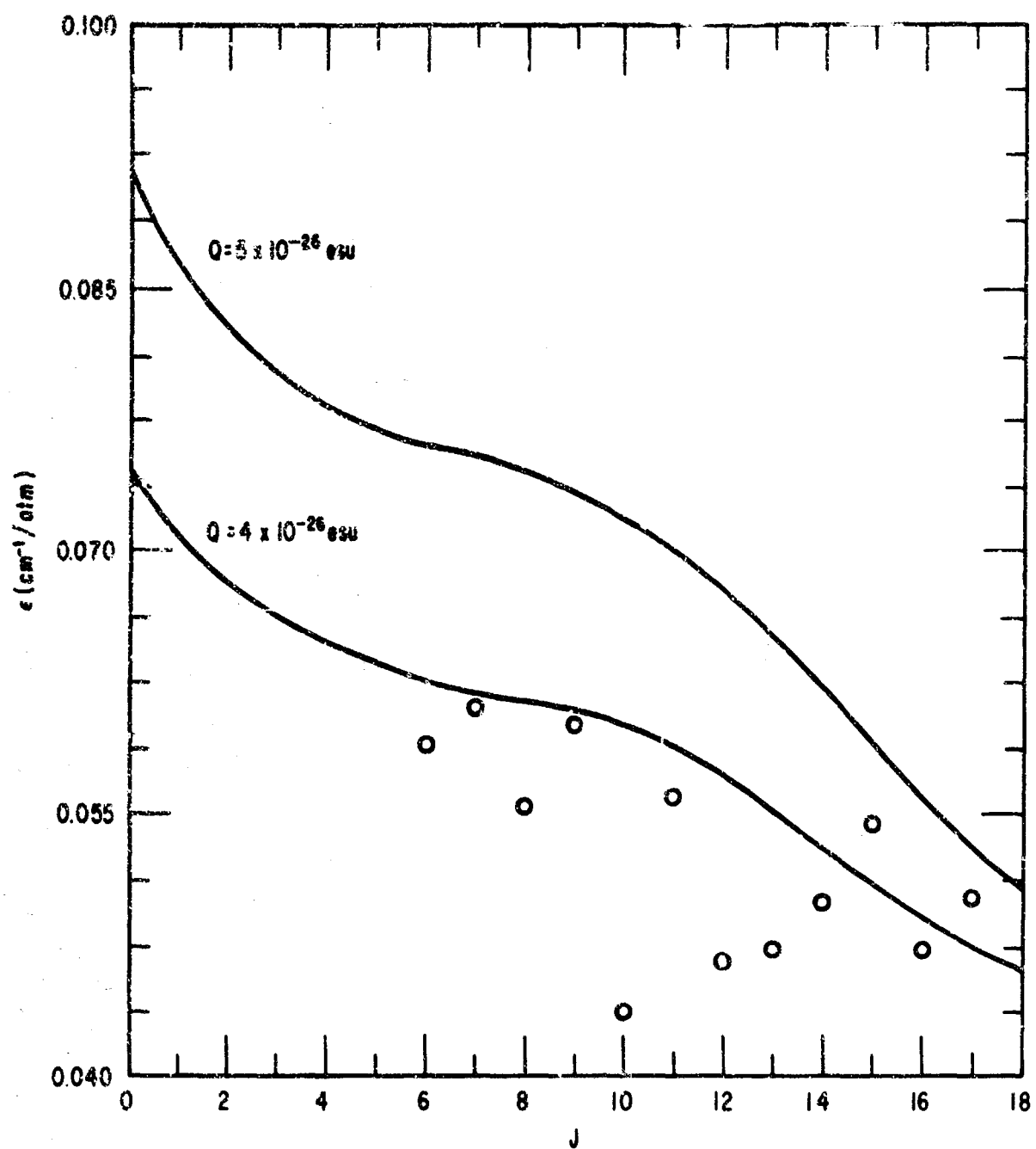


Fig. 37. Preliminary line widths (self-broadened) for the pure rotational lines of CO. The solid curves are theoretical curves for the quadrupole moment of CO equal to 5×10^{-26} esu and 4×10^{-26} esu.

studies in the near-IR (vibration-rotation spectra) and microwave (usually low J pure rotational spectra) region, it has been found that the absorption lines are broadened linearly with pressure. At higher pressures (where three or more body collisions become important), the lines are broadened in an asymmetric manner (i.e., the line shape is no longer symmetric about the peak absorption). It has also been observed that the lines are shifted in wavenumber because of the increased pressure. Most of these studies have been carried out in the near-IR (Ref. 70).

Before the development of two-beam interferometers for the FIR, such investigations were not feasible since the S/N was so poor as to preclude using narrow enough slits in conventional spectrometers to make studies on line shapes. Usually only investigations reporting wavenumber measurements were carried out. The performance of the Aerospace FIR lamellar grating has indicated that some of these studies are now feasible. A small cell has been designed, fabricated, and tested in the 1 to 10 atm range. A photograph of this cell is shown in Fig. 38. It has a clear circular aperture of ~2.5 cm diam and an absorption length of ~6.5 cm. Some preliminary tests have been made with CO in the absorbing cell, but no analysis or measurements have been made.

Fig. 38. Absorption cell for medium pressures (~1 to 10 atm)

B. OPTICAL CONSTANTS OF SOLIDS

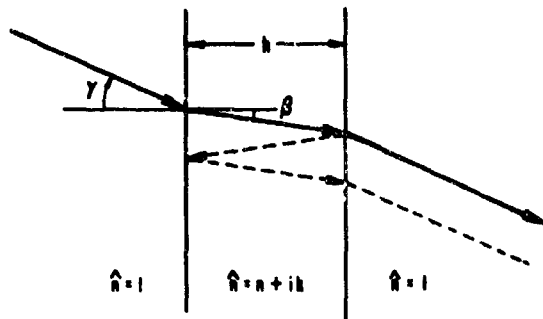
The index of refraction of optical materials is commonly measured by a variety of techniques for wavelengths in the visible and near visible

regions. In the FIR spectral region (80 to 500μ , 20 to 125 cm^{-1}) most of these methods are not used either because they are not feasible in this spectral region or because they require special equipment that has not been developed. An exception is the channel spectrum technique in which the radiation is multiply reflected between the faces of a flat sample so that interference in the transmitted beam produces a spectrum consisting of a series of maxima nearly equally spaced in frequency ("channels"). The maxima occur at those wavelengths for which the optical thickness of the sample is an integral number of half wavelengths; hence, from wavelength and thickness measurements, the index of refraction can be determined.

Interferometers are admirably suited to this determination since they are fundamentally wavelength-measuring devices. In the FIR region, they are superior to grating type instruments because of their high sensitivity and spectral resolution. In recent years the required instrumentation and techniques have been developed to a high degree (Refs. 8, 9, 71, 72). The application of the Aerospace Corporation lamellar grating interferometer to the measurement of refractive indices is discussed here.

The transmittance of a material is determined by its index of refraction. This index, in general, must be complex to account for absorption within the material. The channel spectrum technique is effective for determining the index, provided the absorption is not too large. The energy transmitted through the sample can be calculated in the following manner for the geometry of Fig. 39. Let $\hat{n} = n + ik$ be the complex index, $r = (n - 1)/(n + 1)$ be the amplitude reflectance and $t = 2/(n + 1)$ be the transmittance at each surface. Then

$$A(\nu) = t^2 \left[1 + \sum_{l=1}^{\infty} r^{2l} e^{i(2\pi l + 2\hat{n}\nu h \cos \beta + \delta)} \right] \\ \equiv t^2 (1 + \sum r^{2l} e^{il\sigma}) \quad (29)$$



is the vector sum of the amplitudes of the transmitted components. Here

ν is the wavenumber

h is the sample thickness

β is the angle between normal to the sample surface and the ray within the medium, and

δ is the phase shift produced by absorption within the medium.

The energy transmittance

$$T(\nu) = A \cdot A^* \quad (30)$$

Fig. 39. Geometry of sample for channel spectrum index of refraction measurements.

has been derived in many forms (Ref. 21). Here, where we are interested in the general solution with absorbing materials, and where the measurement is made by Fourier transform methods, it is convenient to express this transmittance by (Ref. 8)

$$T(\nu) = \tau(\nu) \left(1 + 2 \sum_{l=1}^{\infty} \rho^l \cos l\theta \right) \quad (31)$$

where

$$\begin{aligned} \tau(\nu) &= \frac{\left| \frac{4n}{(n+1)^2} \right|^2 \exp(-\alpha h / \cos \beta)}{1 - \rho^2} \\ &= \frac{16(n^2 + k^2) \exp(-\alpha h / \cos \beta)}{\{[(n+1)^2 + k^2]^2 (1 - \rho^2)\}} \end{aligned} \quad (32)$$

$$\rho = \frac{[(n - 1)^2 + k^2]}{[(n + 1)^2 + k^2] \exp(\alpha h \cos \beta)} \quad (33)$$

$$\theta = 4\pi nhv \cos \beta + \delta = 4\pi nhv \cos \beta + \tan^{-1} \left(\frac{2k}{n^2 + k^2 - 1} \right) \quad (34)$$

and $\alpha = 4\pi kv$ is the customary absorption constant. The more familiar form of Eq. (31) in terms of the same parameters is $T(v) = \tau(v) (1 - \rho^2) / (1 + \rho^2 - 2\rho \cos \theta)$. ρ is significant in that it is the fraction of the energy that survives two reflections and two transmittances through the sample. The angle of the beam within the sample β is related to the external angle γ by Snell's law, which becomes, when solved for $\cos \beta$ for a sample of complex index

$$\cos^2 \beta = \frac{1}{2} \left\{ 1 - \frac{\sin^2 \gamma}{n^2} + \left(\frac{k}{n} \right)^2 + \left[\left(1 - \frac{\sin^2 \gamma}{n^2} - \left(\frac{k}{n} \right)^2 \right)^2 + \left(\frac{2k}{n} \right)^2 \right]^{1/2} \right\} \quad (35)$$

$\tau(v)$ is the average transmittance that would be observed if there were no interference, i.e., it is the scalar sum of the transmitted energies.

Equation (33) is obviously the Fourier cosine series expansion of $T(v)$, i.e.,

$$T(v) = \sum_{l=0}^{\infty} A_l \cos l\theta$$

where

$$A_0 = \tau(v) , \quad A_{l \neq 0} = 2\tau(v)\rho^l$$

Because the interferometer used for these measurements generates an "interferogram" that is the Fourier transform of $T(v)$ (multiplied by the source function), Eq. (33) is a very convenient form to work with. The interferogram function (see Section II) can be written as

$$F(x) = \int_0^\infty \tau(v)(1 + 2\sum_l \rho^l \cos l\theta) \cos 2pxdv$$

where x is the optical path difference in the interferometer. In this equation the source function has been absorbed into $\tau(v)$ and the constant term in the interferogram has been dropped. If $\tau(v)$ and ρ were constant and v extended from zero to infinity, $F(x)$ would simply consist of a series of δ -functions with coefficients A_l located at $x = l\theta/2\pi$. For a finite range of θ , these δ functions are broadened into sinc ($= \sin x/x$) functions, which are further distorted by the nonconstancy of τ and ρ .

These distorted sinc functions have been given the name of "signatures". Since they contain all the available information about the sample,¹¹ it is

¹¹Here we note that the modular resolution definition is the appropriate one, since no "channels" in the observed spectrum will be seen unless at least the first signature is observed.

possible to replace the interferogram between signatures by a constant, thus eliminating a major fraction of the recorded noise without significantly distorting the spectrum obtained from the transformed interferogram.

From Eq. (31) it is evident $T(\nu)$ will be a maximum when all the cosine terms in the sum are in phase; i. e., when $\theta = m \cdot 2\pi$, where m is an integer, from which

$$2\nu h \cos \beta + \frac{\delta}{2\pi} = m \quad (36)$$

This leads to a series of maxima equally spaced in ν , provided n is constant. From measured values of these ν_{max} and the other parameters in Eq. (36), it is possible to calculate $n(\nu)$. The phase shift δ can be neglected for the first approximation.

From a measured mean transmittance and the above index value, the absorption coefficient $\alpha = 4\pi\nu k$ can be calculated (see Eq. (32), which in turn can be used to determine δ (see Eq. (34) so that a corrected n can be found). The process can be repeated if necessary until n and k achieve stationary values.

This method is limited by the requirement that the sample be transparent enough that a significant fraction of the radiation can survive at least two internal reflections and three passes through the sample. We now make some semiquantitative estimates of the maximum thickness permitted for a given n and absorption coefficient. For a difference spectrum (see Section III-C) the noise can be as low as $10^{-3} E_0$, where E_0 is the source intensity. For $n < 4$ the amplitude of the channels may be approximated by $2\tau(\nu)pE_0$, the first term in the series of Eq. (31), which is the contribution of the first pair of internal reflections. (The $\tau(\nu)$ term is removed in the differencing technique.) Assuming a S/N of at least 2 is needed to make meaningful measurements, then $2\tau(\nu)p > 2 \times 10^{-3}$. For the absorption constants and

frequencies involved, $k \ll n$, and an adequate approximation becomes

$$e^{-2\alpha h} < 10^{-3} \frac{(n+1)^2(n^2+1)}{n(n-1)^2}$$

Figure 40 gives, as a function of the absorption constant, α , the maximum value of h which satisfies this relation, with the refractive index as a parameter.

We now turn to an analysis of the accuracy with which the parameters needed for calculating n can be determined.

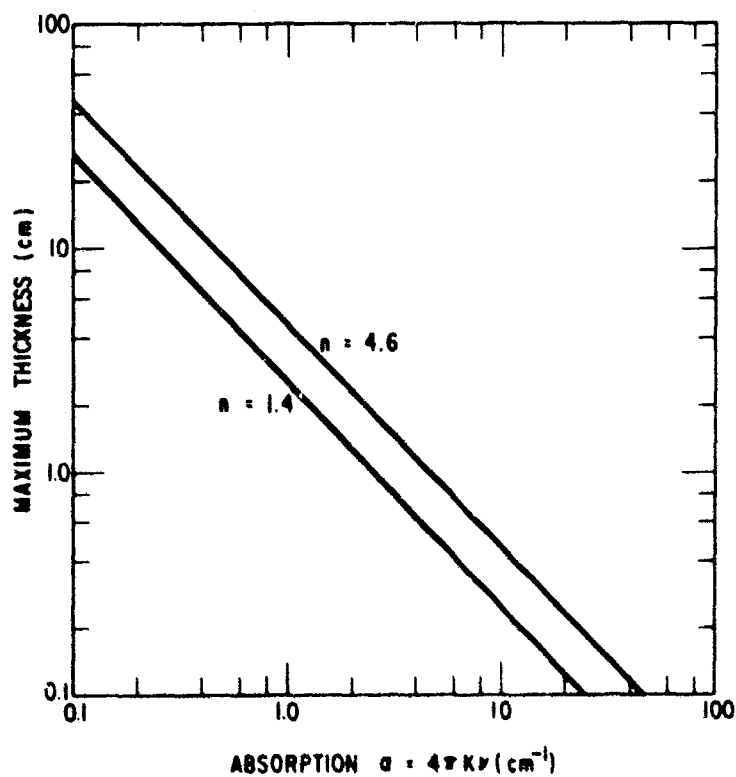


Fig. 40. Maximum sample thickness usable with present techniques for channel spectrum determination of refractive index in the FIR, for values of the real index n and absorption coefficient $\alpha = 4\pi k v$.

Since the order number, m , must be an integer there is no difficulty determining it exactly, provided that the accuracy is sufficient to distinguish between adjacent integers. Since in this wavelength region m is never larger than a hundred or so, accuracy is easily achieved. A simple procedure for determination of m is the following: Two values of ν_{\max} are determined from the spectrum for $m = m_1$ and $m = m_1 + p$. Substituting twice in Eq. (36) and subtracting, we have $2nh \cos \beta(\nu_{1 \max} - \nu_{2 \max}) = p$, from which an average n can be found. Inserting this value in one of the above equations then leads to a value of m . This technique will be adequate only as long as n is relatively constant, but when it is not, there will be strong absorptions and, as shown above, the method becomes unsatisfactory.

The determination of frequency furnishes an ultimate limit to the final precision. Measurements with our interferometer on pure rotational spectra indicate a limiting instrumental wavenumber accuracy of about 0.003 cm^{-1} , or, for 60 cm^{-1} radiation, about 5 parts in 10^5 .

To achieve this precision requires, however, locating the peaks in the spectrum with a similar precision. The precision with which the experimental peaks can be located is in turn limited by the inherent sharpness of the peaks, governed by how many terms in the series of Eq. (31) contribute significantly to the spectrum. The rate at which the terms in this series die off is in turn controlled by the index of the material. The precision is also limited by changes in the base line, which may make the lines appear to shift, and by noise. Figure 41, the channel spectrum of fused quartz, shows

two problems: First, if there is any change in absorption there will be a changing base line; second, the channel spectrum we are interested in uses only a small part of the dynamic range of the instrument. Both of these problems may be significantly decreased by means of the facilities in the Aerospace interferometer for double-beam difference

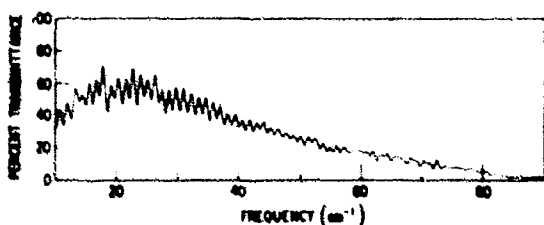


Fig. 41. Transmittance of 2.14 mm thick fused quartz $T(\nu)$ showing both channels and transmittance change caused by changing absorption.

interferometry. We can, while obtaining the interferogram, subtract the interferogram of a similar sample, different only in that it is wedged and therefore does not exhibit a channel spectrum. The resulting interferogram and its Fourier transform, the spectrum, appear in the upper part of Fig. 42.

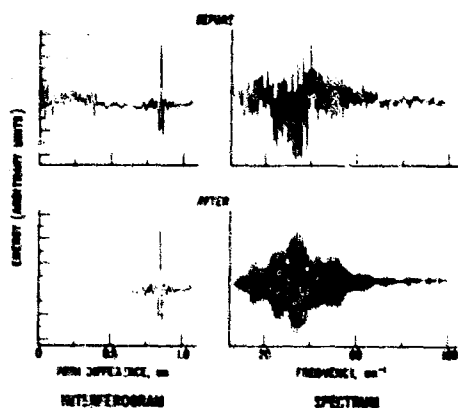


Fig. 42. Difference interferogram and spectrum for fused quartz, without editing (upper) and with editing (lower).

The changing base line has indeed been removed, but apparently at the expense of adding a good deal of noise. However, because of the localized nature of the information needed for the channel spectrum in the interferogram signature, as discussed above, it is possible to artificially remove much of the noise from the interferogram before it is transformed and still not harm the information content of the spectrum as far as determining refractive indices is concerned. The results of this are shown in the lower part of Fig. 42.

With all these procedures for improving

the measurement of the individual maxima, it is possible to decrease the scatter in points on the index curve by as much as a factor of 4 or 5 in the case of an absorbing material of low index such as fused quartz.

If the refractive indices are to be determined with an accuracy limited only by the frequency measurement, the error in the thickness value must not be limiting. For a typical sample thickness of 3 mm, this means a thickness determination to within a fraction of a fringe of visible light. The flatness and parallelism of the faces must be held within similar tolerances. Sample preparation to these tolerances has been carried out in our optical shop. The measurements of thickness to within $\pm 0.2 \mu$ were made by a commercial metrology laboratory. If measurements to this precision are to be meaningful,

¹²Metrotronics Inc., Burbank, Calif.

the material must be homogeneous to a similar extent. Since independent methods of analyzing the homogeneity are difficult, we have started with high purity material.¹³

Within the sample all light rays should see the same thickness of material. This effective thickness depends however on the angle with which the light is incident on the sample, the rays at large angles seeing an apparently foreshortened thickness as indicated by the cosine β in Eq. (34). Ideally then the measurements should be made in parallel light, but since this is not possible with the Aerospace instrument, the observed $T(v)$ is a sum over the possible angles weighted according to the solid angle, and is, except for a constant multiplier,

$$T(v) = T(v) \left[1 + \sum_{l=1}^{\infty} \frac{p_e}{(\cos \beta_m - 1)} \int_{\beta} \sin \beta \cos e\theta(\beta) d\beta \right]$$

where β_m is the maximum internal angle. Carrying out the integration,

$$\int_{\beta} \sin \beta \cos e\theta(\beta) d\beta = \left[\cos l 4\pi n h \left(\frac{\cos \beta_m + 1}{2} \right) \right] \frac{\sin y}{y}$$

where $y = 2\pi n h v (\cos \beta_m - 1)$.

Since the position of the channels is determined by the first term in the summation, the $\sin(y)/y$ term in the above equation with $m = 1$ is the one that attracts our attention. In our instrument, with its cutoff frequency of 125 cm^{-1} the maximum value y can have is $250 \text{ shn}(\cos \beta_m - 1)$. If we wish to have $y < \pi$, meaning our channel amplitude never goes through zero, then

¹³ Germanium and silicon came from Exotic Materials, Costa Mesa, Calif. Fused quartz was Infrasil grade low H_2O quartz.

$hn < [250(\cos \beta_m - 1)]^{-1}$. For an external half angle of 7.5 deg, this leads to a maximum thickness for samples of silicon and germanium, 1.1 and 1.8 cm, respectively. If this criterion is met, the additional effects introduced by the convergence of the beam on the amplitude of the modulation is less pronounced than the change in source intensity with energy. The only correction needed then is to replace the thickness h with $[h(1 + \cos \beta_m)]/2$. A sufficiently accurate determination of n to correct for beam convergence can usually be obtained from the positions of the signatures in the interferogram.

For materials sufficiently transparent for this method to be successful, the imaginary part of the dielectric constant k , which gives rise to both absorption and the phase factor δ , must be small. An estimate of sufficient precision can therefore be made by means of Eq. (32) from a spectrum of the average transmittance $\tau(v)$, using preliminary channel measurements to obtain a value of n . The average transmittance spectrum is also easily obtained from a single-beam interferogram by using only that portion of the interferogram around $x = 0$ and then dividing this spectrum by a spectrum obtained under similar conditions,

but without the sample in the beam. For the materials reported on here, the phase factor was small enough to ignore in comparison to the uncertainty in locating the channel spectrum peaks.

Figure 43 shows the results of the analysis as described when applied to the fused quartz spectrum in Figs. 41 and 42. The error bars on the refractive index data indicate the statistical scatter between nearby points and are smaller near the middle of the spectral region of interest, since this is the region where our

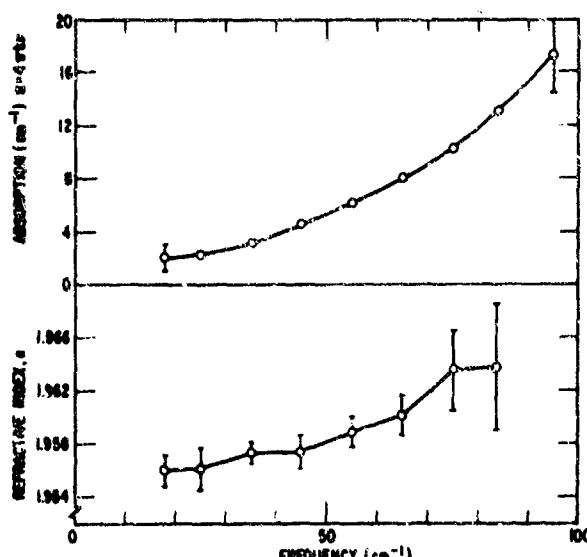


Fig. 43. Absorption coefficient $\alpha = 4\pi k v$, and real refractive index for fused quartz.

instrument has the best S/N. The absorption curve was calculated, by means of Eq. (32), from an average transmittance spectrum. The error bars on the absorption curve indicate the uncertainty of each point on the curve. This uncertainty arises almost entirely from the uncertainty in the transmittance measurements.

Because silicon has a higher index and lower absorption, more internal reflections contribute to the spectrum, as may be seen from the presence of 3 signatures in Fig. 44. Figure 45 shows the refractive index and absorption

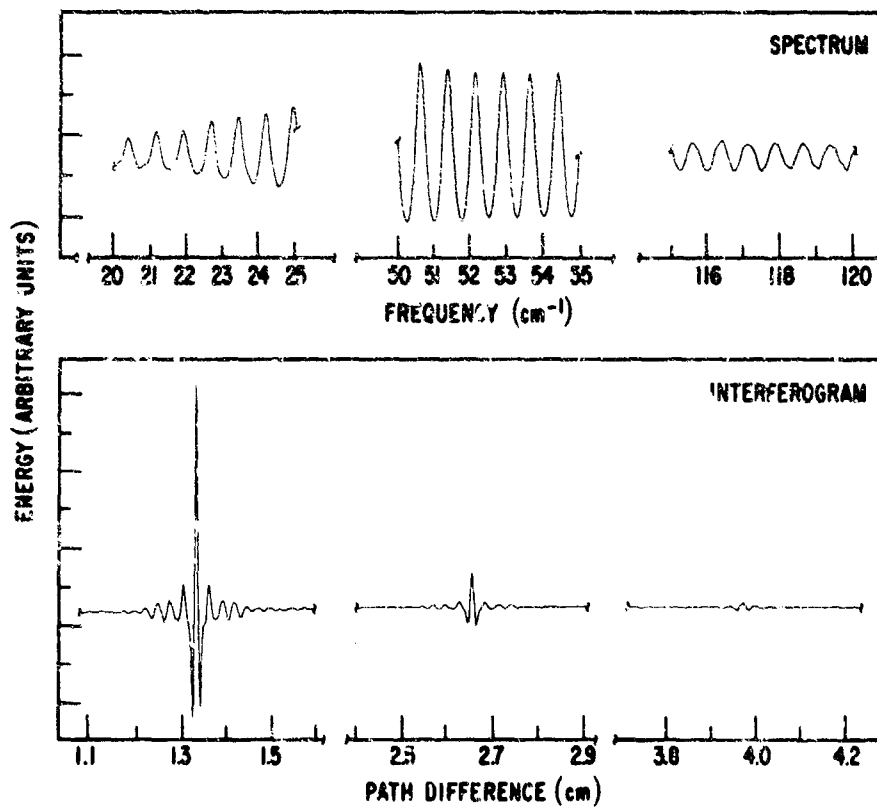


Fig. 44. Region of interferogram and spectrum for 0.194 cm thick silicon sample. Because of the high refractive index and low absorption, three signatures are visible, indicating that light undergoing up to six internal reflections is contributing significantly to the spectrum.

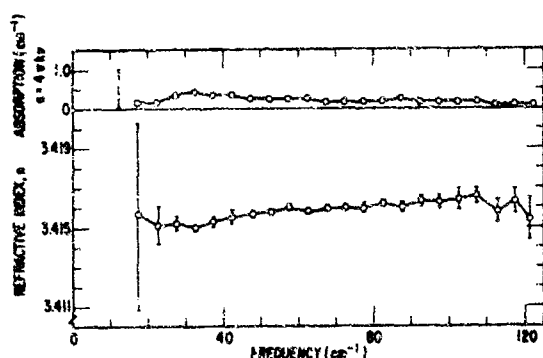


Fig. 45. Absorption coefficient and real refractive index for silicon.

constant in the FIR for silicon. The error bars have the same significance as those used on the fused quartz data. The higher number of internal reflections making significant contributions to the spectrum makes the peaks in the spectrum sharper, leading to lower scatter in the index data points. The transmission of one sample of silicon has been determined independently with a commercial grating spectrometer (Perkin-Elmer 301) over a wide spectral

range. These results are presented in Fig. 46, together with the measured transmittance with the interferometer in the region where the instruments

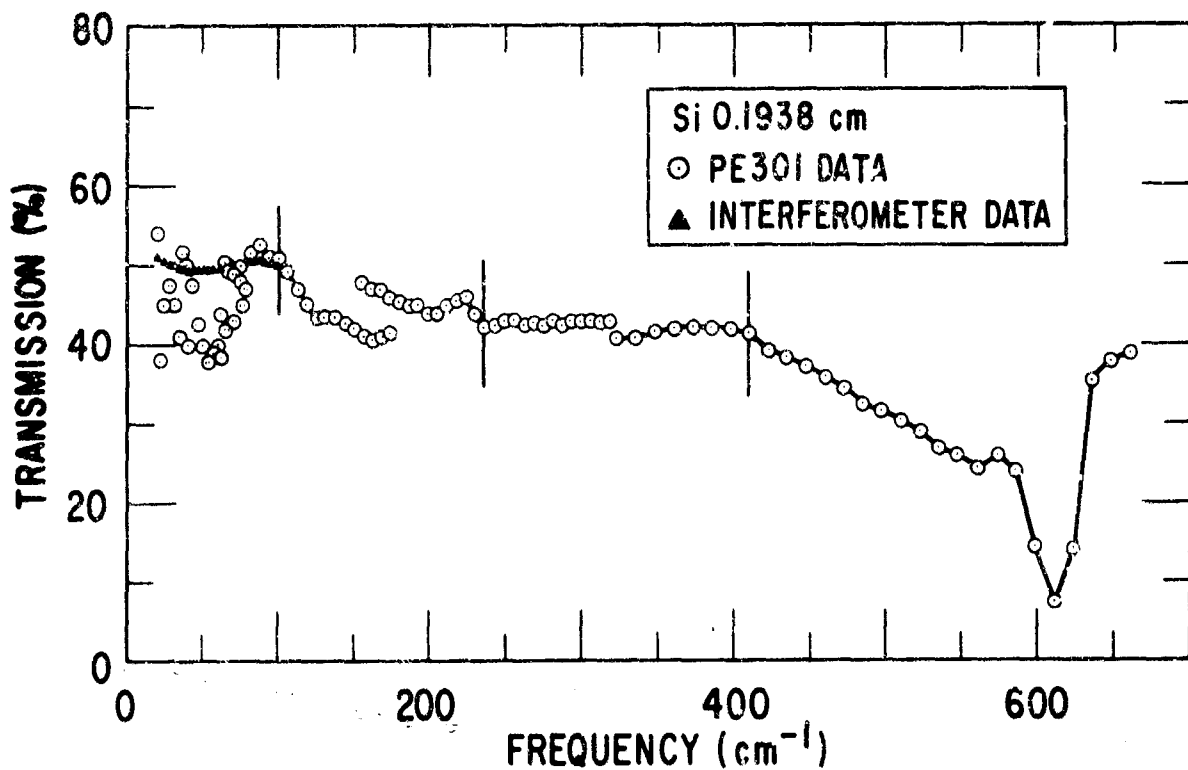


Fig. 46. Mean transmittance $\tau(\nu)$ of silicon.

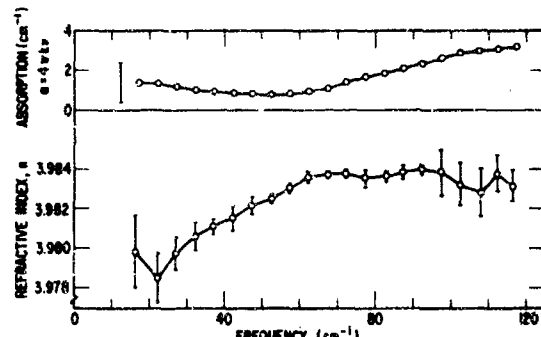


Fig. 47. Absorption coefficient and real refractive index for germanium.

for silicon might be expected. Germanium, however, exhibits more dispersion and more absorption. This may be caused by impurities in the sample but, we think we are observing the low-frequency side of the band at 100 cm^{-1} reported by Aronson and McLinden (Ref. 73).

overlap. From these measurements, estimates of the uncertainty in transmittance have been made.

Figure 47 shows the refractive index and absorption constant for germanium in the FIR. Figure 48 is a plot of transmittance, again taken over a wide range with the Perkin-Elmer 301, for comparison. Because of the chemical similarities between silicon and germanium, a spectrum similar to Fig. 44

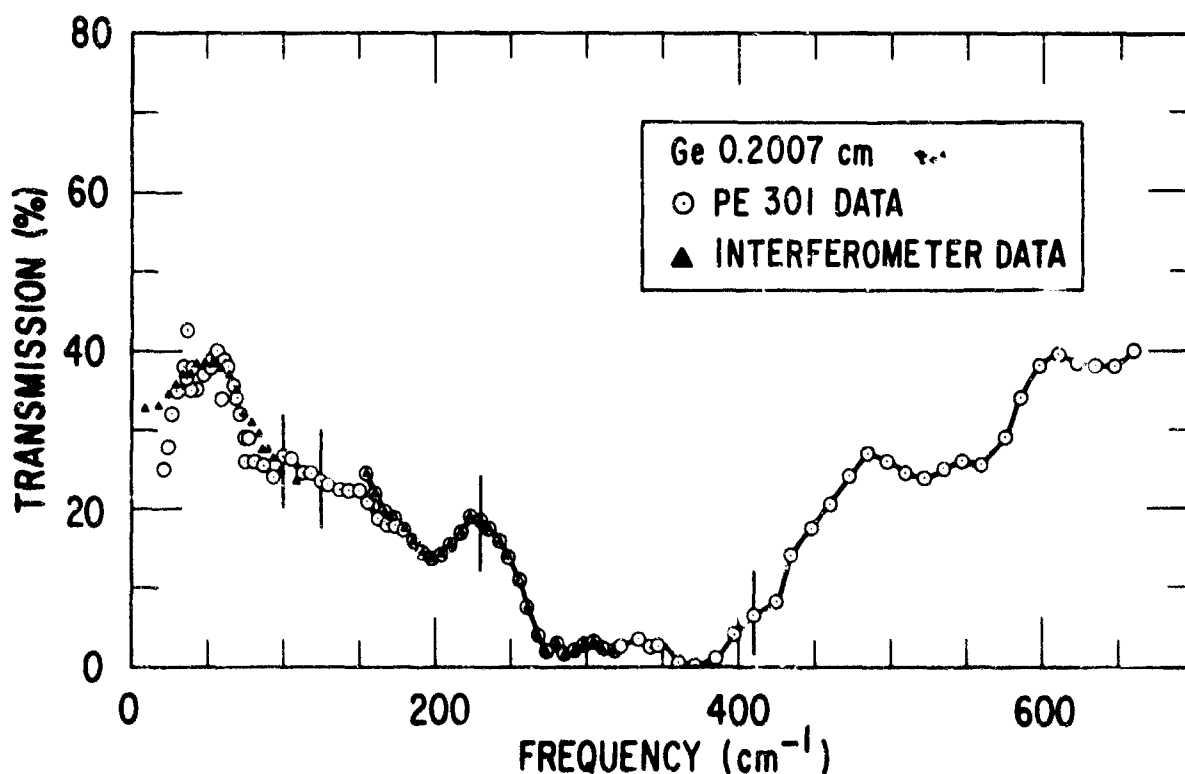


Fig. 48. Mean transmittance for germanium.

We have presented a method for determining the refractive index of materials from channel spectrum measurements. The equations used to obtain values make no assumptions except that of nearly normal incidence, so the polarization of the radiation is unimportant. This method is particularly well suited for interferometric measurement techniques since, as is shown, the spectrum may be written as a Fourier cosine series. Since the interferometer gives us the cosine transform of the spectrum, the approximations which are justifiable in treating the data are easily seen.

The method is good for materials which are not strongly absorbing in this spectral region. Limiting sample thicknesses for varying combinations of real index and absorption have been estimated.

These methods have been applied to a number of materials, with data presented for three, to show the application of the technique. It should be noted that the values are close to those measured in the radio frequency part of the spectrum and may differ widely from values in the visible region, as the fused quartz shows.

C. INDEX OF REFRACTION OF GASES

The results just described have encouraged us to try to apply the same principles to the measurement of the indices of refraction of gases in the FIR. The high-pressure absorption cell can be modified into an "interference cell." The faces against which the cell windows are mounted have been ground flat (~3 fringes of HG 5460 Å) and parallel (~8 arc sec). The windows are plano concave lenses of crystalline quartz. The focal lengths of the lenses are chosen such that the entering beam is made parallel inside the cell and then restored to its original divergence on leaving the cell. The interior surfaces of the windows are plain and provide the reflective surfaces for interference. In the FIR the reflectivity of a single surface of quartz is ~13% (in this respect germanium would be a better window material). Only preliminary tests of the cell as an interferometer have been completed. The first channel signature (at $x \approx 13$ -cm optical path difference) has been observed. The observed S/N for the signature is not as large as hoped for, and part of the reason for this is that the source is extended in nature. This results in difficulty in locating the focus in the sample chamber and subsequent

placement of the interference cell. A short arc Hg lamp is presently being tested (for reasons in addition to its more point-like feature) and evaluated for use as a source in the FIR.

D. NARROW BANDPASS FILTERS

Fabry-Perot etalons consisting of two parallel wire meshes have been used by earlier investigators (Refs. 74-77) as efficient narrow band filters for the FIR and microwave regions (wavelengths greater than about 50 μ). These filters have been further developed in this laboratory, the fabrication procedures and the performance obtained being the subject here. This work has been greatly facilitated by the availability of the Aerospace Corporation lamellar grating interferometer, which has a sensitivity and spectral resolution unavailable to the earlier workers. This permitted much better evaluation of the improvements in the filter design.

The spectrum transmitted by such a filter is described in texts on physical optics. The power transmissivity T is given by

$$T = \frac{t^2}{[(1 - r)^2 + 4r \sin^2 \delta/s]} \quad (37)$$

where t and r are the power transmissivity and reflectivity, respectively, of the individual meshes, and δ is the phase shift of the radiation passing twice through the gap between the meshes, i. e.,

$$\delta = 2\pi \cdot 2vb\mu \cos \theta + 2\phi \quad (38)$$

where $v = 1/\lambda$ is the wavenumber of the radiation, b is the mesh separation, μ is the index of refraction of the assumed nonabsorbing material in the gap, θ is the angle of incidence, and ϕ is the phase shift caused by reflection at a mesh surface.

All the filters discussed will have an air (or vacuum) gap between the meshes and, hence, $\mu = 1$. If the meshes are made of a metal with high conductivity the losses are small, or, $t \approx i - r$; and thus

$$T = \frac{t^2}{t^2 + 4r \sin^2 \delta/2} = \frac{1}{1 + (4r/t^2) \sin^2 \delta/2} \quad (39)$$

It is evident from this equation that $T_{\max} = 1$ for $\delta = m 2\pi$, where m is an integer, i. e., there is a series of transmittance peaks equally spaced in wavenumber for $v = v_{\max}$, where

$$v_{\max} = \frac{m\pi - \phi}{2\pi b \cos \theta} \quad (40)$$

Also, for $\delta = (m + 1/2) 2\pi$, $T_{\min} = (1 - r/1 + r)^2$, therefore $T_{\min} \rightarrow 0$ as $r \rightarrow 1$. The conventional measure of the sharpness of the fringes is the finesse F , defined as the ratio of the separation between adjacent fringes to the width at half maximum (half width) of a given fringe. For r near 1 this is given very closely by

$$F = \frac{\pi(r)^{1/2}}{1 - r} = \frac{\pi(r)^{1/2}}{t} \quad (41)$$

and $F \rightarrow \infty$ as $r \rightarrow 1$. A large finesse, of course, indicates narrow fringes.

The above theory assumes an ideal filter, i. e., no resistive losses, perfectly flat and parallel meshes, and the angle of incidence θ is either zero or a constant. In order to achieve a finesse F for nearly normal incidence, the allowable variation in b is $\delta b \approx 1/2vF$, thus, for $F = 100$, $v \sim 100 \text{ cm}^{-1}$, $\delta b = 5 \times 10^{-5} \text{ cm}$, or approximately one visible light fringe. This result is surprising in view of the general impression that the construction tolerances for FIR components can be rather sloppy because of the

large wavelengths involved. Attempts have been made by other workers to construct tunable filters, with adjustable mesh spacing, but the performance has been mediocre because the mesh parallelism was not adequately maintained. Also, simple rugged filters have been constructed by cementing meshes onto the faces of a wafer of fused quartz. Again the performance has been mediocre, perhaps due to inhomogeneities or lack of flatness in the quartz, but more probably due to lack of perfect contact between the quartz and the mesh caused by inclusions of cement.

The available meshes¹⁴ are from 5 to 2000 mesh (rulings per inch), and are about 0.0002 in. \approx 5- μ thick. For the FIR region considered here ($v = 10$ to 100 cm^{-1}), 250- to 1000-mesh rulings are most suitable. These meshes are fragile and have no rigidity of their own and so must be carefully stretched over a supporting ring to remain flat, as shown in Fig. 49. The meshes are cemented as smoothly as possible onto the two temporary supports shown. No wrinkles, as seen by reflected light, can be permitted at this stage. These are then hung over the other members, as shown, the weight of the support rings stretching the meshes taut. The assembly is then clamped between the end pieces, the excess mesh trimmed off, and the joint sealed with epoxy cement.

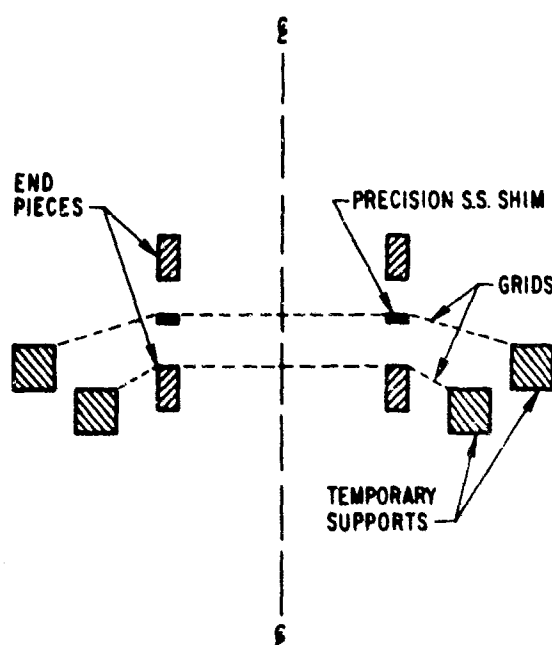


Fig. 49. Details of filter construction. The space is cut from precision stainless steel shim stock and the burrs carefully removed. The faces of the end pieces touching the grids are machined and lapped flat.

¹⁴ Available from Buckbee-Mears Corp., St. Paul, Minn.

Since the wire meshes must be very accurately flat and parallel, the most critical component is the stainless-steel shim space shown. Ours have been cut from precision shim stock, any burrs on the edge being carefully removed by lapping. The end pieces also are carefully machined and lapped. A completed filter with a 1-in. aperture is shown in Fig. 50.



Fig. 50. Photograph of a completed filter.

Calculations of the transmittance or reflectance of a metal mesh are difficult because of the complex two-dimensional geometry. The most successful approach involves the calculation of an equivalent transmission line and has been solved for the related problems of one-dimensional arrays of various shaped wires (Ref. 78-80) and the problem of circular openings in a metal sheet (Ref. 81). We find however a very satisfactory analysis of filter performance can be based on the empirically determined values of power reflectance r and power transmittance t for a single mesh. Scaling the distance d between mesh opening by the wavenumber ν allows us to plot results in terms of the dimensionless variable νd , making it possible to compare data taken on different meshes in different frequency ranges. Figure 51 is a plot of the transmission of four different mesh materials as a function of this reduced variable νd . The transmission curves for this region are nearly straight lines on a loglog plot, indicating a simple power law relation. The curves for two of the materials coincide as anticipated. The 250-mesh material, however, exhibits a higher transmittance, as might have been expected, since each cell in this mesh has about 17% more open area than the cells in the other meshes. The nickel mesh exhibits a higher transmission, perhaps due to its higher resistivity.

For νd greater than that shown in the figure, the measured transmittance first rises to a maximum of about 90% at $\nu d \approx 0.85$ and then decreases and oscillates for greater νd . For $\nu d > 1$, a mesh begins to act

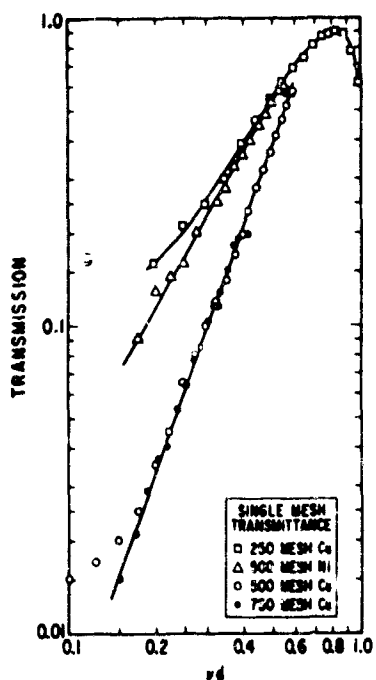


Fig. 51. Transmission of a single wire mesh as a function of reduced frequency, νd , where d is the spacing between openings; □ 250-mesh ($d = 102\mu$) copper (Buckbee-Meers ruling no. 25027); △ 500-mesh ($d = 204\mu$) nickel (ruling no. unknown); ○ 500-mesh ($d = 204\mu$) copper (ruling no. 509); ● 750-mesh ($d = 306\mu$) copper (ruling no. 761).

as a two-dimensional diffraction grating; hence, varying amounts of transmitted power are diffracted out of the acceptance angle of the measuring instrument, making details of the measured transmittance dependent on the particular experimental geometry used for the measurement. In view of the variability of mesh fabrication and the difficulties of measuring absolute transmissions in this spectral region, we feel the present results are in satisfactory agreement with those of others (Refs. 9, 74-76, 82). Indeed the data in Fig. 8 of Russell and Bell (Refs. 9, 83) superimpose on our 500- and 750-mesh data for values of νd from 0.25 to 0.75.

The Aerospace interferometer cannot measure reflectance at normal incidence, and hence we cannot show that $r = 1-t$, thus demonstrating the absorption in the mesh to be small. However the data of Mitsuishi, et al. (Ref. 75) indicate that losses are indeed small, at least for $\nu d < 0.85$. Also the performance of the filters discussed in Section V could not have been achieved had there been large losses in the meshes.

The choice of mesh material for a particular filter application depends on the wavenumber and finesse specified. For example, from Eq. (40) if $F = 100$ is required, $r \approx 97\%$ or $t \approx 3\%$. From Fig. 51, this gives $\nu_d = 0.19$ for the 500- or 750-mesh grids, and $\nu \approx 54 \text{ cm}^{-1}$ or 36 cm^{-1} , respectively. Note that the above finesse assumes an ideal filter and makes no allowance for fabrication imperfections.

Filters have been successfully made using a number of meshes and shim spacers. A measured spectral response curve for one of the better samples (750 mesh, 0.0807-cm space) is given in Fig. 52. This is the actual energy

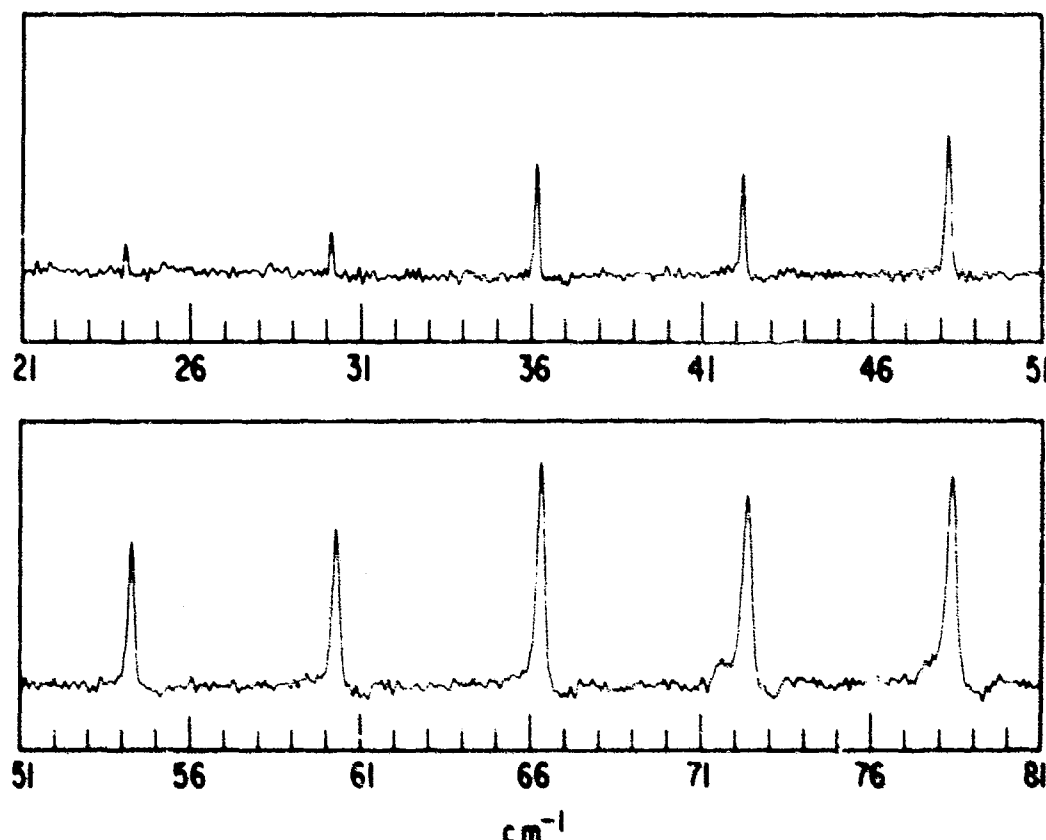


Fig. 52. Energy throughput of a wire mesh filter consisting of two 750-mesh screens separated by a 0.0805 cm spacer.

throughput, and it is multiplied by the spectrum of the source and the transmittance of the interferometer. Transmission peaks appear approximately every 6 cm^{-1} , the three at 6, 12, and 18 cm^{-1} being missing because of the low energy available in this interval. The widths of the peaks increase with ν as expected from the mesh transmittance given in Fig. 51. From the noise level at the base of the peaks, it is evident that peak transmittance values and off-peak rejection can be determined at best to within about 5%. This is poorer than the measurements on single grids because of the small amount of energy transmitted with a narrow transmittance peak.

Wavenumber determinations are much more accurate than intensity measurements as they are calculated directly from the grating displacement. Transmittance peaks can be read to about 0.003 cm^{-1} and half-widths to about 0.005 cm^{-1} .

The half-width thus determined is not the true half-width of the filter, but it is broadened by the finite resolution of the interferometer and by the convergence of the measuring beam of radiation. The resolution of the interferometer is limited by the maximum displacement permitted the lamellar grating. However, before this limit is reached the interferogram signal falls into the noise, and hence, in practice the resolution is actually limited by the S/N. In order that there be a usable signal it is necessary that a convergent beam be transmitted through the filter, θ varying from 0 to θ_{\max} and ν varying from $m\pi - \phi/2\pi b$ to $m\pi - \phi/2\pi b \cos \phi$, according to Eq. (40). For a beam of half-angle θ_{\max} it can be shown that this broadens the peaks by approximately $\delta\nu_g = \theta_{\max}^2 \nu / 2$.

In Fig. 52 finesse calculated from the measured half-widths is plotted against ν for three 750-mesh filters. As expected, F decreases with ν . The largest values (100) were obtained in a filter with a thin spacer and correspondingly wide, more easily measured peaks. The two curves for the filters with the wide space were obtained with $\theta_{\max} = 8 \text{ deg}$ and $\theta_{\max} = 4 \text{ deg}$ and clearly show the broadening due to beam convergence. The finesse

values reported here have no corrections applied, and yet they are about three times larger than values reported by earlier workers (Refs. 74, 76) for which a spectrometer slit-width correction was applied.

The magnitude of the corrections which could be applied here is indicated by Fig. 54 for the 750-mesh, 0.0807-cm shim filter. The upper curve

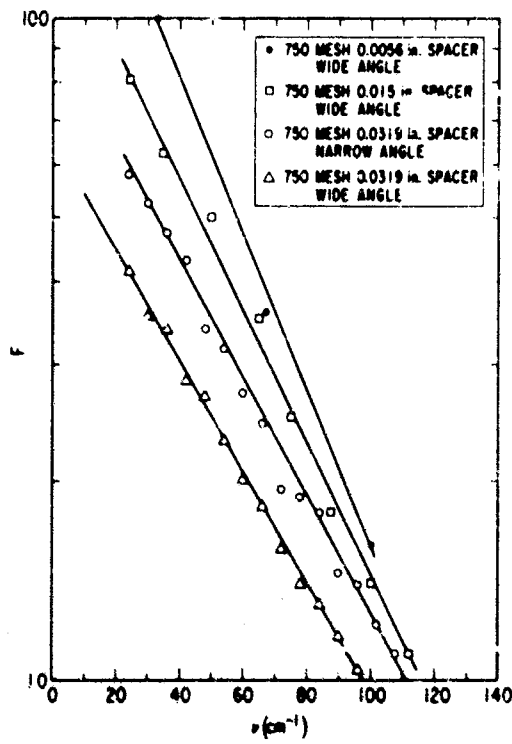


Fig. 53. Measured finesse for 750-mesh filters of different spacing.

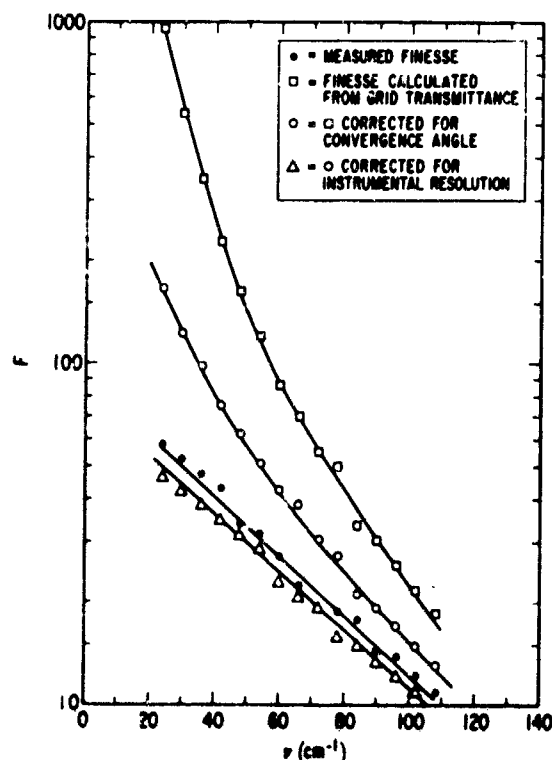


Fig. 54. Reduction in finesse for 750-mesh, 0.081-cm spacing filter due to limitations of measuring technique.

is the finesse calculated from the measured mesh transmittance (Fig. 51). It assumes a perfect filter fabrication and ideal measuring instrumentation. Introducing the 4 deg beam angle convergence lowers the finesse to the second curve. Including, in addition, the finite resolution of the particular

interferometer measurement lowers the finesse to the bottom curve. It is seen that this curve is in close agreement with the actual measured finesse. Because the corrections are an order of magnitude larger than the ideal half-width, the true finesse cannot be calculated with any precision. We can conclude however that it is significantly larger than the value of 58 measured at 24 cm^{-1} . The ideal finesse of 1000 shown in the figure is unreasonably large, as it would require meshes flat and parallel to within about 500 \AA .

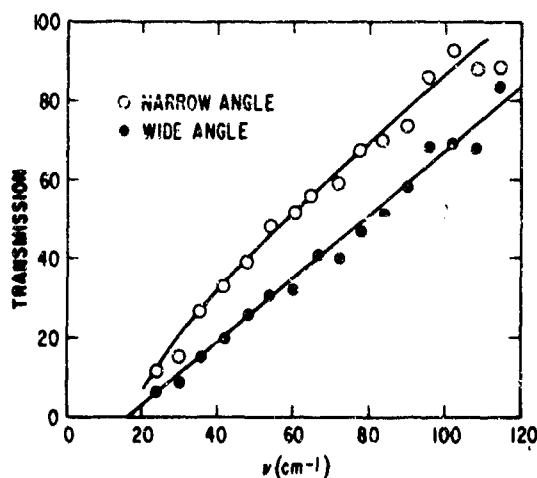
Further evidence that the measured finesse is too low is given by Fig. 55, which is a graph of the measured transmittance at the peaks for

the same 750-mesh, 0.0805-cm space filter, measured again with 4 and 8 deg beam angles. Increasing the beam angle and hence widening the peak decreases the measured transmittance as would be expected from an unresolved peak. The peak transmittance at this wavenumber for the 750-mesh, 0.0142-cm spacer filter is about 40%, or about three times as large. Since the meshes and wavenumbers are identical, the transmittance should not be greatly different. This would indicate a true finesse of at least 180.

The off-band rejection cannot be adequately measured with our instrument--or any existing FIR instrumentation. From the data presented, however,

Fig. 55. Transmission as a function of frequency for a 750-mesh, 0.081-cm spacing filter for two beam convergence angles.

we have some confidence that an adequate mathematical description of the filter can be made using Eq. (37) and the measured transmittance of the single meshes (Fig. 51). Filter imperfections will broaden the peaks, but they should have little effect on the off-band rejection. Resistive losses however will degrade the rejection. The minimum transmittance

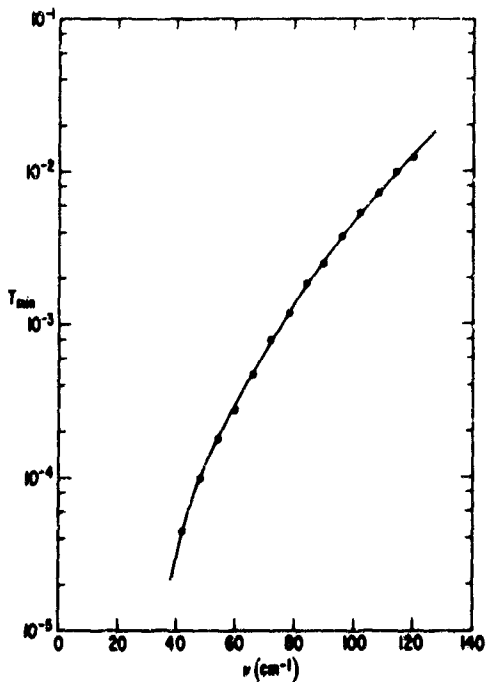


halfway between peaks calculated from this equation is shown in Fig. 56. The

low frequency peaks (Fig. 53) do indeed intersect sharply with the noise base line, so these results are not unreasonable. The high rejection levels shown in Fig. 56 are of course to some extent meaningless in a room temperature environment, since the blackbody radiation from the filter itself, or reflected from other portions of the instrument by the filter, can easily be much larger than the off-band energy transmitted by such a filter.

We feel that these interference filters can now be made to order with finesse, peak transmittance, and off-band rejection better than can be measured with any existing instrumentation. In particular applications, additional filtering will be needed to eliminate the unwanted higher harmonics. This filtering will have to be tailored for each case. A study of suitable materials and techniques is in progress.

Fig. 56. Calculated transmission halfway between peaks of a 750-mesh filter.



V. NOISE, EXPERIMENTAL ERRORS, AND PROBLEMS

A. ORIGIN ERROR (x = 0 point)

The origin error has been discussed by Connes (Ref. 6) and is briefly reviewed here. We will consider its effect on a Lorentz line.

$$\text{Input Spectrum} \quad I(\nu) = \frac{A\epsilon}{(\nu - \nu_0)^2 + \epsilon^2}$$

$$\text{Interferogram Function} \quad F(x) = \pi A e^{-2\pi x \epsilon} \cos 2\pi x \nu_0$$

We now assume an error has been made in locating the first point of the interferogram at $x = 0$; therefore,

$$x_{\text{measured}} = x_{\text{(true)}} - \beta$$

where β is the error. Thus,

$$F(x) = \pi A e^{-2\pi(x-\beta)\epsilon} \cos 2\pi(x - \beta)\nu_0$$

$$= \pi A e^{2\pi\beta\epsilon} e^{-2\pi x \epsilon} \cos 2\pi(x - \beta)\nu_0$$

The output spectrum is then

$$I_\beta(\nu) = e^{2\pi\beta\epsilon} \left[\frac{A\epsilon}{(\nu - \nu_0)^2 + \epsilon^2} \cos 2\pi\beta\nu_0 - \left(\frac{\nu - \nu_0}{\epsilon} \right) \sin 2\pi\beta\nu_0 \right] \quad (42)$$

The exponential factor $e^{2\pi\beta\epsilon}$ is usually very close to one in that usually $\beta\epsilon \ll 1$; therefore, we neglect it. Equation (42) is shown in Fig. 57 for the cases $\beta\nu_0 = 0$ (no error), $\beta\nu_0 = 1/8$, and $\beta\nu_0 = 1/4$. As seen in this

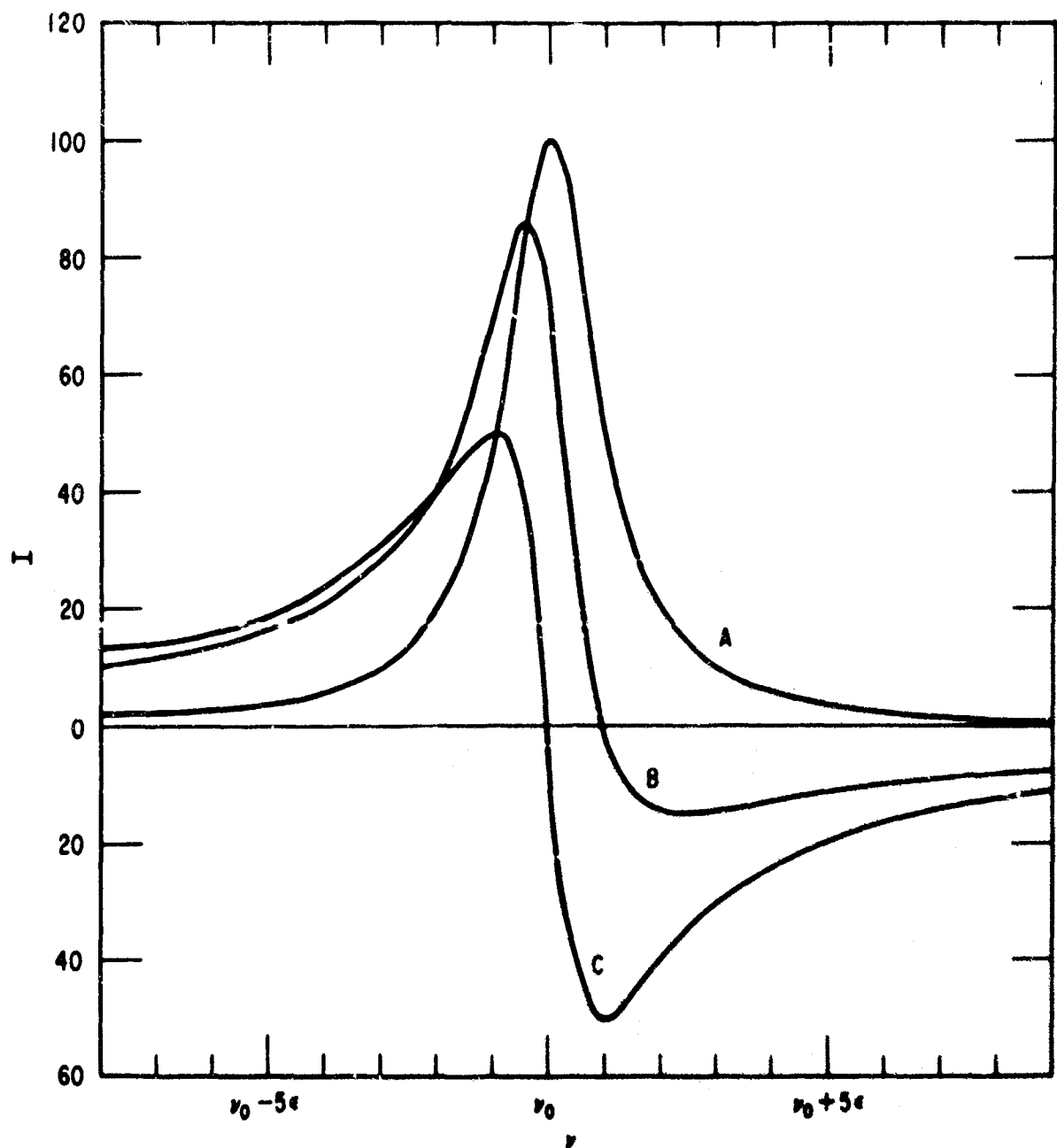


Fig. 57. Appearance of a Lorentz line when an error has been made in the location of the origin; curve A, $\beta\nu_0 \approx 0$, curve B, $\beta\nu_0 = 1/8$, and curve C, $\beta\nu_0 = 1/4$.

figure, the line shape can be severely distorted and significant apparent line shifts are possible. The amount of distortion depends on β and ν_0 . When an error of this type is made in the interferogram, its effect in the spectrum is usually quite striking. As an example, assume $\beta = 50\mu$ (a large error) in an interferogram made up of lines spread out in the wavenumber region 0 to 100 cm^{-1} . In the region $\sim 0 \text{ cm}^{-1}$, the lines would appear almost as they should; near $\nu \approx 50 \text{ cm}^{-1}$, where $\beta\nu_0 \sim 1/4$, the lines would have the most asymmetric appearance, somewhat like their first derivative shape; near $\nu \approx 100 \text{ cm}^{-1}$, the lines would again have near their true shape but would be upside down. It is obvious that good spectral data will be obtained only if $\beta\nu_0 \ll 1/4$.

When β is sufficiently small so that $2\pi\beta\nu_0$ is small enough for the small angle approximation to hold in Eq. (42), then the shifts and distortion in the line shape can be easily calculated. These are summarized in Table 12.

Table 12. Distortions Caused by Mislocation of Origin ($x = 0$)

Quantity	$\beta = 0$	$\beta \neq 0$ (small angle approx.)
$I(\nu)$	$\frac{A\epsilon}{(\nu - \nu_0)^2 + \epsilon^2}$	$\frac{A\epsilon}{(\nu - \nu_0)^2 + \epsilon^2} \left(1 - \frac{\nu - \nu_0}{\epsilon} q\right)$
$I(\nu)_{\max}$ at	ν_0	$\circ - \frac{\epsilon q}{2}$
$I(\nu)_{\max}$	$\frac{A}{\epsilon}$	$\frac{A}{\epsilon} \left(1 - \frac{3q^2}{4}\right)$
Half-width	2ϵ	$2\epsilon \left(1 + \frac{5q^2}{4}\right)$
$q = 2\pi\beta\nu_0$		

B. PERIODIC ERROR

Another possible error in the measurement of x is a periodic error, a type of error expected if a screw type mechanism (Ref. 6) (and, as we shall show, a linear inductosyn system) is used. Let us assume a monochromatic line input.

Input Spectrum

$$I(v) = \delta(v_0)$$

Then

$$F(x) = \cos 2\pi x v_0$$

Now let us assume a periodic error of period L_e , and amplitude B ; thus,

$$x_{\text{measured}} = x_{(\text{true})} + B \sin \left[\frac{2\pi x_{(\text{true})}}{L_e} + \phi \right]$$

where ϕ is a phase factor. The measured interferogram function will then be

$$F_B(x) = \cos \left\{ 2\pi \left[x + B \sin \left(\frac{2\pi x}{L_e} + \phi \right) \right] v_0 \right\}$$

and now, calling $v_e = L_e^{-1}$

$$\begin{aligned} F_B(x) &= \cos [2\pi x v_0 + 2\pi B v_0 \sin(2\pi x v_e + \phi)] \\ &= \cos(2\pi x v_0) \cos(2\pi B v_0 \sin(2\pi x v_e + \phi)) \\ &\quad - \sin(2\pi x v_0) \sin(2\pi B v_0 \sin(2\pi x v_e + \phi)) \end{aligned}$$

We now assume $2\pi B\nu_o$ is small enough that the small angle approximation is valid; therefore,

$$\begin{aligned} F_B(x) &\approx \cos(2\pi x\nu_o) - 2\pi B\nu_o \sin(2\pi x\nu_o) \sin(2\pi x\nu_e + \phi) \\ &= \cos(2\pi x\nu_o) - \pi B\nu_o \cos[2\pi x(\nu_o - \nu_e) + \phi] + \pi B\nu_o \cos[2\pi x(\nu_o + \nu_e) + \phi] \end{aligned}$$

In the spectrum, the first term gives the line at ν_o ; the second and third terms yield ghosts at $\nu = \nu_o \pm \nu_e$, where shape will in general be distorted by the phase factor ϕ in much the same way as discussed in Section V-A. It is obvious that if $2\pi B\nu_o$ is not small enough that the small angle approximation is valid, so that higher order terms should be carried in the expansion, then these higher order terms would contribute ghosts at $\nu = \nu_o \pm n\nu_e$. We can estimate the first relative ghost intensity:

$$\frac{\text{ghost intensity}}{\text{line intensity}} \approx \pi B\nu_o \quad \text{for } \phi = 0$$

We have examined our linear inductosyn scale for this type of error. The following technique was employed. The signature of a diatomic molecule should be evenly spaced in optical path difference. The positions of the maximums of the first eight signatures of HBr were measured (the isotopic splitting is negligible in this molecule for signatures in the neighborhood of the origin). These eight measurements were then fitted to an equation of the form: $x(\text{signature maximum}) = an + b$, where n is the signature number and b is included to account for any origin error. The best values of a and b were determined, and the deviation calculated and plotted as a function of x . The results are shown in Fig. 58 with a sine curve of amplitude 1.5μ and period 2 mm fitted to best cover the points. The error bars represent the uncertainty, due to noise, in locating the signature maxima. There is little doubt that a periodic error exists. For $B \sim 1.5\mu$ and a period of ~ 2 mm, the ghost intensity at $\sim 50 \text{ cm}^{-1}$ line should appear with $\sim 2\%$ of the line intensity

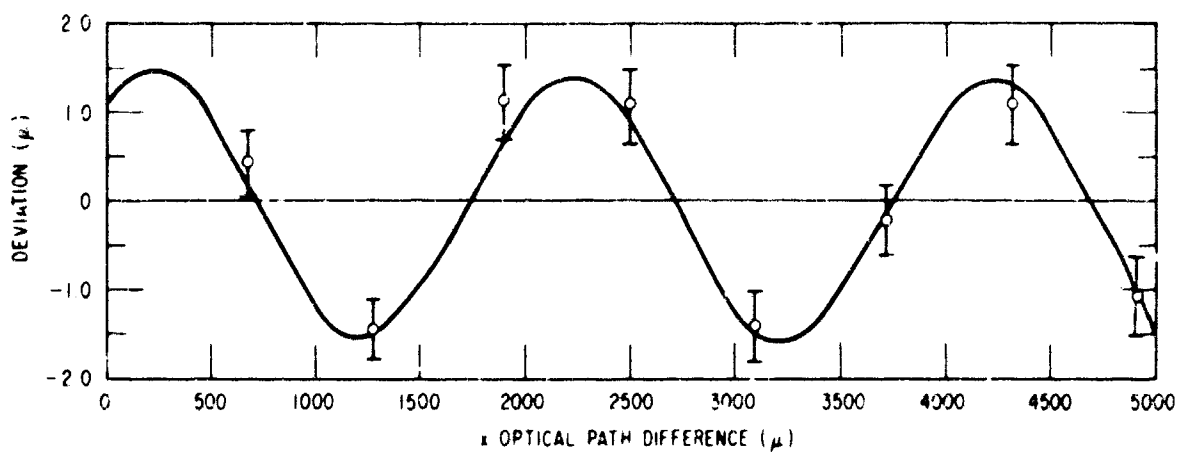


Fig. 58. Optical path difference error in a linear inductosyn scale. The superposed curve is a sine curve of amplitude 1.5 μ and period 2 mm.

at displacements of $\sim \pm 5 \text{ cm}^{-1}$ away from the line. The over-all noise level of most of our spectra would hide these ghosts; however, see Fig. 52. There are features at $\sim \pm 5 \text{ cm}^{-1}$ about each of the "lines" that appear to be ghosts.

The remedy for this error is of course a more accurate measurement of x , the optical path difference. The possibility of using a single mode laser is being examined.

C. CHOICE OF Δx

As mentioned previously, the optical path difference increment Δx is fixed by sampling theory; i. e., $\Delta x \leq (2v_c)^{-\frac{1}{2}}$, where v_c is the cutoff wavenumber of the spectrum. Three points are discussed: (1) determination of v_c , (2) effect of choosing Δx too large, and (3) effect of choosing Δx smaller than need be.

We determine Δx (or v_c) in the following manner. An interferogram of the source is obtained with a relatively small Δx , corresponding to a large v_c . This interferogram is then transformed and the spectrum of the lamp as modified by the filtering is obtained. Where the intensity goes to zero (within the noise level) is the true v_c , and thus the maximum Δx is determined. This is done whenever sources or filtering arrangements are changed.

When Δx is chosen too large, aliasing takes place. This is best understood in terms of the scanning function. The breadth of the scanning function is determined by L , the maximum optical path difference generated. The range over which the scanning function scans¹⁵ is determined by Δx . Actually, except as $\Delta x \rightarrow 0$, there is more than one scanning function. For a given Δx the first scanning function covers the spectral region $0 \rightarrow v_c$; the second, $2v_c \rightarrow v_c$; the third, $2v_c \rightarrow 3v_c$; etc. Thus when Δx is taken too large or there is intensity in the spectrum beyond $v_c + (2\Delta x)^{-1}$ one will alias the spectral information beyond v_c back into the region $< v_c$. To illustrate, suppose the true cutoff wavenumber of a spectrum is 125 cm^{-1} (for which $\Delta x = 1/250 \text{ cm}^{-1} = 40\mu$) but Δx is chosen to be 50μ (corresponding to a v_c of 100 cm^{-1}). Under these conditions the spectral data between $0 \rightarrow 100 \text{ cm}^{-1}$ will be displayed as they should be, but in addition the spectral data between $100 \rightarrow 125 \text{ cm}^{-1}$ will be folded over on top of the data between 100 cm^{-1} and 75 cm^{-1} . This is somewhat similar to the overlapping of orders in a grating spectrometer and is usually undesirable.

There is, however, one case where the multi-order scanning function is an advantage. Suppose there is no intensity in the regions corresponding to the 1st, 2nd, . . . , ($n - 1$)th order, but there is intensity in the n th and none beyond. Then Δx can be chosen as $[2(n + 1)v_c - 2nv_c]^{-1} = (2v_c)^{-1}$ instead of $\Delta x = [2(n + 1)v_c]^{-1}$, and for the same resolution fewer points need be measured. This has been exploited by the Connes (Refs. 6, 7) in their near-IR studies.

Making Δx smaller than need be is equivalent to making v_c larger than need be, and obtaining the same resolution requires more points to be measured. In theory there is no disadvantage, but in practice it amounts to a waste of measuring time and computer time. This is expanded on in the discussion of noise in interferometry.

¹⁵ There is no scanning in the formal sense, but it is convenient to discuss it in this manner.

D. CHANNEL SPECTRA

One of the most annoying phenomenon encountered in FIR interferometry is channel spectra. In this frequency region ($10\text{-}125\text{ cm}^{-1}$), surfaces not plane parallel under the usual optical criteria (a fraction to a few wavelengths of visible light) may be plane parallel in the FIR and will produce channel spectra. The effect is quite easy to see in IR interferometry, and signature-type features will be easily detected in interferograms at $x = 2nd$ (Ref. 72), where n is the index of refraction of the plane parallel slab of material, and d is its thickness. Windows can be suitably wedged to prevent this phenomenon, and all the windows have been so treated in our interferometer. However, the thin pieces of black polyethylene used as filters cannot be wedged and are believed to contribute somewhat to the previously discussed residual unbalance at the origin. The channel signature will come close to $x = 0$ since $d \sim 100\mu$ and $n \approx 1.5$; of course, there is some cancellation because of double beaming.

More troublesome is the fused quartz envelope of the high-pressure Hg arc used as the source. It seems to have local areas of plane parallelism and, since the reference beam and sample beam do not originate from exactly the same region of the plasma and envelope, the effect is far from cancelled by double beaming. We have tried dimpling the lamp as suggested by Richards (Ref. 18), but this led to great difficulties in making an equivalent match between the two beams. We have therefore left our lamps undimpled. The result is a cosine variation of the source spectrum that is superimposed on the sample spectrum with a period of $\sim 1.3\text{ cm}^{-1}$ and whose amplitude decreases at higher wavenumbers. Fortunately these channels are quite wide, and their maxima and minima are easily determined; thus, they are not confused with the sharp lines observed in the high resolution spectra. However, as the width of the lines approaches the period of variation the error in the frequency determinations is greater. It is estimated that the amplitude of oscillation (in intensity) of this channel spectrum is four to eight times the noise level in the low wavenumber region of the spectra.

As mentioned, the channels are much stronger in the low wavenumber region and are almost nonexistent above 55 cm^{-1} . From this we infer that most of the energy in the low wavenumber end of the spectrum ($\gtrsim 55 \text{ cm}^{-1}$) comes from inside the lamp (i. e., the plasma) and most of the energy above 55 cm^{-1} comes from the hot quartz envelope.¹⁶

E. LONG TERM SOURCE FLUCTUATIONS - STEP FUNCTIONS

The medium-high pressure Hg arc lamp has been the most frequently used source for the far infrared. Although no comprehensive comparison of possible FIR sources has been made, it is rather firmly established that the medium-high pressure Hg arc is a brighter FIR source than a glowbar (Ref. 83), a He discharge (Ref. 84), or a high pressure Na lamp (Ref. 85).

It has been our experience that the stability of Hg arcs such as the G. E. AH3 and AI4 is the limiting factor (i. e., largest contributor to the noise) in our observed S/N (if the channel spectra are not considered noise). At first, it would seem that monitoring the source and using this to operate a feedback loop so as to compensate for these fluctuations would eliminate this difficulty. Aside from the negative resistance characteristics of these lamps such a scheme is not practical since the Hg arc is in reality two sources, the plasma, and the hot envelope of the lamp. Most, if not all, of the fluctuations are in the plasma. Their onset is quite rapid and may have quite a long duration (~15 minutes). We have seen, quite often, a step function type discontinuity in the interferogram. Conversely, the FIR energy output from the envelope should be quite steady, and, even if it did change, such a change would be expected to be slow and quite small (if power input is regulated to some degree). The arc fluctuations are caused by two inter-related effects: changes in the voltage-current characteristics and actual arc wandering over the electrodes. The phenomenon is very noticeable in

¹⁶At room temperature, fused quartz does show a cutoff in the $50-60 \text{ cm}^{-1}$ region; however, it is impossible to say what the spectral transmission properties are at the temperatures the envelope reaches when the lamp is on.

double-beam operation ($\sim 4\%$ of $F'(x)$ average). In this respect we have found that the AH3 lamps appear somewhat more stable than the AH4 lamps. We surmise that this is due to the capillary restrictions in the AH3 lamps not present in the AH4 lamps, and thus the actual physical wandering of the arc in the AH3 lamps is less than in the AH4 lamps.

We now consider what effect a step function in the interferogram has on the spectrum obtained by Fourier cosine transformation. Consider a step function of amplitude A starting at x_1 and ending at x_2 . The effect of the "box" in the spectrum is ascertained by Fourier cosine transforming the "box" from optical path difference space (x) into wavenumber space (v). Thus

$$I(v)_{\text{box}} = \int_0^{\infty} A(x_1, x_2) \cos 2\pi x v dx = A \int_{x_1}^{x_2} \cos 2\pi x v dx$$

which can be written

$$I(v)_{\text{box}} = [A(x_2 - x_1)] \cdot [\cos \pi v(x_2 + x_1)] \cdot [\operatorname{sinc} \pi v(x_2 - x_1)]$$

The first term, the amplitude, is proportional to A , which is the amplitude of the step function in optical path difference space and to $(x_2 - x_1)$, the duration of the step function in optical path difference space. The second term gives the rate of the variations in wavenumber space. If $(x_2 + x_1)$ is large, the fluctuations will be rapid and will appear to the observer as high-frequency noise. The last term is the envelope (in general) of this function, and it is seen that the largest fluctuations of $I(v)_{\text{box}}$ occur in the low wavenumber region.

It is possible to "edit" the interferogram by estimating A from the record, then subtracting it from the interferogram function from points x_1 to x_2 . This will eliminate the gross effects of the extraneous box, but in no way compensates for the fact that there has been a real spectral change of intensity (plasma change) or an apparent change (arc wander).

We are testing and evaluating some "short arc" dc operated Hg lamps in the hope that they will provide a solution to this problem.

F. STOP-AND-GO SCANNING AND TIME CONSTANTS

As described, digital computation is the most flexible and accurate means of performing the Fourier transforms required in interferometric spectroscopy. This requires that the continuous interferogram be sampled, meeting particular requirements of frequency and total number of samples as discussed in this report. The simplest scheme for taking those data is an on-the-fly technique in which the grating moves continuously. Data are taken during a time interval sufficiently short that the grating has not moved appreciably. If a high S/N were available in the interferometer output, this scheme would allow rapid data acquisition. However, because of the low S/N available in the signals being detected, obtaining adequate S/N in data taken by this method would require extremely slow scanning rates leading to long total run times with much of the time being spent unproductively in going between points. This problem can be eliminated of course by moving rapidly between positions where data are desired, then stopping grating motion during the data-taking process. This stop-and-go technique is the one used in the Aerospace instrument.

Proper operation of such a system, however, requires a proper regard for the time constants of the detecting system. There are three principal time constants in the detecting system in our instrument: (1) The time constant, τ , of the synchronous detector in the 19-cycle amplifier; (2) the gate time, T , used by the preset counter; and (3) the period $\Delta T \approx 1/3$ seconds required for the grating to move to a new position. The first controls the highest frequency noise that will appear in the output; the second controls the length of time ("integration time") over which the data are averaged; the third is only indirectly under the control of the experimenter.

These filtering parameters are adjusted for any particular run to optimize the conflicting requirements of a low noise level and a reasonable total run time. Failing to recognize that the adjustments are interdependent,

however, may lead to systematic errors in intensity in the final spectrum. If the ratio of the integration time to the detector time constant is too low and if the signal level is quite different from the preceding point, the signal averaged by the counter will be changing over an appreciable portion of the period of averaging. This adds to the interferogram another function proportional to the first derivative of the interferogram.

The magnitude of this contribution can be estimated with the aid of Fig. 59, a schematic representation of the signal changes during one data acquisition cycle. At t_0 , data acquisition at the preceding location is completed; between t_0 and t_1 , the grating moves to a new location and stops. For convenience the signal (solid line) is assumed to vary linearly during this time. At t_1 , data taking at the new point is initiated and continued throughout a period T until time t_2 . The output signal from the 19-cycle detector, with a poor choice of time constants, is shown as the dashed line. The fractional error in the data taken then will be the ratio of the hatched area to the rectangle of area TE_2 . This fractional error is:

$$X = \left(\frac{m-1}{m} \right) \left[\left(\frac{\tau}{\Delta T} \right) \left(1 - e^{-\Delta T/\tau} \right) \right] \\ \times \left[\left(\frac{\tau}{T} \right) \left(1 - e^{-T/\tau} \right) \right]$$

The first set of parentheses represents the amount of change in the signal and thus the largest possible error. The first square brackets represent the decrease in this maximum error because the output signal has some time, ΔT , in which to start to follow the input signal change; the second brackets introduce the error caused by the input to the counter changing during the data taking.

Since the noise is expected to go down with the square root of the integration time, increasing T above about 10 seconds increases the overall run time more than is worthwhile for the improvement in noise. Since a pen recorder runs off the output of the detector, an offhand choice for τ would be a little longer than the 1-second response time of the recorder, possibly 3

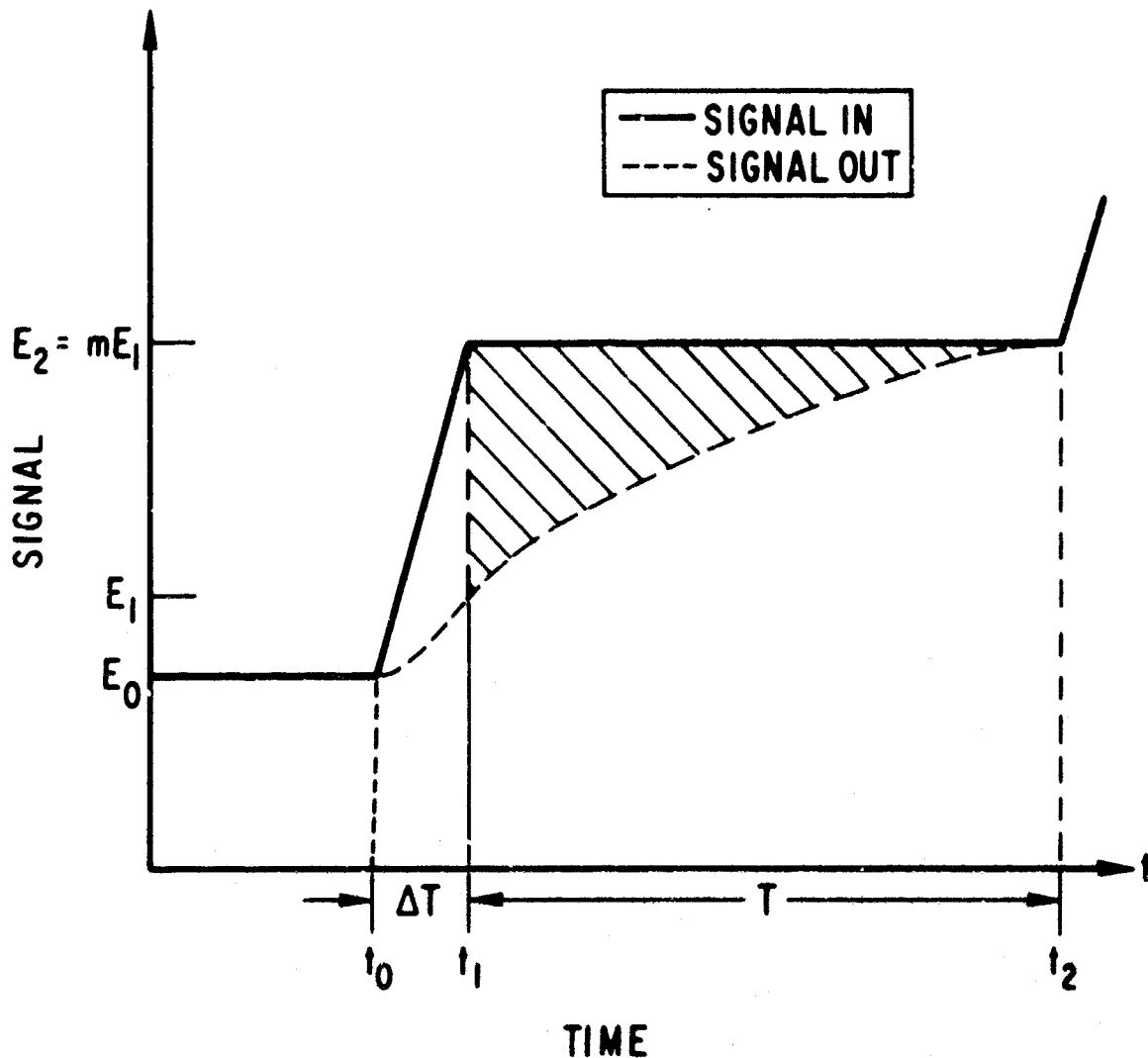


Fig. 59. Schematic representation of signals into and out of the 19-cycle detector during one data acquisition cycle.
 During time ΔT , grating is moving to new position.
 During time T , the "integration time", data are taken.
 Hatched area is the amount by which the final integrated information will be in error due to the constant of the detector.

seconds. With these values almost no correction takes place during the moving time ($[] = 0.95$), whereas, the error during the integration process is still about 30%. The solution is to decrease the detector time constant as much as possible and to independently increase the recorder time constant if desired. If we reduce τ to 0.5 second, 25% of the change can occur while the grating is moving. The error in the integration is about 5%, so the total error is now only a little above 3%, a ten-fold reduction. The effects of this improvement in accuracy in intensity measurements on the transformed spectrum may be seen from Fig. 60, which shows two spectra of a mercury vapor source taken under identical circumstances, except for the time constant of the 19-cycle detector. From this figure, it is apparent that proper choice of time constants is imperative for a system having several cascaded systems, each with a comparable individual time constant.

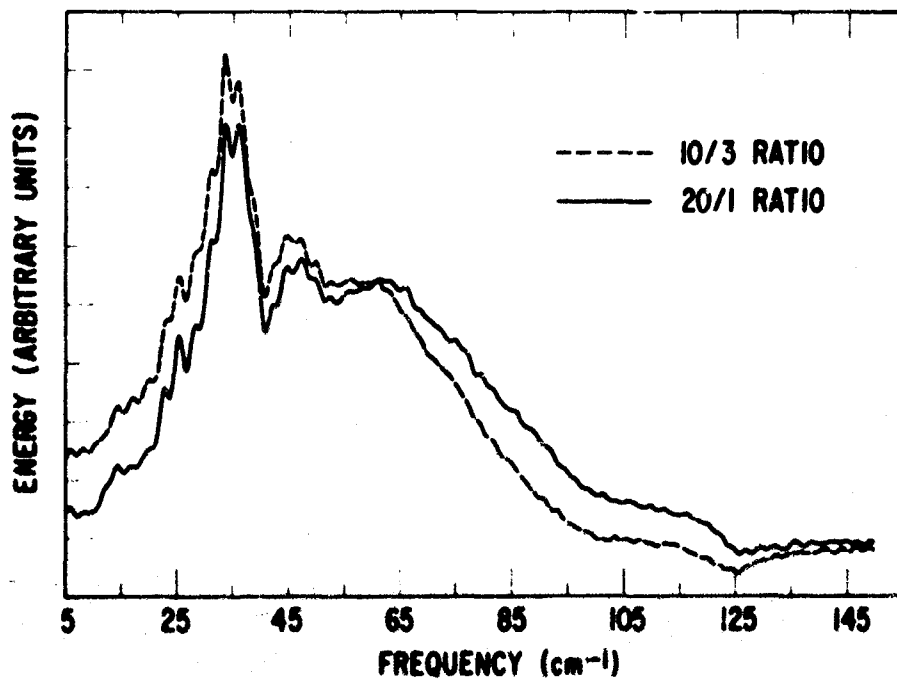


Fig. 60. Effect on the spectrum of a large detector time constant. Both curves are spectra of a medium-pressure mercury vapor source, and except for the detector time constant, were taken under identical operating conditions. The integration time was 10 sec/point. The solid line corresponds to a detector time constant τ of 0.50 sec; the dashed line is the spectrum obtained with a τ of 3 sec.

G. BACKGROUND RADIATION

In any spectrometry, and particularly in the FIR, background radiation competing with that from the sample can introduce serious errors in measurements. It is important that this source of error be understood and that all possible means to minimize it be used. In order to assess this error, consider first the Planck radiation law as applied to these long wavelengths. It can be written

$$E(\lambda) = \frac{c_1 \lambda^{-5}}{e^{-(c_2/\lambda T)} - 1}$$

where c_1 and c_2 are constants and λ and T are the wavelength and the absolute temperature of source. For $\lambda T \gg c_2$, by expanding the exponential and keeping only the leading term, we obtain the Rayleigh-Jeans approximation

$$E(\lambda) = \frac{c_1}{c_2} \lambda^{-4} T$$

where we see that $E(\lambda)$ is simply proportional to T , not rapidly varying as it is for small λ . In a room temperature (300°K) environment with a source at 3000°K (very high for available sources), the radiance ($\text{W/cm}^2 \text{ ster}$) is only 10 times greater for the source. The source in our case fills a solid angle, as seen by the detector through the interferometer, of about $1/50$, whereas, the background fills 2π , which is larger by about 300. Hence, the integrated energy from the background exceeds that from the source by a factor larger than 30 even before absorbing samples are inserted in the beam.

Fortunately, two factors act to greatly reduce the effect of the background. First, most of the background radiation does not pass through the interferometer and it is not modulated by the interferometer displacement; hence, it introduces a constant zero shift in the interferogram that is ignored

in the computer transformation. Second, an even larger fraction of the background is not chopped and the detector response it produces does not contain the 19-cycle modulation frequency to which the amplifier is tuned. Radiation must pass through both the interferometer and the chopper to be transformed into an output spectrum. In any case, however, it adds to the detector noise. Also the chopped-nonmodulated component uses up some of the available dynamic range of the amplifier.

In order to minimize the effects of stray chopped radiation, it is necessary to baffle the system carefully. Baffling in this spectral region is more difficult than it is for the shorter wavelength region because most of the usually black materials are not black. Even black flocking reflects about 20%. Also, ordinarily opaque materials such as heavy cardboard transmit about 10%. Sheet metal appears to be about the only truly opaque baffling material, and we have not found any really good nonreflecting surfaces. We have been able to reduce the chopped-nonmodulated component to less than 10% when highly transmitting samples are being measured, but the percentage increases drastically for absorbing materials.

If an absorbing sample is in the sample holder, the chopped and modulated radiation received by the detector when the sample is being viewed consists of:

1. Desired radiation from the source transmitted by the sample
2. Radiation emitted by the sample
3. Radiation from the surroundings that is reflected by the sample into the beam
4. Radiation, similar to items 2 and 3, from the sample holder and other surrounding structures.

There are similar components in the reference beam which, of course, subtract from the signal due to the sample beams.

It is easy to estimate the effect of sample emission. Consider a source of effective temperature T_s radiating energy through a sample at ambient temperature T_a . The sample has an absorbtivity, a , that equals its emissivity, e .

If the sample were in equilibrium with its surroundings at T_a , it would absorb a fraction, a , of the radiation of wavelength λ passing through it within a given solid angle, but it would also emit an equal amount into the same solid angle. In our case, the source radiation entering the sample is T_s/T_a times as large because of the higher temperature of the source. Hence, the radiation observed is proportional to $T_s(1 - a) + aT_a = T_s - a(T_s - T_a)$. An apparent absorption, $a' = a[1 - (T_a/T_s)]$, is observed that can never be larger than $1 - T_a/T_s$. With the commonly used quartz Hg arc source, the hot quartz is the radiating material for ν near 100 cm^{-1} . If T_s is then $\approx 900^\circ\text{K}$, the error in a is $\approx 30\%$. The observed transmittance will then never be less than 30%.

The reflection by the sample allows the detector to see other emitting surfaces near the sample. These surfaces can have any spectral radiation profiles and hence the distortion introduced into the measured spectrum cannot be predicted. It will not be a simple multiplier as in the case of absorption but may even introduce extraneous features into the spectrum. An interesting special case arises when the sample acts as a partially reflecting mirror perpendicular to the beam. The detector then "sees itself," and since the detector is cooled, the magnitude of the error is reduced. This effect has been observed with metal meshes run single-beam, the reference beam being blocked off by a blackened metal plate. The metal meshes are highly reflective and the detector sees itself in the sample beam, but it sees the 300°K surroundings in the reference beam. The measured "transmittance" is negative as a result.

It should be pointed out that under these circumstances the detector does not see just itself but half of itself and half of the surroundings. The interferometer puts half of incident energy into the central maximum and half into the higher orders. Looking backward through it, we see an extended field of view with half transmittance from the position of the central maximum and half from the positions of the higher orders. Since the detector is very cold, the effective temperature that the detector sees under these conditions approaches $T_a/2$ as extraneous scattered radiation is reduced.

H. DRIFT

During the data taking, changes in signal intensity with time constants of the order of hours are observed. In a particular run there are varying contributions of two types to these changes: (1) an effect correlated with the motion of the lamellar grating as reflected in motion of the interferometer entrance aperture image in the exit aperture; (2) nonreproducible drifts of detector, source, and critical amplifiers. Independent of the cause, however, is the effect of these slow changes on the output spectrum. They lead to an increase in low wavenumber noise in the spectrum and may have some effect on line shapes in higher wavenumber regions of the spectrum.

To illustrate this, we discuss results of a detailed study of a water vapor interferogram which showed a particularly simple long-term change, a more-or-less linear decrease with increasing path difference. This is shown in Fig. 61, which is a plot of averages of 10 adjacent points taken at

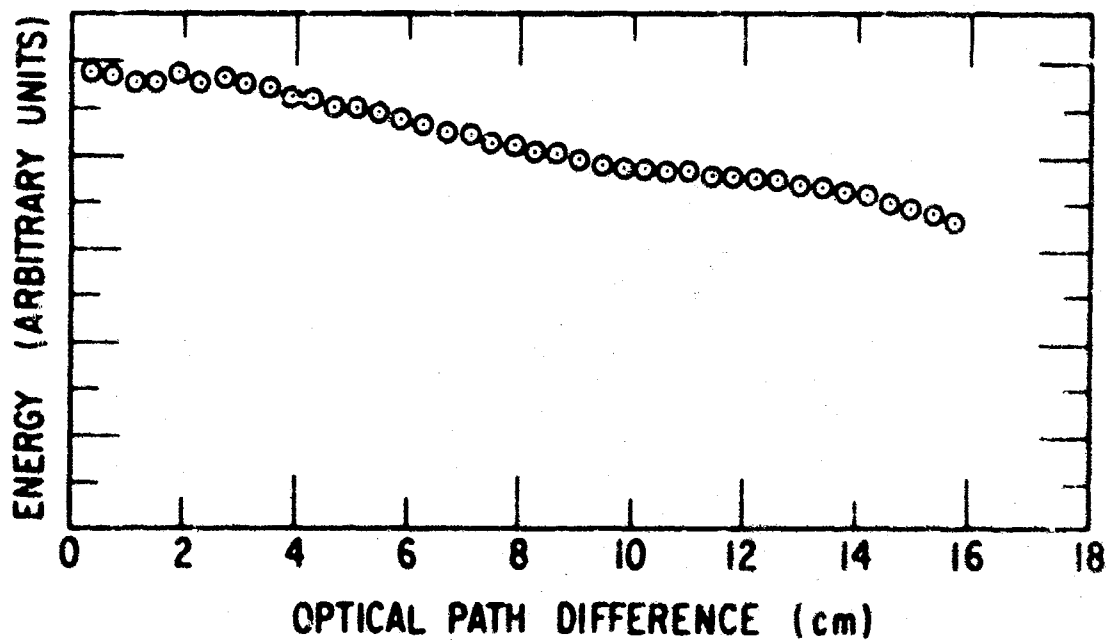


Fig. 61. Averages over adjacent 10-point regions of a water vapor interferogram, showing a case of nearly linear drift.

100-point intervals in the interferogram. A first approximation to the apparent form of the interferogram, $F'_a(x) = F'_w(x_m) + F_a(x)$ is

$$F'_a(x) = F'_w(x) (1 - ax)$$

where $F'_w(x) = F'_w(x_m) + F_w(x)$ is the interferogram due to the water alone, and the quantity in brackets introduces the linear fall-off. The spectrum then is obtained by Fourier transforming $F_a(x)$ and is

$$\begin{aligned} E(v) &= \int_0^{x_m} F_a(x) \cos 2\pi vx dx \\ &= a I_w(x_m) \int_0^{x_m} (x_m - x) \cos 2\pi vx dx \\ &\quad + \int_0^{x_m} F_w(x)(1 - ax) \cos 2\pi vx dx \\ &= \frac{a I_w(x_m) x_m^2}{2} \left(\frac{\sin \pi v x_m}{\pi v x_m} \right)^2 + E_f(v) \end{aligned} \quad (43)$$

The first term in Eq. (43) makes its main contribution at $v = 0$ and falls off proportional to v^{-2} ; although it is large in magnitude at $v \approx 0$ in the region of the spectrum where there is sufficient energy to make observations, $v \gtrsim 20 \text{ cm}^{-1}$, this term will make little contribution.

To gain an idea of the effect of the additional $(1 - ax)$ factor in the integrand of the second term of Eq. (43), it is convenient to assume we are discussing lines with a Lorentzian shape, $E(v) = [(v - v_0)^2 + (\Delta v)^2]^{-1}$, of half maximum width of Δv centered at frequencies v_0 . It has been shown that the

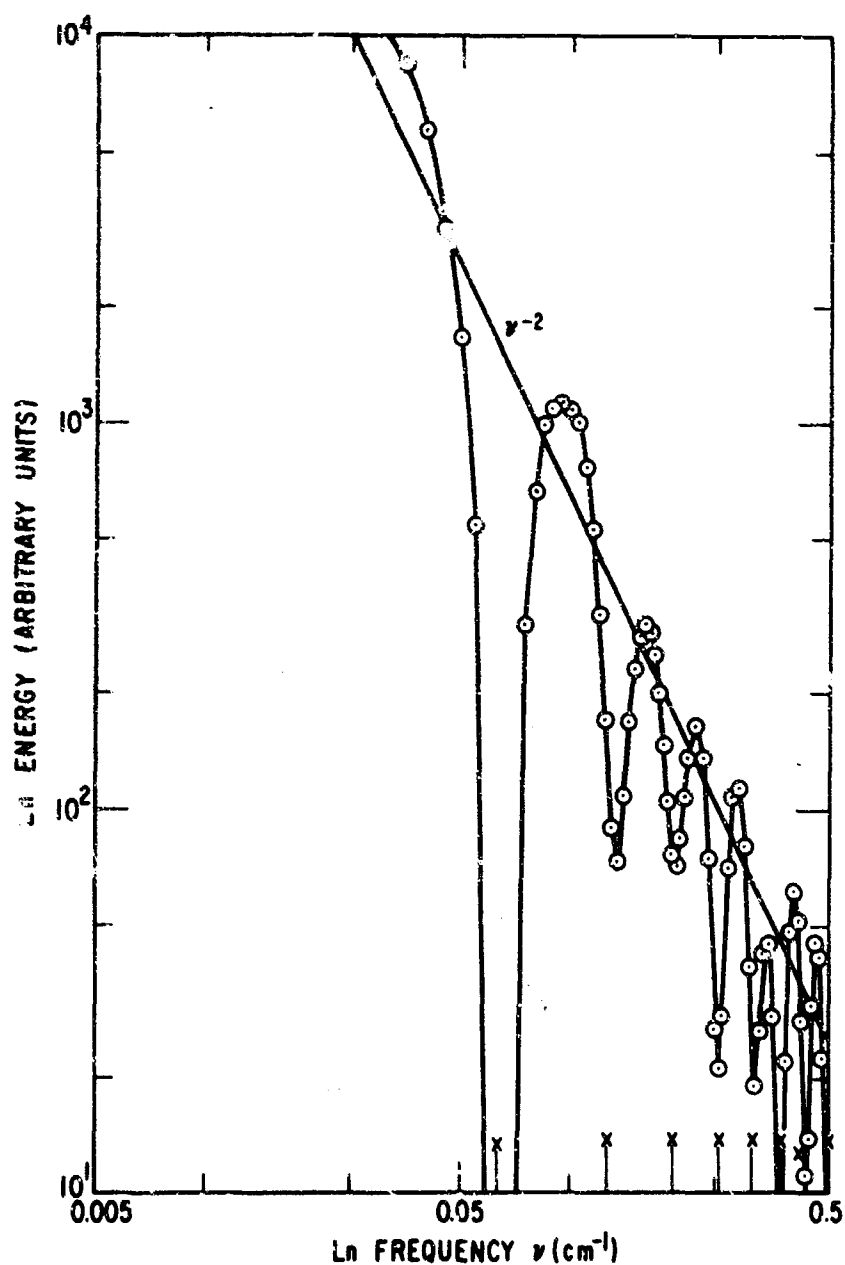


Fig. 62. Difference between the spectrum near $\nu = 0$ as obtained from the uncorrected interferogram and that obtained from the same interferogram after dividing each point by $(1 - ax)$. The straight line has slope -2 , as suggested by the ν^{-2} factor in the first term of Eq. (43). The x-marks along the ν axis are zeros of $\sin \pi \nu x_m$.

interferogram expected from this line is an exponentially decaying cosine, $\cos 2\pi\nu_0 x \exp(-2\pi\Delta\nu x)$. Then the apparent spectrum given by $E_1(\nu)$ for this line will be

$$E_1(\nu) = \int_0^\infty \cos(2\pi\nu_0 x) \cos(2\pi\nu x) e^{-2\pi x \Delta\nu} (1 - ax) dx$$

If a is not too large, $(1 - ax)$ may be thought of as the first terms in the expansion of $\exp(-ax)$. The form of the function to be transformed then is the Lorentz line interferogram. Thus the line shape must also be Lorentzian with an apparent line width $\Delta\nu_a = \Delta\nu + a/2\pi$ somewhat wider than the true line width.

The applicability of this approach is demonstrated by dividing each point in the apparent interferogram by $(1 - ax)$, thus obtaining the actual interferogram. The difference between the transforms of the corrected and uncorrected interferograms near $\nu = 0$ appears as a loglog plot in Fig. 62. The decaying sine curve is obvious. The straight line has the expected die-off slope of -2 and is seen to agree well. Figure 63 shows one of the lines in the water vapor spectrum. The solid line is the transform of the uncorrected interferogram, whereas the dashed line obtained from the corrected interferogram shows the narrowing effect of eliminating the drift from the interferogram.

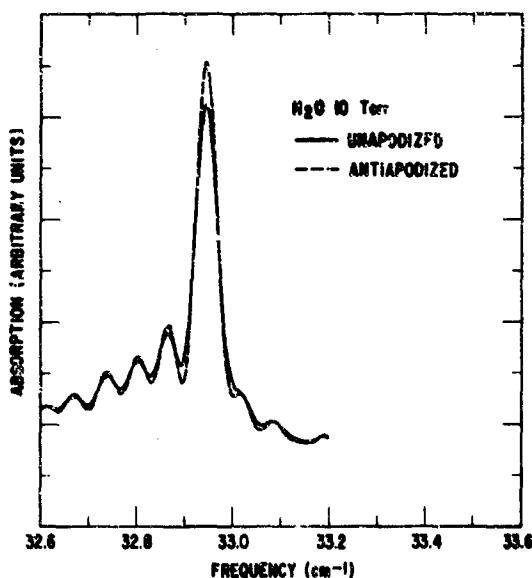


Fig. 63. Lines obtained from the corrected interferogram (dashed line) and from the uncorrected interferogram (solid line). Note the decrease in width at half-maximum intensity obtained at the expense of some increase in the apparent noise in the base line.

The particular analytic expressions developed here are applicable only to interferograms of separated lines of Lorentzian shape which show a drift linear with increasing position. The effect of other long period drifts, however, would be expected to be similar, introducing increased noise at low wavenumbers in the spectrum and making changes in the line shapes at higher wavenumbers.

I. NOISE

Let the interferogram function $F(x_n)$ be measured at points $x_0, x_1, x_2, \dots, x_n, \dots, x_N (= L)$. We assume the separations $\Delta x (= x_j - x_{j-1})$ are all equal and chosen such that $\Delta x = (2v_c)^{-1}$ in accordance with the sampling theory condition (see Section II). In each $F(x_n)$ there will be a contribution that is the noise and is called $A_0, A_1, A_2, \dots, A_n, \dots, A_N$. The A_n are assumed to be independent of x and $F(x_n)$ and furthermore their mean value is zero. We then take as a measure of the noise in the interferogram its standard deviation N_I given by

$$N_I = \left(\frac{1}{N} \sum_{n=0}^N A_n^2 \right)^{1/2}$$

The spectrum is obtained from the interferogram function by Fourier cosine transformation and thus the component of noise in the spectrum, B_m , at v_m is given by¹⁷

$$B_m = \Delta x \sum_{n=0}^N A_n \cos 2\pi x_n v_m$$

¹⁷ For the term $n = 0$, we should use $A_0/2$ rather than A_0 , but as long as N is reasonably large, the error is small.

We shall calculate the B_m only at those ν_m that are independent. The independent ν_m are located $\Delta\nu = (1)^{-1} \text{ cm}^{-1}$ apart, and taking the first ν_m at 0 cm^{-1} we have $\nu_m = m\Delta\nu = m(L)^{-1}$; furthermore, $x_n = n\Delta x$, and $\Delta x = (2\nu_c)^{-1}$. Making these substitutions we obtain

$$B_m = \frac{1}{2\nu_c} \sum_{n=0}^N A_n \cos\left(\frac{\pi nm}{\nu_c L}\right) \quad (44)$$

The mean value of the B_m 's is

$$\overline{B_m} = \frac{1}{M+1} \sum_{m=0}^M B_m = \frac{1}{2(M+1)\nu_c} \sum_{m=0}^M \sum_{n=0}^N A_n \cos\left(\frac{\pi nm}{\nu_c L}\right)$$

Interchanging the sum over m and that over n , and multiplying by $\Delta m (=1)$, and then approximating the sum over m by its limiting integral form, we obtain

$$\overline{B_m} = \frac{1}{2(M+1)\nu_c} \sum_{n=0}^N \int_0^{\nu_c L} A_n \cos\left(\frac{\pi nm}{\nu_c L}\right) dm$$

and making the change in variable $y = (\pi m/\nu_c L)$ the integral reduces to the form $\int_0^\pi \cos ny dy$, which is zero. Therefore $\overline{B_m} = 0$. We proceed to calculate the standard deviation of the noise in the spectrum. Squaring Eq. (44) and

summing over m , we obtain

$$\begin{aligned} \sum_{m=0}^M B_m^2 &= \frac{1}{4v_c^2} \sum_{m=0}^M \sum_{n=0}^N A_n^2 \cos^2\left(\frac{\pi nm}{v_c L}\right) \\ &+ \frac{1}{2v_c^2} \sum_{m=0}^M \sum_{p=0}^N \sum_{r>p}^N A_p A_r \cos\left(\frac{\pi pm}{v_c L}\right) \cos\left(\frac{\pi rm}{v_c L}\right) \end{aligned}$$

Again, by interchanging the sum over m with the other sums and approximating this sum by the limiting integral, then dividing by $M (= N/2)$, we obtain the standard deviation squared of the noise in the spectrum N_s^2 .

$$N_s^2 = \frac{1}{M} \sum_{m=0}^M B_m^2 \approx \frac{L}{4v_c} \cdot \frac{1}{N} \sum_{n=0}^N A_n^2$$

Therefore,

$$N_s = \left(\frac{L}{4v_c}\right)^{1/2} N_I = \left(\frac{L \Delta x}{2}\right)^{1/2} N_I \quad (45)$$

which is equivalent to the expression given by Connes (Ref. 6) and Bell (Ref. 8). We have carried out the following numerical exercise to confirm Eq. (45). One thousand numbers were chosen randomly with a normal (Gaussian) distribution such that the standard deviation was 1000 units. These one thousand numbers were then used on a noise interferogram and were Fourier cosine transformed with various values of L and Δx . The standard deviation in the noise spectra were then computed, and the results are summarized in Table 13. The ranges of L and Δx were chosen to be representative for the FIR region. Equation (45) predicts that, if Δx is decreased (or v_c multiplied)

Table 13. Calculated (from Eq. 45) and Observed Standard Deviations

L, cm	$\Delta x, \mu$	N_I	N_S (calc)	N_S (obs)
4.00	40	1000	89	86
3.60	40	1000	85	83
3.20	40	1000	80	79
2.80	40	1000	75	74
2.40	40	1000	69	69
2.00	40	1000	63	64
8.00	80	1000	179	172
4.00	80	1000	127	126
6.00	60	1000	134	131
3.00	60	1000	95	97
2.00	20	1000	45	44
1.00	20	1000	32	31
1.00	10	1000	22	21
0.50	10	1000	16	15

by a factor R , the noise in the spectrum will be reduced by a factor $R^{1/2}$. The number of points will of course be increased by R (for constant L). Thus, if the same amount of time is available for the measurements, N_I will be increased by $R^{1/2}$ resulting in no change for N_S . In practice, however, it is still advisable to select Δx as large as possible equal to $(2v_c)^{-1}$ to minimize the "dead time" (the time it takes the interferometer to go from point to point, during which no data are taken), since in general the smaller Δx becomes the more dead time there will be per unit length of optical path difference.

Making Δx as large as possible also minimizes the total number of points in the interferogram which can be of some consequence when computer economics are considered.

Connes (Ref. 6) has considered the case of an interferogram that is a cosine function. This corresponds to a line in the spectrum having zero width. The signal (maximum intensity of the line) is proportional to L , and therefore the S/N is proportional to $L^{1/2}$. For such a case the interferogram should be carried out as far in optical path difference as possible since an increase in L always increases the S/N in the spectrum. This is a limiting case and is appropriate when the resolution attained in the interferogram (governed by L) is much less than the width of the line. When the resolution becomes comparable to the line width, then the dependence of S/N in the spectrum will be different than the $L^{1/2}$ dependence.

Consider a spectrum $I(v)$ made up of a single line having a Lorentz shape. This line shape was chosen since it represents a good description of weakly absorbing pressure broadened lines, and is mathematically tractable for the Fourier cosine transformation we wish to carry out. And now calling the signal in the spectrum, $S_S = I_L(v_0)$ (see Eq. 10),

$$S_S = I(v_0)(1 - e^{-|2\pi\epsilon L|}) \quad (46)$$

and therefore the S/N in the spectrum is

$$\frac{S_S}{N_S} = \frac{S_I}{N_I} \left(\frac{8v_c}{\pi\epsilon} \right)^{1/2} \left[\frac{1 - e^{-|2\pi\epsilon L|}}{(2\pi\epsilon L)^{1/2}} \right] \quad (47)$$

where $S_I = F(0)$, the maximum signal in the interferogram.

The S/N in the spectrum has a maximum when $L\epsilon \approx 0.200$. For $L\epsilon < 0.2$, the S/N curve rises $\sim L^{1/2}$ as is to be expected since $L < 1/\epsilon$; for $L\epsilon \sim 0.2$ the curve flattens out, then falls gently toward the asymptotic

dependence of $L^{-1/2}$. If x is set equal to $(5\epsilon)^{-1}$ in the interferogram function (see Section II), then the amplitude of the interferogram function at this value of x will be down to $\sim 28.5\%$ of its maximum value at $x = 0$. Thus, for maximum S/N in the spectrum, the interferogram should be terminated when it has been damped down to 28.5% of its maximum value.

In Fig. 64 is a plot of $I_L(v)$ for $L\epsilon = 0.200$, and also $I(v)$. The intensity of $I_L(v)$ differs markedly from $I(v)$. It is $\sim 28\%$ lower. Also, the characteristic sidelobes, or feet, are quite prominent. For $L\epsilon = 0.200$, the intensity of the first sidelobe (the strongest) is (measured from the first minima to the second maxima) $\sim 16\%$ of the central maxima (measured from the first maxima to the first minima). In such a spectrum, if the S/N is greater than ~ 6 , these sidelobes might be interpreted as real lines and, therefore, it would be desirable to suppress them. The sidelobe intensity depends on L , and in general the sidelobe intensity will be decreased by making L larger.

The quantity I_F (discussed in Section II) represents the maximum intensity of the first (and strongest) sidelobes; therefore, $I_L(v_0)/I_F$ measures the maximum intensity to sidelobe intensity. There is little to be gained in carrying the interferogram beyond that L which yields $I_L(v_0)/I_F$ much larger than the S/N. The function $I_L(v)/I_F$ vs $2\pi L\epsilon$ is shown as curve D in Fig. 65. Also shown are three S_N/S curves characterized by the parameter

$$\frac{S_I}{N_I} \left(\frac{8v_c}{\pi\epsilon} \right)^{1/2} = 100 \text{ (curve A)} ; 300 \text{ (curve B)} ; \text{ and } 500 \text{ (curve C)}$$

Consider for example curve B. If maximum S/N in the spectrum is required the interferogram should be cut off where $L\epsilon \approx 0.20$, as discussed previously, and this would yield a S/N in the spectrum of $\sim 190/1$. However, if we require that the sidelobes be the same size as the noise, then we are interested in where curve B intersects curve D, which happens at $2\pi L\epsilon \approx 5.35$. The S/N in the spectrum will then be $\sim 130/1$. In this case the interferogram will be carried down to $e^{-5.35} \approx 0.005$ of its maximum value. Then the difference

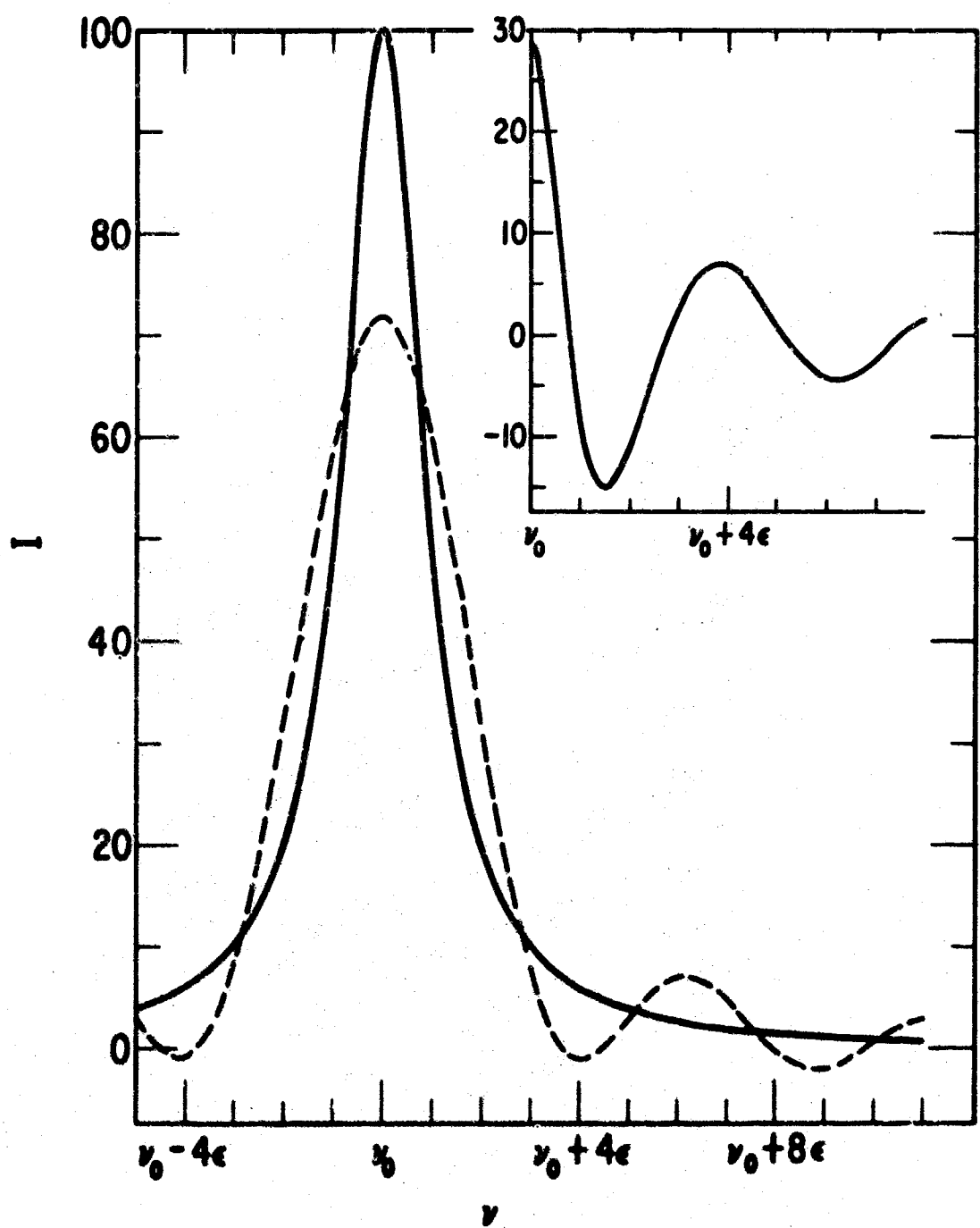


Fig. 64. $I(\nu)$, solid curve, and $I_L(\nu)$, for $L = (5\epsilon)^{-1}$, dashed curve.
The inset shows $I(\nu) - I_L(\nu)$ at the same scale.

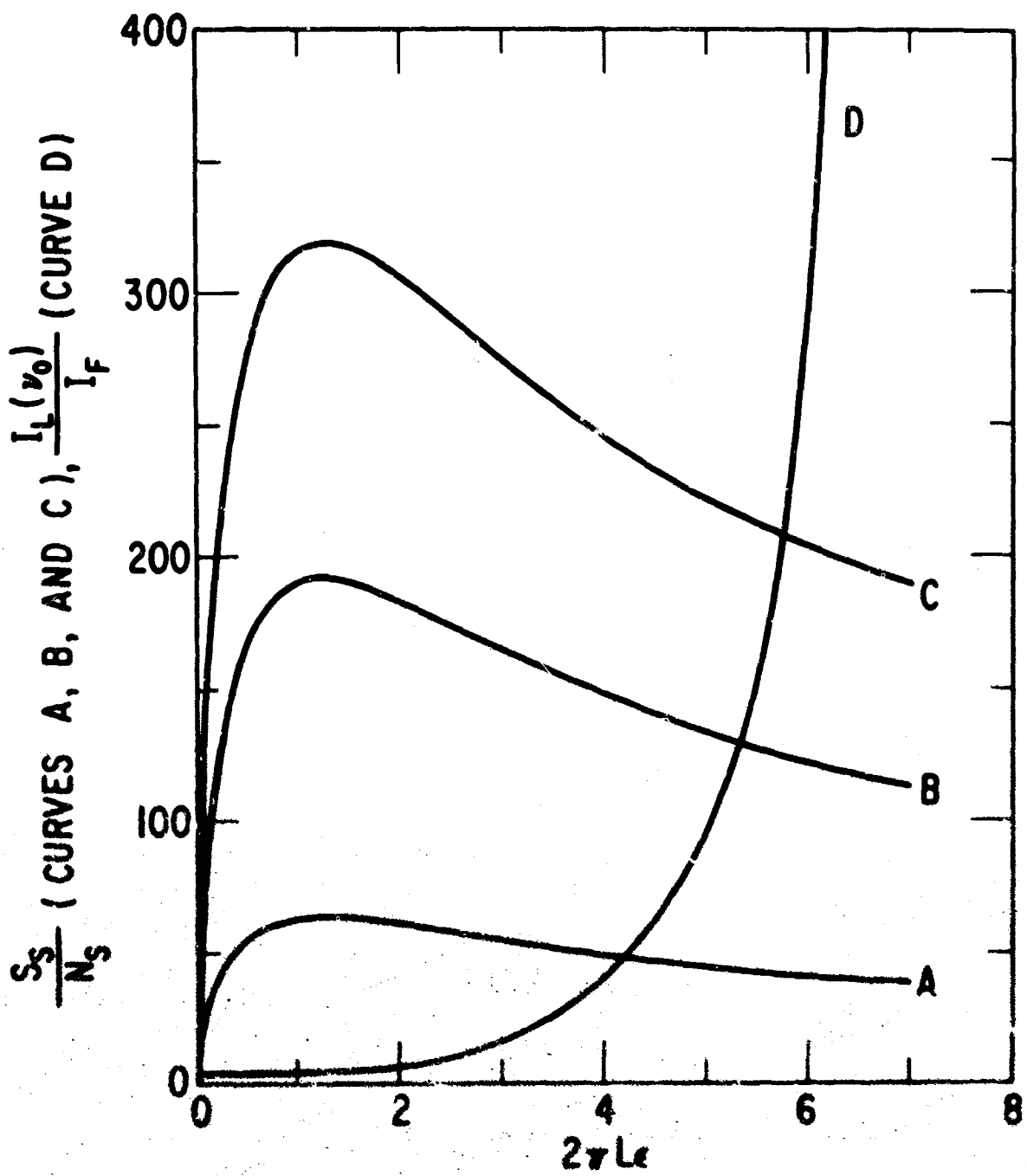


Fig. 65. Spectrum S/N curves (A, B, and C), and maximum intensity to sidelobe intensity curve (D).

$I(v_0) - I_L(v_0)$ will be also within the noise. If $(8v_c/\pi\epsilon)^{1/2} > 1$ (and generally it is), then the interferogram will be carried out beyond where the signal in the interferogram is lost in the noise of the interferogram.

Two-beam interferometry is usually applied to rather broad band absorption investigations (this does not of course exclude high resolution). This will lead in general to two complications not considered in the previous discussion. First, the quantity we have been calling the signal in the interferogram (which can be thought of approximately as the variation of the interferogram about its average value) is usually only a small percentage of the total signal detected by the detector. This is the well-known dynamic range problem of two-beam interferometry. It can be suppressed by the technique of double-beam differencing (see Section III). Second, usually more than one line is present in the spectrum being examined interferometrically, and the line width parameters ϵ may not all be equal. Thus, the interferogram will not have a simple damped cosine form, but rather will be the net result of many of these terms (one for each line). In the case of diatomic and linear molecules the arguments of these cosines are related nearly harmonically and the grosser features of the interferograms are its well-known signatures (Refs. 22, 23), and the damped amplitude of these signatures are then a measure of the (total) signal in the interferogram.¹⁸ At the other extreme is the pure rotational interferogram of the water molecule. This interferogram is very irregular (Ref. 15); however, the amplitude does decay (on the average) as one goes to larger x and an average assessment of the damping is possible. To a certain extent in pure rotational spectroscopy the line width parameter is somewhat in the control of the experimenter since it depends on the pressure of the absorbing gas. For best S/N in the spectrum, the pressure in the absorption cell should be fixed so that the average of the signal in the interferogram in the vicinity of

¹⁸ A word of caution, however. In the pure rotational interferogram (Ref. 15) of DCI, the signatures die out and then come back at larger L because the spectrum is made up of a series of closely spaced doublets.

$x = L$ is ~28% of the average of the signal in the vicinity of $x = 0$ (the region about $x = 0$ should be excluded from the average). This will provide (on the average) the best compromise between S/N in the spectrum and sharp lines and presumably the best condition for wavenumber measurements. If there are overlapping lines the presence of the sidelobes will, in general, introduce an error in the wavenumber measurements. This is discussed later.

The line shape assumed is a good approximation for weak absorption. For more strongly absorbing lines the Lambert-Beers law is more appropriate, and in general the line shape will be modified.¹⁹ If such a line (hereafter called Lorentz-Lambert-Beers line or, for short, LLB line) is compared with a Lorentz line normalized such that both have the same maximum intensity and same effective half-width at half-maximum, then the L line will be "squarer" in the sense it is broader (more intense) between $v_0 - \epsilon_{\text{eff}}$ and $v_0 + \epsilon_{\text{eff}}$ and narrower (less intense) outside this range. We have generated a number of $I_{\Delta}(v)$ for various values of $\gamma(v_0)l > 1$ and Fourier cosine transformed these functions, the result being the interferogram function they would present. In the region $x(\epsilon)_{\text{eff}} < 1$ these interferograms were damped out $\sim \exp[-|2\pi\epsilon_{\text{eff}}x|]$, but in the region $x(\epsilon)_{\text{eff}} \sim 1$ the cosine modulation came back with amplitude small but not negligible in comparison with its amplitude near $x = 0$. To a first order of approximation the difference between these two line shapes looks like two lines separated by ϵ_{eff} and thus one would expect subsidiary maxima and minima when $x(\epsilon)_{\text{eff}} = 1, 2, \dots$. The magnitude of the amplitude of the interferogram at $x(\epsilon)_{\text{eff}} = 1, 2, 3, \dots$ is of course determined by the difference between the LLB line shape and the

¹⁹When an interferogram is measured using the double-beam differencing mode of operation (Ref. 15) the result (after Fourier cosine transformation) is not $I(v)$ the spectrum, but rather $I_{\Delta}(v) = [I_o(v) - I(v)]$, where $I_o(v)$ is the spectrum that would be obtained with no sample in the cell. If we assume a Lambert-Beers law for absorption, we have $I_{\Delta}(v) = I_o(v)[1 - e^{-\gamma(v)l}]$, where $\gamma(v)$ is the absorption coefficient and l the absorbing path. For $\gamma(v)l \ll 1$, this reduces to $I_{\Delta}(v) \approx I_o(v_o)W(v)l$. For pressure broadened lines $\gamma(v)$ has the form given by Eq. (24).

Lorentz line shape. As far as the spectrum is concerned the contribution from these parts of the interferogram will "square" out the line.

We have assumed no error in the measurement of x , the optical path difference.²⁰ Such an error can be quite degrading as far as S/N in the spectrum is concerned. Consider for example an interferogram which has large amplitude features, such as signatures. In the vicinity of a signature, the rate of change of intensity in the interferogram is very large with respect to a change in x , and thus a small error in x could lead to a large change in intensity of the interferogram. This is very undesirable in that the apparent noise generated by such an error could be very much larger than the true noise. Furthermore, these larger apparent noise excursions occur at exactly those places in the interferogram that correspond to the positions of greatest contribution to the intensity of the lines in the wavenumber spectrum. Thus the noise level in the wavenumber region of the lines could be greater than in the wavenumber regions where there are no lines.

Finally, we consider the question of resolution. Shown in Fig. 66 are two identical lines with $L\epsilon = 0.200$ (optimum S/N situation) separated by 4ϵ . The dip in intensity between the lines is $\sim 11\%$ (somewhat smaller than the Rayleigh criterion; if the separation were $\sim 4.2\epsilon$ the dip in intensity would be $\sim 18\%$, very close to the Rayleigh criterion). The lines are separated by 4ϵ but appear (measurement of maximum intensities) to be separated by $\sim 3.8\epsilon$. Well separated lines could be measured more accurately (depending of course on the S/N). Apodization of the interferogram would suppress the sidelobes, but little or no gain in measurement accuracy would be expected since the lines would then be broader and their central intensity region would overlap even more.

²⁰If the error is constant (i.e., mislocation of the origin, $x = 0$) then serious shifts and distortions of line shape may result. If the error is periodic, ghosts will be seen in the spectrum (Ref. 6). See Section V-A, B.

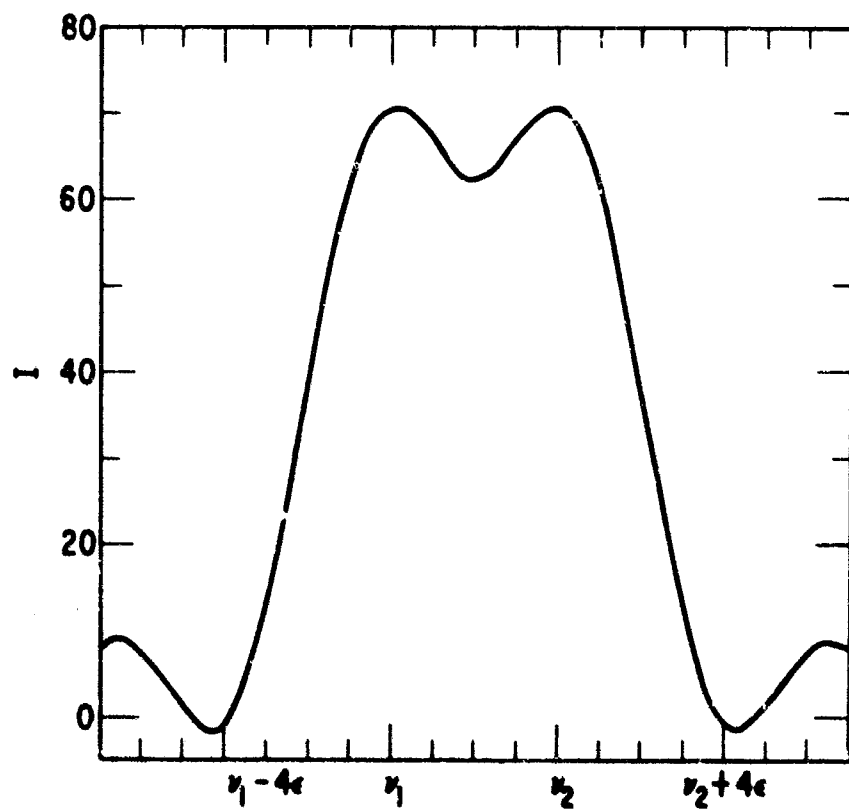


Fig. 66. Two identical Lorentz lines separated by 4ϵ , and $L\epsilon = 0.200$.

VI. COMPUTATIONAL TECHNIQUES

A. INTRODUCTION

Development of efficient means to carry out the calculations indicated in Eq. (5) has enabled Fourier transform spectroscopy to become a practical means of spectroscopy. Because the computational techniques are so necessary, this section is devoted to a discussion of the algorithms used and tests that may be applied to them, and it closes with a brief discussion of programming the algorithms for use on a high speed computer, including flow diagrams. With detectors presently available, the only meaningful energy information available is relative, not absolute. Because of this, constant factors are customarily left out of the equations of Fourier transform spectroscopy. When this is done, Eq. (5) becomes

$$E(v) = \Delta x \left[F(0) + 2 \sum_{j=1}^N F(j\Delta x) \cos 2\pi j v \Delta x \right] \quad (48)$$

Notice the finite sampling of the interferogram forces the computed spectrum $E(v)$ to be periodic with period $1/\Delta x$. Furthermore, since $\cos(y + n\pi) = \cos(y - n\pi)$, $E[v + (1/(2\Delta x))] = E[(1/2)\Delta x - v]$, all the information must be contained in a frequency band between 0 and $(2\Delta x)^{-1}$ [or in general v and $v + (2\Delta x)^{-1}$].

B. COMPUTATIONAL ALGORITHMS

The computational algorithms used must carry out the operations indicated in Eq. (48) as efficiently as possible. Two algorithms have been developed, each with particular advantages.

1. DIRECT SUM ALGORITHM

The conceptually simplest way to carry out Eq. (48) for a given value of v is to take a value of $F(n\Delta x)$, multiply by the required cosine, and add

the result to the sum of the preceding manipulations. This involves N multiplications and finding N cosines for each output point. If we define a "manipulation" as one addition, one multiplication, and finding one function, to obtain M output points from an interferogram of N points will require NM manipulations. By far the slowest of these processes is the calculation of the cosine by the computer. This can be speeded up, however, because all the arguments for the cosines needed to calculate the transform at one frequency are integrally related to each other. This allows the use of the recursion formula

$$\cos(nx) = 2 \cos(x) \cos[(n-1)x] - \cos[(n-2)x] ; n = 1, 2, \dots$$

The recursion formula, however, introduces accumulated roundoff error into the cosines. In practice, a compromise is sought by periodically computing a set of cosines from the basic definition while obtaining most of the cosines from the recursion relation. Even with this feature the computer takes about 40 μ sec per input-output point, meaning a spectrum of 4000 points in and 4000 out would take about 11 minutes.

2. COOLEY-TUKEY ALGORITHM

It was noticed that if certain simplifying restrictions were made on the relationship between input point spacing Δx and output point spacing Δv , a number of similarities existed between the computation of Fourier series and the factorial experimental designs familiar to statisticians. From this, Cooley and Tukey (Ref. 86) have developed algorithms suitable for general complex Fourier series computation. Forman (Ref. 87) was the first to bring these algorithms to the attention of spectroscopists. The algorithm computes the output spectrum of M points by means of several intermediate arrays, each of which also contain M points. The trigonometric weighting is not calculated all at once for each interferogram point but partially applied each time a new array is computed.

The most convenient way to accomplish the weighting is to use complex exponentials, since the weighting function of the sum of two arguments may then be obtained by the multiplication of the two weighting functions. It becomes very convenient to also require that $\Delta v \Delta x = 1/M$, the number of output points. If we let $E(v) = E(k \Delta v) = 2 \Delta x \operatorname{Real}[T(k)]$, $S(j) = F(j \Delta x)$, $j = 1, 2, \dots, N$, and $S(0) = F(0)/2$, Eq. (48) may be rewritten compactly as

$$T(k) = \sum_{j=0}^N S(j) W^{jk} \quad (49)$$

where $W = \exp(i2\pi/M)$ and $N =$ the number of input points.

All the information in the interferogram can be obtained if $M = N$; however it is often convenient to have the output points more closely spaced. Forman has pointed out that this can be effectively done by extending the interferogram function with zeroes, until it has M points. In the following proof of the algorithm it is shown that the same effect can be obtained with the calculation of fewer intermediate arrays if calculation of the first array is modified slightly. The success of the method depends on N and M being highly composite numbers, the most efficient base being 3. It may be shown however (Ref. 86) that either base 2 or 4 is only about 6% less efficient, and for some methods of programming digital computers a binary-based system is much more convenient; therefore, this will be the system used for our demonstration of the algorithm.

The interferogram is required to have $N = 2^n$ points, extending the actual data with zeroes if necessary. The spectrum is desired at $M = 2^m$ output points with $m = n + p$; m , n , and p all being positive integers. It is convenient to express j and k explicitly in binary notation

$$k = k_{m-1} 2^{m-1} + k_{m-2} 2^{m-2} \dots k_0 = \sum_{l=0}^{m-1} k_l 2^l$$

$$j = j_{n-1} 2^{n-1} + k_{n-2} 2^{n-2} \dots j_0 = \sum_{\ell=0}^{n-1} j_\ell 2^\ell$$

When the sum (Eq. 49) is rewritten in the following way, the final result can be computed in n passes through the data, each pass involving the calculation of M points, corresponding to the n summations over the binary digits.

$$T(k) = \sum_{j_0=0}^1 \sum_{j_1=0}^1 \dots \sum_{j_{n-2}=0}^1 \left[\sum_{j_{n-1}=0}^1 S(j_{n-1}, \dots, j_0) W^{j_{n-1} k 2^{n-1}} \right] \\ \times W^{j_{n-2} k 2^{n-2}} \dots W^{j_0 k}$$

The only dependence on binary digit j_{n-1} is enclosed within the square brackets; thus we can eliminate it from the sum by carrying out the summation and define the result as S_1 .

$$S_1(k_p, \dots, k_0, j_{n-2}, \dots, j_0) = \sum_{j_{n-1}} S(j_{n-1}, \dots, j_0) W^{j_{n-1} 2^{n-1} (k_0 + \dots + k_p 2^p)} \\ \times W^{j_{n-1} M (k_{p+1} + \dots + k_{m-1} 2^{n-2})}$$

Since W raised to any integer power is unity, the right-hand factor of this equation is always 1, making S_1 depend only on $k_0 \dots k_p, j_0 \dots j_{n-2}$, as we have indicated in the argument of S_1 . This process is repeated on the next innermost sum to obtain S_2 and so on until the last summation over j_0 yields the desired transform. The relation between arrays on two successive passes may be summarized by the recursion formula

$$\begin{aligned}
 & S_{l+1}(k_{p+l}, \dots, k_1, k_o, j_{n-l-2}, \dots, j_o) \\
 &= \sum_{j_{n-l-1}} S_l(k_{p+l-1}, \dots, k_o, j_{n-l-1}, \dots, j_o) \\
 &\quad \times W^{j_{n-l-1}} (k_o 2^{n-l-1} + \dots + k_{p+l} 2^{m-1}) \tag{50}
 \end{aligned}$$

If we define $S_o(0, \dots, 0, j_{n-1}, j_{n-2}, \dots, j_o) = S(j_{n-1}, \dots, j_o) = S(j)$, the computation can be carried out by applying the recursion scheme Eq. (50) to the M points in the S_o array to obtain the S_1 array, and repeating the operation a total of n times. The calculation of one point in one array requires two multiplications, two additions, and the finding of two exponentials. In the entire computation then there are nM points to be computed, meaning

the total number of manipulations (as defined earlier) is $4 nM = 4M \log_2 N$. The extra factor of 2 is introduced because of the complex operations, making this relation directly comparable with the NM manipulations required in the Direct Sum scheme. The saving in time for long runs may be seen in Fig. 67, which is a comparison of IBM 7090 running time for the same data processed by two programs, differing only in the algorithm used for the transform. A similar curve has not been obtained for the CDC 6000 series computers, but the scaling factor appears to be about 6, since data requiring 4096 input and output points takes about 26 seconds of 6600 central processor time as compared with the

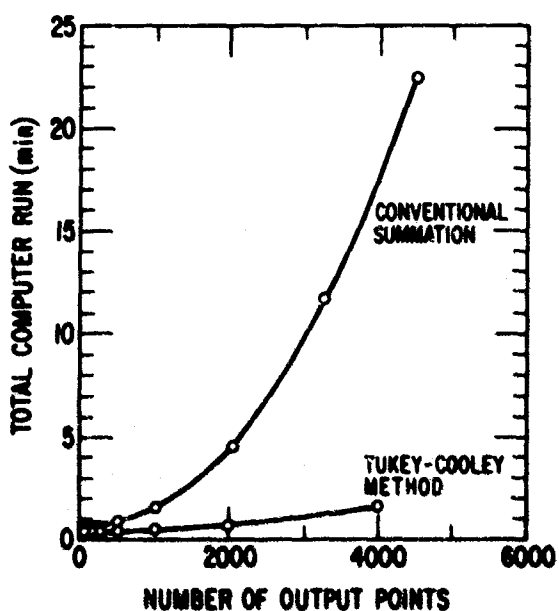


Fig. 67. Comparison of computing times for the Direct Sum and Cooley-Tukey algorithms on the same data run on an IBM 7090 computer.

1. 8 minutes required on the 7090 system. The time required for a single manipulation is still not the same for both algorithms, since by proper choice of a programming scheme only $4(M-1)$ sines and cosines are needed by the Cooley-Tukey algorithm as compared with the NM required in the Direct Sum algorithm. For this number, it is practical to calculate each trig function from its argument rather than use recursion relations with their accumulating error. However, since all advantages are not on the side of the Cooley-Tukey algorithm, it is reasonable to turn next to a comparison of the two methods.

3. COMPARISON OF ALGORITHMS

The Direct Sum method gives output points at intervals Δv input to the program. It uses a minimum of computer memory, needing only enough to store the N points of the interferogram plus the actual number of output points N_o desired for a total requirement of less than $2 N_o$ locations. These two features make this algorithm particularly attractive in studies of small regions of the spectrum where, for convenience, a great number of points per resolution width is desired. No information is gained in addition to that possible from interpolation with an appropriate function in a spectrum with the number of output points equal to the number of input points, but it is simpler to not involve additional computer programs. A disadvantage of this method is the large amount of time required.

The Cooley-Tukey method solves the time problem, but it has other disadvantages. It is required that $\Delta v = 1/M\Delta x$. Because Δx is specified by the experimental conditions of the interferometer, the only possible variation in Δv is through the choice of M ; but since M must be an integral power of 2, the choices are limited. The resulting Δv is seldom a simple number, which may be of some inconvenience if further hand computation on the spectrum is required. A more serious limitation is the memory required by this method. The algorithm calculates the arrays S_i at all the points between 0 and $1/L$ at a spacing of Δv . As pointed out earlier, the only portion of the transform of interest is from 0 to $1/2 L$; thus $M = 2 N_o$ or

twice as many points are calculated as are desired in the final spectrum, requiring $2 N_0$ locations. Points are needed for calculating the S_{i+1} array in a different sequence than they occur in the S_i array, so some provision must be made to save at all times at least part of the preceding array (the minimum amount convenient for saving is half). This requires N_0 more locations. Since each of these $3 N_0$ locations must store a complex number, with both real and imaginary parts, the memory requirements are for $6 N_0$ locations or three times the memory requirements of the Direct Sum method. Because even large computers typically have only about 32,000 cells of core memory, N_0 is limited at present to a maximum of 4096 points, in turn limiting the smallest spacing between points, $\Delta\nu_{\min}$, to a value somewhat greater than would be convenient on many occasions. We are at present considering the possibility of writing a special program, taking advantage of the 60-bit word size in the CDC 6000 computers, to store in the same computer word the real and imaginary part of each element in the S array, allowing our maximum number of points to be doubled and the minimum spacing between output points halved.

Each algorithm then has its advantages. The Cooley-Tukey algorithm is particularly suited for scans of wide-frequency regions at high resolution. The Direct Sum approach is particularly suitable for detailed studies of a narrow-frequency range with a small output point spacing chosen for convenience in further analysis.

4. TEST PROBLEM

In checking any computer program it is desirable to have a problem simple enough to be worked by hand, and yet one which tests the capabilities of the program. The function we have chosen to check the Fourier cosine transform algorithms is a straight line $F(x) = E_0(1 - x/x_m)$ for $0 \leq x \leq x_m$, and $F(x) = 0$ for $x > x_m$. The interferogram, as plotted by the computer, is shown in Fig. 68. The transform as obtained by the computer is listed in

T2 TEST INTERFEROGRAM STRAIGHT LINE

16 01/05/67.

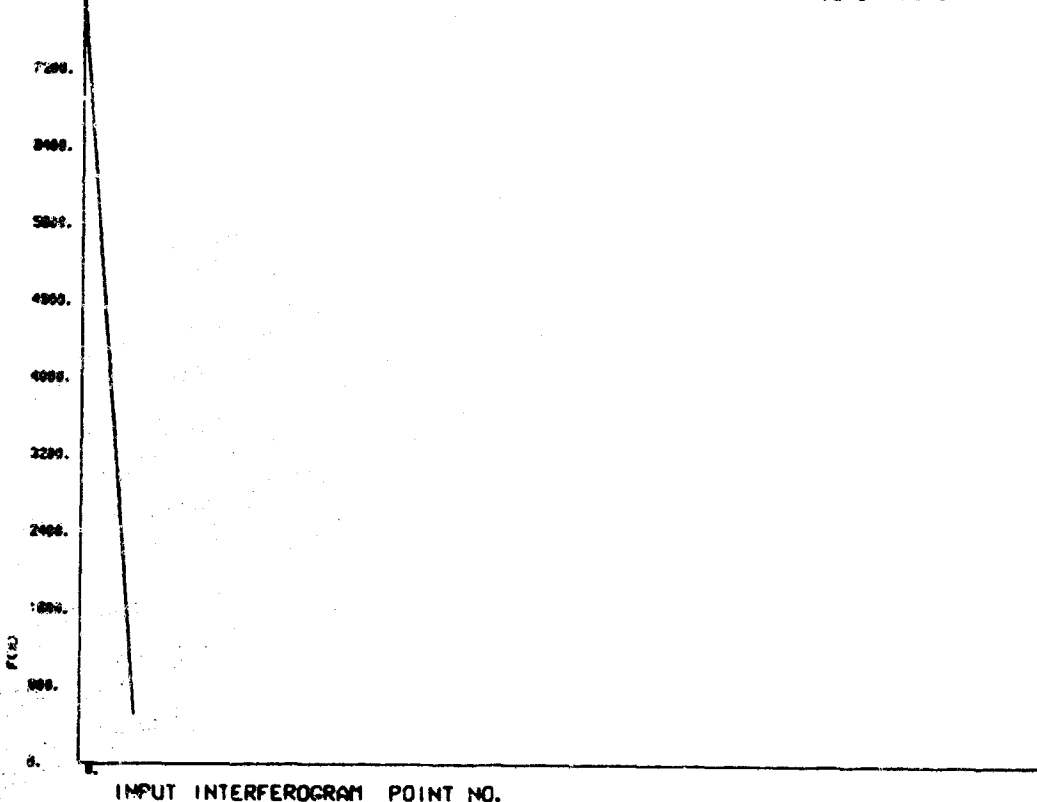


Fig. 68. Test interferogram as plotted by the computer.

Table 14 and shown as plotted by the computer in Fig. 69 for $E_0 = 8000$, $\Delta x = 0.1$, which leads to $x_m = 1.6$ and $v_c = 5$. The computations have intentionally been extended to $2v_c$, so the periodicity of the function discussed earlier could be demonstrated. The two series algorithms agree to within ± 1 in the eighth significant figure, and they agree with test hand calculations made at a few output points to within the error of the cosine tables available for the hand calculations.

The integral transform for this simple interferogram can of course also be calculated in closed form and the result is

$$E(v) = E_0(1 - \cos 2\pi x_m v) / (4\pi^2 x_m v^2) \quad (51)$$

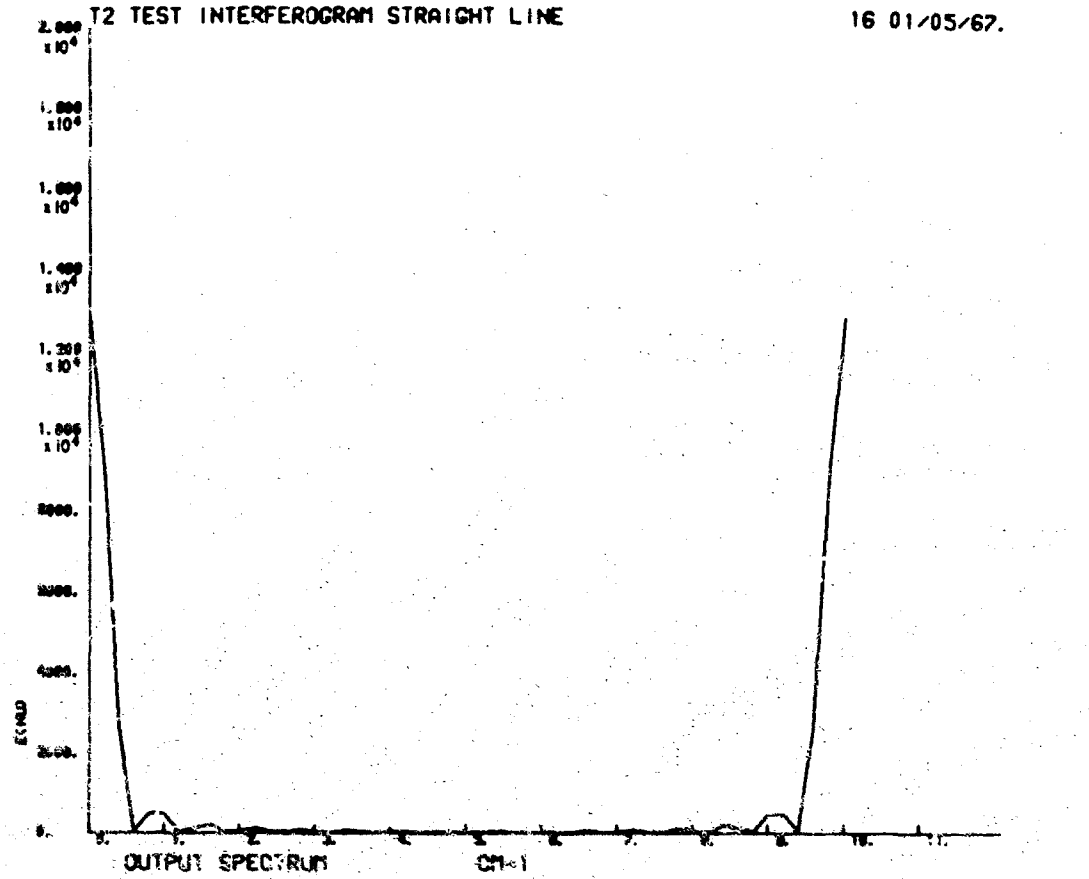


Fig. 69. Transform of test interferogram as computed and plotted by the computer.

This has been evaluated for the values of v where sum results are available, and these results are also listed in Table 14.²¹ From the above discussion of computational precision it is apparent the differences between the evaluation of Eq. (50) and the sum evaluation cannot be due to computational errors. The differences arise rather from the finite sampling of the interferogram, as may be seen from Fig. 70, where the differences between the integral transform and sums are plotted for a Δx of 0.05 and 0.1, which leads to

²¹To facilitate comparison between the integral results and computer results, the factor of 2 dropped in obtaining Eq. (48) is reinserted as a multiple of this integral.

Table 14. Comparison of Integral Transform and Sum Transform
of Straight Line Interferogram

ν (cm ⁻¹)	$\frac{E_0}{2\pi^2 x_{in}^2} (1 - \cos 2\pi x_m \nu)$	$2E(\nu)$ (computer sum with $\Delta x = 0.1$ sampling)
0	12800.000	12800.000
0.15625	10375.289	10383.627
0.3125	5187.6446	5204.3434
0.46875	1152.8099	1161.1795
0.625	0	$\sim 10^{-8}$
0.78125	415.01157	423.44627
0.9375	576.40496	593.36480
1.09375	211.74060	220.27446
1.25	0	$\sim 10^{-8}$
1.40625	128.08999	136.75898
1.5625	207.50578	225.00743
1.71875	85.746192	94.588898
1.875	0	$\sim 10^{-8}$
2.03125	61.392244	70.450783
2.1875	105.87030	124.23754
2.34375	46.112396	55.433426
2.5	0	$\sim 10^{-9}$
2.65625	35.900655	45.536630
2.8125	64.044995	83.675684
2.96875	28.740413	38.751138
3.125	0	$\sim 10^{-8}$
3.28125	23.526733	33.981318

Table 14. continued

ν (cm ⁻¹)	$\frac{E_0}{2\pi^2 x_m^2 \nu^2} (1 - \cos 2\pi x_m \nu)$	2E(ν) (computer sum with $\Delta x = 0.1$ sampling)
3. 4375	42. 873096	64. 285108
3. 59375	19. 613023	30. 592392
3. 75	0	$\sim 10^{-8}$
3. 90625	16. 600463	28. 200623
4. 0625	30. 696122	54. 600961
4. 21875	14. 232221	26. 568523
4. 375	0	$\sim 10^{-8}$
4. 53125	12. 336848	25. 550089
4. 6875	23. 056198	50. 485028
4. 8437	10. 796347	25. 060336
5. 0	0	$\sim 10^{-11}$

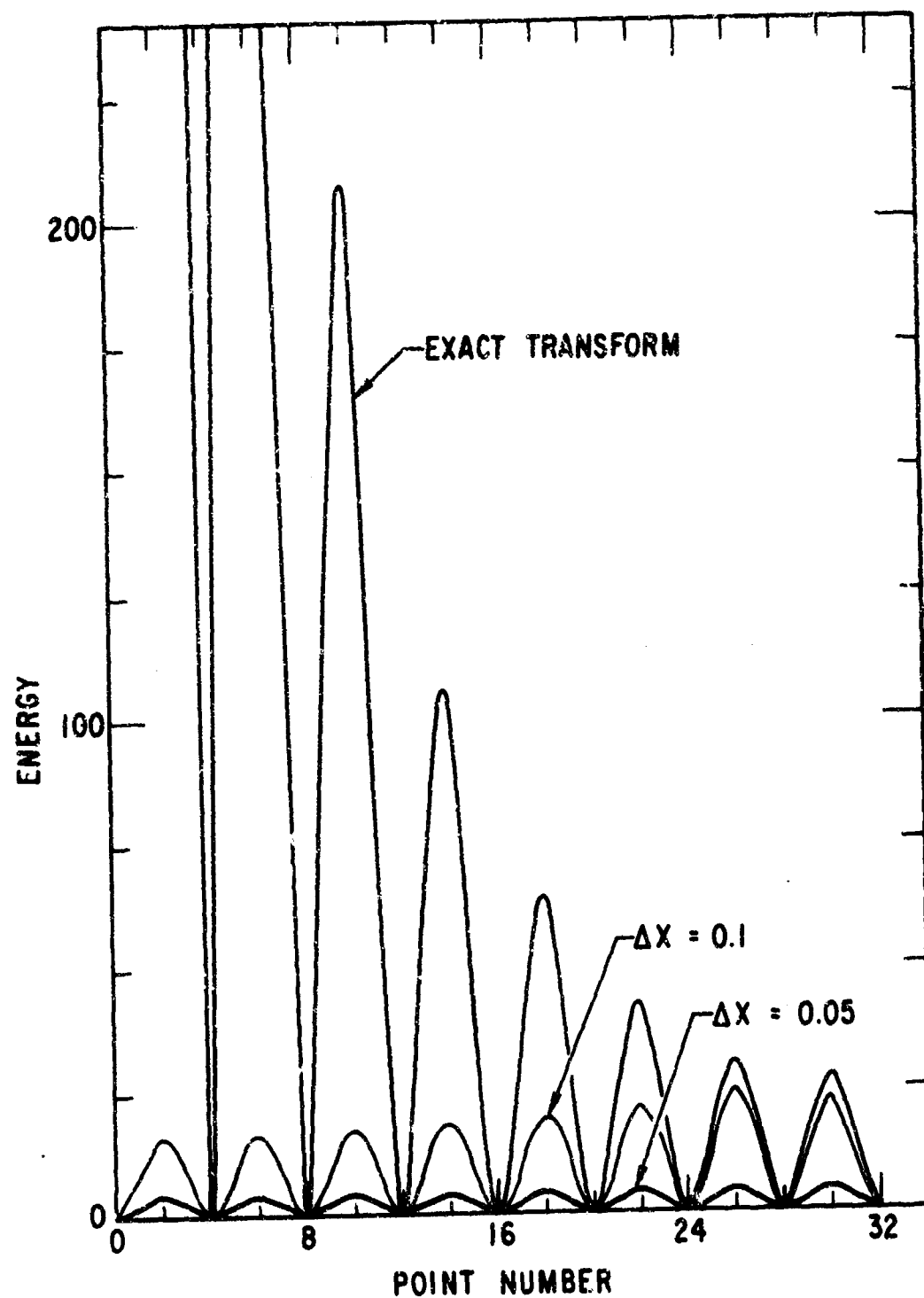


Fig. 70. Difference between sum and integral for different sampling frequencies of the interferogram. (1) Exact transform minus sum with $N = 16$ samples, $\Delta x = 0.1$. (2) Exact transform minus sum with $N = 32$ samples, $\Delta x = 0.05$.

interferograms of 32 and 16 points, respectively. Equation (51) is also plotted for comparison. In terms familiar to spectroscopists, these differences arise because the filtering in the "instrument" which determined the original interferogram, the straight line, did not cut off the radiation above $\nu_c = 1/2 \Delta x$. This radiation is being aliased back at lower wavenumbers and makes the energy appear higher at $\nu < \nu_c$. As Δx is decreased, in the examples shown, the cutoff frequency is increased, making less energy available above the cutoff frequency for aliasing into the region of interest.

C. COMPUTER PROGRAM

The computer program includes facilities for plotting both the interferogram and computed spectrum, facilities to subtract the asymptotic value from the raw interferogram, and also facilities to modify input points. The latter feature makes it convenient to apply experimental corrections to the interferogram. The heart of the program, of course, is the sections which perform the summing of the series. In the present program these are subroutines written in FORTRAN. Descriptions, flow charts, and listings of these subroutines follow.

Identification

FCTRAN - Fourier Cosine Transform by direct sum
6400/6600 FORTRAN

Purpose

To provide the Fourier Cosine transform of set of data, by a direct summation of the series

$$E(k\Delta\nu) = \Delta x \left[F(0) + 2 \sum_{j=1}^N F(j\Delta x) \cos 2\pi j k \Delta x \Delta \nu \right]$$

Method

For details of the method, see Fig. 71.

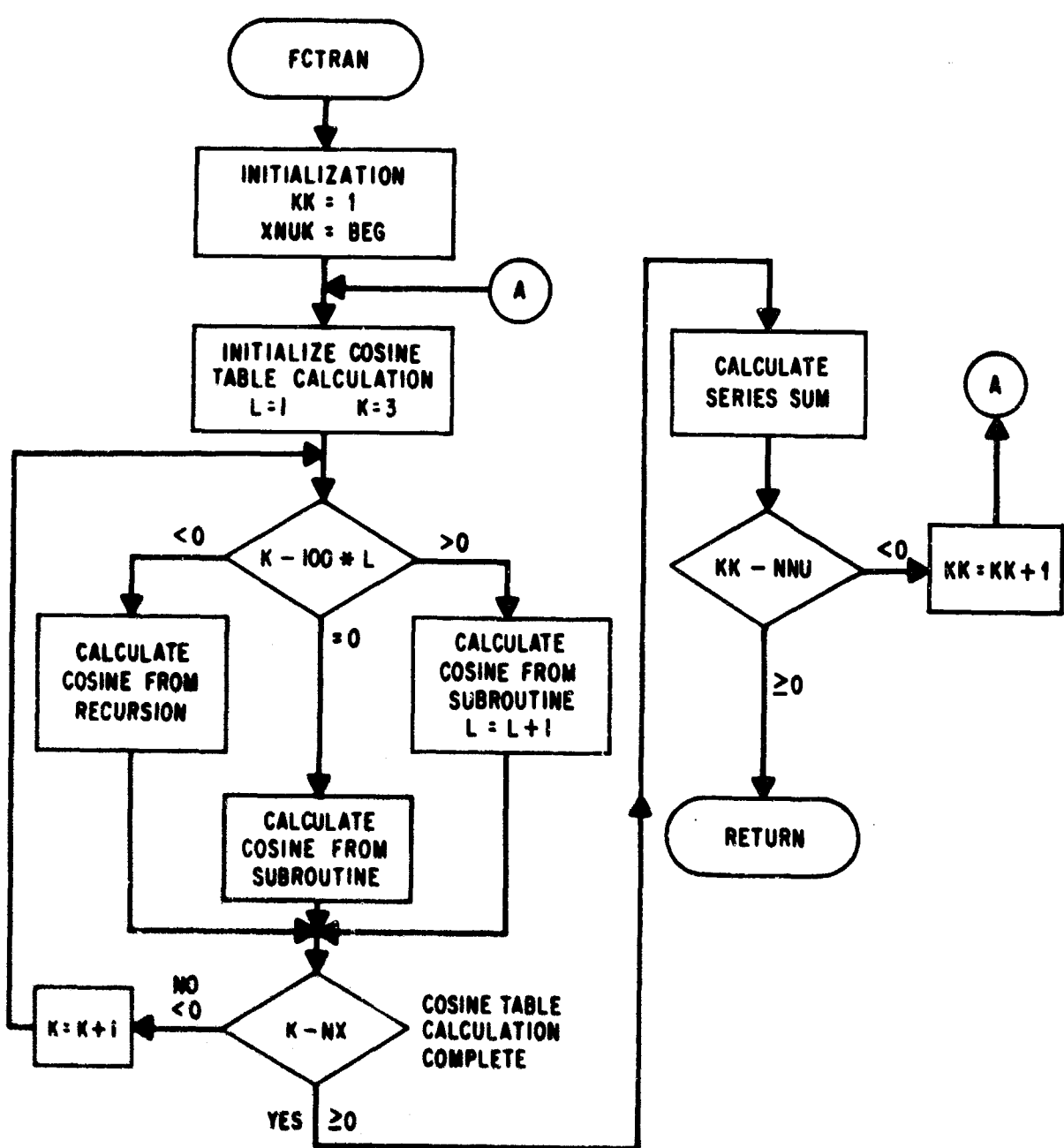


Fig. 71. Flow Chart of Direct Sum Method.

Usage

CALL FCTRAN (BEG, DELX, DNU, NX, FNUMX, PF, NNU, IAV)

where

BEG is the first value of v for which the transform is desired.

DELX is the spacing between points in the function to be transformed. The units of BEG, DNU, and FNUMX are reciprocal to the units of DELX.

DNU is the spacing between desired output points.

NX is the number of values in the function to be transformed.

FNUMX is the largest value of v for which the transform is desired.

PF is a constant phase factor shift which may be put in, usually zero.

NNU is the number of values.

IAV is not used.

The input data are assumed to be in the first NX locations of a common array, F. The output transform is placed into the first NNU locations in a common array, T. The content of F at the end of the execution is unchanged.

Restrictions

The calling program must specify as COMMON three arrays: NOUT, F, T, with the dimensions of 10, 8192, 16384, respectively.

Memory Requirement

256₈ exclusive of COMMON.

```

C SUBROUTINE FCTRAN (BEG,DELX,DNU,NX,FNUKX,PF,NNU,IAV)
C FCTRAN DIRECT SUM ALGORITHM FOR FOURIER COSINE TRANSFORM
C DECLARITIVE, FORMAT AND INITIALIZATION STATEMENTS
C
C COMMON NOUT,F,T
C DIMENSION F(4096,2), T(8192,2), NOUT(10)
C PRINT 9
C TPI=6.28318531
C XNUK=BEG
C
C INITILIZE COSINE TABLE CALCULATION
C
C DO 7 KK=1,NNU
C FR=XNUK*(DELX
C ARG=AMOD(FR,1.0)
C CST2=2.0*COS(ARG*TPI)
C ADF=ARG+PF
C T(1,2)=COS(TPI*ARG)
C ARG=AMOD(2.0*FR,1.0)+PF
C T(2,2)=COS(TPI*ARG)
C L=1
C
C CALCULATE COSTINE TABLE
C
C DO 5 K=3,NX
C IF (K=100*L) 1,3,2
C 1 T(K,2)=CST2*T(K-1,2)+T(K-2,2)
C 2 GO TO 5
C 3 INOIC=100*L+1
C L=L+1
C 4 GO TO 4
C 5 INOIC=100*L
C ARG=AMOD(IFLOAT(INOIC)*FR,1.0)+PF
C T(INOIC,2)=COS(TPI*ARG)
C CONTINUE
C
C SERIES SUM CALCULATION AND CALCULATION OF NEW FREQUENCY VALUE
C
C T(KK,1)=0.0
C DO 6 J=2,NX
C 6 T(KK,1)=F(J)+T(J-1,2)+T(KK,1)
C
C T(KK,1)=DELX*(F(1)+2.0*T(KK,1))
C XNUK=IFLOAT(KK)*REF
C CONTINUE
C
C RETURNING STATEMENTS
C
C 1 BEG=NNU+1
C 00 8 I=THEG,16382
C 8 T(I)=0.4
C RETURN
C
C FORMAT (IX,17HO) (PCT SUM METHOD)
C END
C
C FCS 1
C FCS 2
C FCS 3
C FCS 4
C FCS 5
C FCS 6
C FCS 7
C FCS 8
C FCS 9
C FCS 10
C FCS 11
C FCS 12
C FCS 13
C FCS 14
C FCS 15
C FCS 16
C FCS 17
C FCS 18
C FCS 19
C FCS 20
C FCS 21
C FCS 22
C FCS 23
C FCS 24
C FCS 25
C FCS 26
C FCS 27
C FCS 28
C FCS 29
C FCS 30
C FCS 31
C FCS 32
C FCS 33
C FCS 34
C FCS 35
C FCS 36
C FCS 37
C FCS 38
C FCS 39
C FCS 40
C FCS 41
C FCS 42
C FCS 43
C FCS 44
C FCS 45
C FCS 46
C FCS 47
C FCS 48
C FCS 49
C FCS 50
C FCS 51
C FCS 52
C FCS 53
C FCS 54-

```

Identification

FCTRAN - Fourier Cosine transform by Cooley-Tukey algorithm.

6400/6600 FORTRAN

Purpose

To provide the Fourier cosine transform of a set of data by the Cooley-Tukey algorithm applied to the series

$$E(k\Delta\nu) = \Delta x \left[F(0) + 2 \sum_{j=1}^N F(j\Delta x) \cos 2\pi j k \Delta x \Delta \nu \right]$$

Method

For details of the program, see the flow chart (Fig. 72). The input routines calculate the following quantities: The number of input, $N = 2^n$, and output points, $M = 2^m$, within the limitations of the memory of the computer. The interferogram is filled out with zeroes if necessary. $LD = 2 * M/N$. KB is the beginning of temporary storage in the F array. For all but the largest number of output points ($M = 8192$ in the present program), this is set to protect the input interferogram. $J = M/4$, $IBEG = M/2$, $NBEG = 0$. The calculation of the array resulting from one pass involves boxes i through ii. Initializing another pass involves boxes iii and iv. The output routines rearrange the spectrum so that the portion of interest fills in the lowest NNU positions in T . These routines also multiply by Δx and insert the phase factor if nonzero. The naming convention of FORTRAN to distinguish between fixed and floating point numbers is observed. Divisions of fixed point numbers is assumed truncated. Operations indicated with \dagger are complex.

For details of the mathematics, see Section B.

the calculated points when leaving.

NX is the number of values in the function to be transformed.

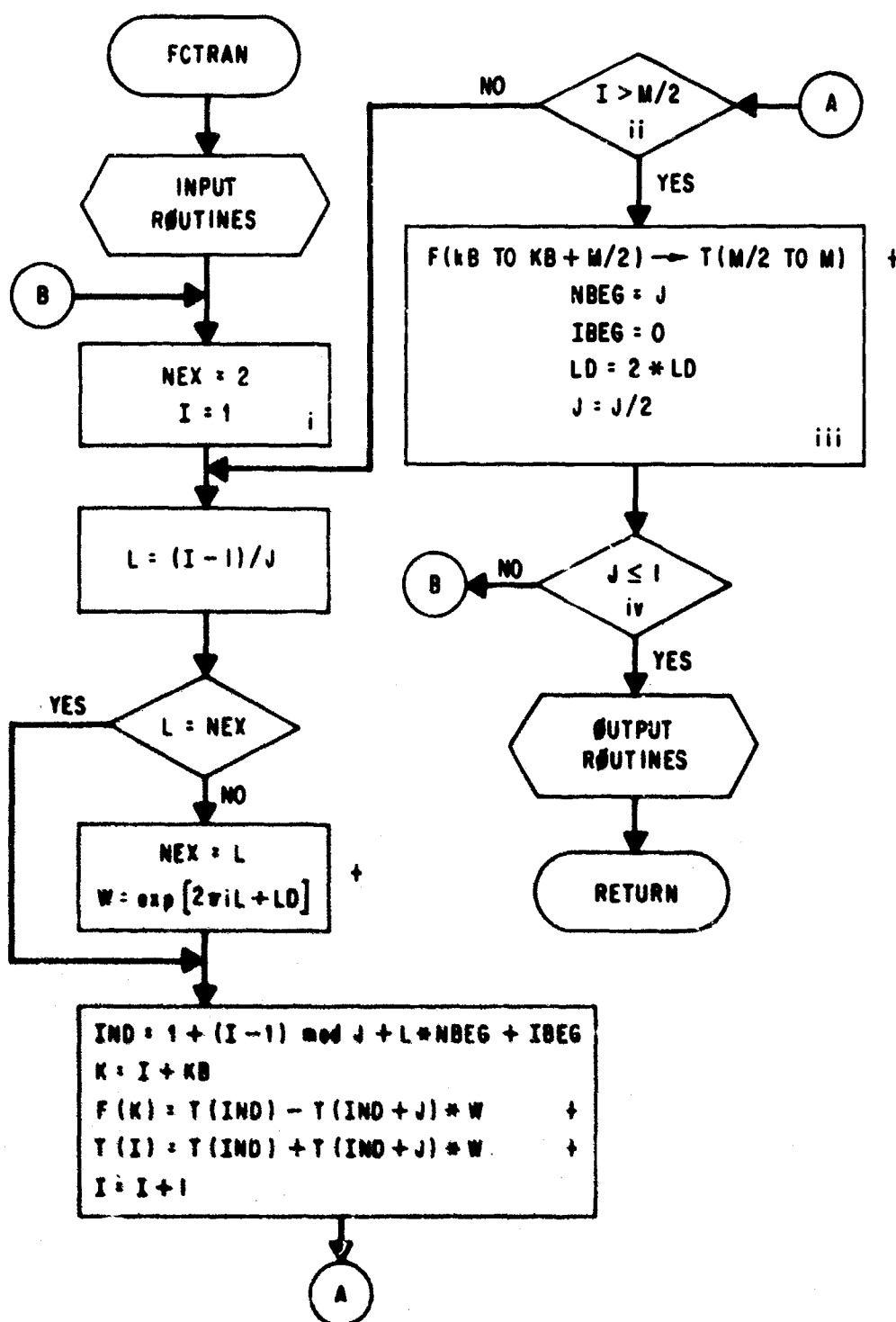


Fig. 72. Flow Chart of Cooley-Tukey Method.

Usage

CALL FCTRAN (BEG, DELX, DNU, NX, FNUMX, PF, NNU, IAV)
where

BEG is the first value of ν for which the transform is desired when calling this routine. When returning, it will be the value of ν corresponding to the value of $E(k\Delta\nu)$ in the first location of T. It will be an integral multiple of the value of DNU returned.

DELX is the spacing between points in the function to be transformed. The units of BEG, DNU, and FNUMX are reciprocal to the units of DELX.

DNU is the desired spacing between output points when entering the routine. It is the actual spacing between the calculated points when leaving.

NX is the number of values in the function to be transformed.

FNUMX is the largest value of ν for which the transform is desired. It is unchanged by the subroutines operations.

PF is a constant phase factor which may be inserted. It is usually zero.

NNU is the number of ν values desired when entering the program. It is the number of values beyond BEG for which the transform is calculated when leaving the program.

LAV not used.

The input data are assumed to be in the first NX locations of an array in COMMON, F. The output transform is placed into the first NNU locations in an array in COMMON, T.

Restrictions

The calling program must specify as COMMON three arrays: NOUT, F, T, with the dimensions of 10, 8192, 16384, respectively.

The contents of the array F will be modified by this subroutine if effective number of output points is 8192.

Memory Requirement

552₈ exclusive of COMMON storage.

WIRE INTERFACER IN CONNECT PLACE TO START RUN

REFERENCES

1. E. V. Loewenstein, *Appl. Opt.* 5, 845 (1966).
2. A. A. Michelson, *Phil. Mag. Ser. 5*, 31, 256 (1891).
3. P. Fellgett, thesis, Cambridge Univ. (1951).
4. P. Fellgett, *J. Phys. Radium* 19, 187 (1958).
5. H. A. Gebbie, *J. Phys. Radium* 19, 230 (1958). See also "Submillimeter Wave Spectroscopy Using a Michelson Interferometer," *Advances in Quantum Electronics*, J. R. Singer, Ed., Columbia Univ. Press, New York (1961).
6. J. Connes, *Rev. Opt.* 40, 45, 116, 171, 231 (1961). See also J. Connes, "Spectroscopic Studies Using Fourier Transformations," English translation NAVWEPS Rept. 8099, NOTS TP 3157, U. S. Naval Ordnance Test Station, China Lake, Calif. (January 1963).
7. J. Connes and P. Connes, *J. Opt. Soc. Am.* 56, 896 (1966).
8. E. E. Bell, *Infrared Physics* 6, 57 (1966).
9. E. E. Russell and E. E. Bell, *Infrared Physics* 6, 75 (1966).
10. J. E. Chamberlin, J. E. Giggs, and H. A. Gebbie, *Nature, London* 198, 874 (1963).
11. J. Strong, *J. Opt. Soc. Am.* 47, 354 (1957).
12. J. Strong and G. A. Vanasse, *J. Opt. Soc. Am.* 49, 844 (1959).
13. J. Strong and G. A. Vanasse, *J. Opt. Soc. Am.* 50, 113 (1960).
14. P. L. Richards, *J. Opt. Soc. Am.* 54, 1474 (1964).
15. R. T. Hall, D. Vrabec, and J. M. Dowling, *Appl. Opt.* 5, 1147 (1966).
16. P. Jacquinot, *Repts. Progr. Phys.* 23, 267 (1960).
17. L. Genzel, *J. Mol. Spectry.* 4, 241 (1960).
18. P. L. Richards, *J. Opt. Soc. Am.* 54, 1474 (1964).
19. L. Mertz, *Transformations in Optics*, John Wiley and Sons, Inc., New York (1965).
20. J. Bartling, *Am. J. Phys.* 34, 974 (1966).
21. M. Born and E. Wolf, *Principles of Optics*, Pergamon Press Ltd., London (1964).
22. J. M. Dowling, *J. Opt. Soc. Am.* 54, 663 (1964).
23. T. Williams, *J. Opt. Soc. Am.* 50, 1159 (1960).

24. E. V. Loewenstein, J. Opt. Soc. Am. 50, 1163 (1960).
25. A. Filler, J. Opt. Soc. Am. 54, 762 (1964).
26. Gordon Jones and Walter Gordy, Phys. Rev. 135, A295 (1964).
27. D. H. Rank, A. C. St. Pierre, and T. A. Wiggins, J. Mol. Spectry. 18, 418 (1965).
28. J. M. Dowling, J. Chem. Phys. 45, 3164 (1966).
29. R. G. Gordon, J. Chem. Phys. 43, 1307 (1965); and references cited therein.
30. R. G. Gordon, J. Chem. Phys. 45, 3165 (1966).
31. J. M. Dowling, J. Opt. Soc. Am. 54, 663 (1964).
32. M. Cowan and W. Gordy, Phys. Rev. 111, 209 (1958).
33. J. Pickworth and H. W. Thompson, Proc. Roy. Soc. (London) A218, 37 (1953).
34. R. T. Hall and J. M. Dowling, J. Chem. Phys. 45, 1899 (1966).
35. J. J. Gallagher and C. M. Johnson, Phys. Rev. 103, 1727 (1956).
36. P. G. Favero, A. M. Mirri, and W. Gordy, Phys. Rev. 114, 1534 (1959).
37. P. Arcas, et al., Appl. Opt. 2, 909 (1963).
38. M. D. Olman, M. D. McNelis, and C. D. Hause, J. Mol. Spectry. 14, 62 (1964).
39. C. Meyer, C. Haeusler, and P. Barchewitz, J. Physique 26, 799 (1965).
40. T. C. James and R. J. Thibault, J. Chem. Phys. 41, 2806 (1964).
41. E. D. Palik and K. N. Rao, J. Chem. Phys. 25, 1174 (1954).
42. H. M. Randall, Rev. Mod. Phys. 10, 72 (1938).
43. N. Wright and H. M. Randall, Phys. Rev. 44, 391 (1933).
44. R. B. Barnes, W. S. Benedict, and C. M. Lewis, Phys. Rev. 47, 918 (1935).
45. H. M. Randall, et al., Phys. Rev. 52, 160 (1937).
46. L. Genzel and W. Eckhardt, Z. für Physik 139, 578 (1954).
47. N. G. Yaroslavsky and A. E. Stanevich, Izv. Akad. Nauk. SSR, Ser Fiz. 22, 1145 (1958); Optics and Spectry. 5, 380 (1958).
48. H. A. Gebbie and G. A. Vanasse, Nature 178, 432 (1956).
49. G. A. Vanasse, J. Strong, and E. Loewenstein, J. Opt. Soc. Am. 49, 305 (1959).
50. A. Hadni and C. Janot, Revue d' Optique 39, 451 (1960).

51. L. R. Blaine, E. K. Plyler, and W. S. Benedict, J. Research Nat. Bur. Standards 66A, 223 (1962).
52. K. N. Rao, et al., J. Opt. Soc. Am. 52, 862 (1962).
53. K. N. Rao, R. V. deVore, and E. K. Plyler, J. Research Nat. Bur. Standards 67A, 351 (1963).
54. P. L. Richards, J. Opt. Soc. Am. 54, 1474 (1964).
55. F. K. Kneubuhl, J. F. Moser, and H. Steffen, J. Opt. Soc. Am. 56, 760 (1966).
56. R. T. Hall, The Pure Rotational Spectrum of Water Vapor: Calculated Frequencies and Relative Intensities, Aerospace Corp. Report TR-669(9260-01)-7 (March 1966).
57. D. M. Gates, et al., Line Parameters and Computed Spectra for Water Vapor Bands at 2.7μ , Nat. Bur. Standards Monograph 71 (August 1964).
58. P. E. Fraley and K. N. Rao, J. Mol. Spectry. 19, 131 (1966).
59. M. Lichtenstein, V. E. Derr, and J. J. Gallagher, J. Mol. Spectry. 20, 391 (1966).
60. P. E. Fraley, Ph.D. thesis, Ohio State University, 1966.
61. W. S. Benedict, Mem. Soc. Roy. Sci. Liege, Spec. Vol. 2, 18 (1957).
62. W. S. Benedict, Theoretical Studies of High Resolution Spectra of Atmospheric Molecules, Final Report AFCRL-65-573 (1965).
63. D. Kivelson and E. B. Wilson, Jr., J. Chem. Phys. 21, 1229 (1953).
64. W. S. Benedict, N. Gailar, and E. K. Plyler, J. Chem. Phys. 24, 1139 (1956).
65. J. R. Rusk (private communication) (1965).
66. C. H. Townes and A. L. Schawlow, Microwave Spectroscopy, McGraw-Hill Book Co., Inc., New York (1955), Chap. 13, p. 360.
67. J. Connes and V. Nozal, J. Phys. Radium 22, 359 (1961).
68. R. W. Parsons and James A. Roberts, J. Mol. Spectry. 18, 412 (1965).
69. W. S. Benedict and R. Herman, J. Quant. Spectr. Transfer 3, 265 (1963).
70. D. H. Rank, D. P. Eastman, B. S. Rao, and T. A. Wiggins, J. Mol. Spectry. 10, 34 (1963).
71. S. Roberts and D. D. Coon, J. Opt. Soc. Am. 52, 1023 (1962).
72. E. V. Loewenstein, J. Opt. Soc. Am. 51, 108 (1961).
73. J. R. Aronson, H. G. McLinden, and P. J. Gielisse, Phys. Rev. 135, A785 (1964).

74. K. F. Rank and L. Genzel, *Appl. Opt.* 1, 643 (1962).
75. Am Mitsuishi, et al., *J. Appl. Phys. (Japan)* 2, 574 (1963).
76. R. Ulrich, K. F. Rank, and L. Genzel, *IEEE Trans. Microwave Theory Tech.* 11, 363 (1963).
77. W. Culshaw, *IEEE Trans. Microwave Theory and Tech.* 8, 182 (1960); 9, 135 (1961); 10, 331 (1962).
78. E. A. Lewis and J. P. Casey, *J. Appl. Phys.* 23, 605 (1952).
79. J. P. Casey and E. A. Lewis, *J. Opt. Soc. Am.* 42, 971 (1952).
80. N. Markuvitz, Waveguide Handbook, McGraw-Hill Book Co., Inc., New York (1951), p. 195.
81. W. Culshaw, *IEEE Trans. Microwave Theory and Tech.* 7, 221 (1959).
82. P. Vogel and L. Genzel, *Infrared Physics* 4, 257 (1964).
83. E. K. Plyler, D. J. C. Yates, and H. A. Gebbie, *J. Opt. Soc. Am.* 52, 859 (1962).
84. W. Boldt, *Monatsber. Deutschen Akad. Wiss. Berlin* 2, 735 (1960).
85. E. V. Loewenstein and D. R. Smith, *J. Opt. Soc. Am.* 56, 1446 (1966).
86. J. W. Cooley and J. W. Tukey, *Math. of Computation* 19, 297 (1965).
87. M. L. Foreman, *J. Opt. Soc. Am.* 56, 978 (1966).
88. J. M. Dowling and R. T. Hall, *J. Opt. Soc. Am.* 57, 00 (1967).
89. F. K. Kneubühl, J. F. Moser, and H. Steffen, *J. Opt. Soc. Am.* 57, 00 (1967).
90. J. F. Moser, H. Steffen, and F. K. Kneubühl, *Appl. Opt.* 5, 1969 (1966).
91. R. D. Rawcliffe and C. M. Randall, *Appl. Opt.* 6 (in preparation).
See also Section IV-D of this report.

APPENDIX

INTERFEROMETRY AND CONVENTIONAL SPECTROSCOPY

In theory, two-beam interferometry has a decided S/N advantage over conventional single-slit dispersive spectroscopy when detector noise is the limiting factor (see Section I, Introduction). In a paper on FIR instrumentation, Richards(Ref. 14) describes an experimental comparison of a Michelson and a lamellar grating interferometer with a conventional grating spectrometer. With respect to the comparative performance of these two types of instruments in the FIR, Richards said,

"We experimentally verify the Fellgett advantage of the interferometer to within about a factor of 3 in time. This is of the order of the uncertainties in our estimates of noise levels and grating and filter efficiencies."

This statement was disputed by Kneubuhl, Moser, and Steffen (Ref. 55) in a paper describing the construction and performance of a conventional FIR grating spectrometer. They conclude,

"From these spectra, we conclude that the performance of Fourier-transform spectrometers may be slightly better than that of grating spectrometers, but the difference is certainly smaller than that stated by Richards. The spectral resolution yet obtained by both types of spectrometers lies between 0.1 and 0.05 cm^{-1} in the spectral region between 30 and 60 cm^{-1} ."

This statement was challenged by Dowling and Hall (Ref. 88), who said, "While achieving remarkable performance with their spectrometer we feel that some comments and conclusions arrived at by KMS with respect to the comparative performance of these two types of instruments are not supported by the evidence presented and, furthermore, are in disagreement with our experience with a far-infrared, lamellar grating interferometer."

And also with respect to the resolution yet obtained by both types of instruments they said:

"To the best of our knowledge this resolution has not yet been demonstrated for conventional grating spectrometers and has only recently been demonstrated for interferometric instruments."

More details are given in these and other papers (Refs. 15, 89, 90).

With the exception of the detector employed, the optical parameters of the conventional grating spectrometer (Ref. 55) and the Aerospace lamellar grating interferometer (Ref. 15) are quite similar. These are given in Table A-1.

In the previous comparison (Refs. 55, 88, 90), there was quite a large difference in experimental conditions (pressure and absorbing path length) in the respective water vapor spectra. Presented here are data obtained with the lamellar grating interferometer under experimental conditions closer to those used by KMS (Refs. 55, 90).

We obtained two single-beam²² runs for H₂O with the lamellar grating interferometer with an absorbing path length of ~9.2 m and a pressure of ~1-1/2 Torr. The first of these was a reasonably high resolution run ($\Delta\nu_M \sim 0.10 \text{ cm}^{-1}$). The transformed interferogram (i.e., the spectra) showed the triplet at ~38 cm⁻¹ quite clearly resolved (Ref. 88), indicating the run had good resolution and reasonable sensitivity (the line at 38.642 cm⁻¹ is quite weak and close to the strong line at 38.792 cm⁻¹). However, the "new" lines seen by KMS (Ref. 55) at 46.3, 49.5, and 50.25 cm⁻¹ were not observed. Although the apparent²³ S/N for this run was somewhat poorer

²² In order to obtain a long absorbing path (to correspond to the long absorbing path used by KMS) the entire optical path (from detector to source) was used by admitting H₂O to the whole system. This, of course, precluded double-beam operation, and thus we encountered the dynamic range problem.

²³ We believe this is due in part to the dynamic range problem.

Table A-1. Comparison of a Conventional Grating Spectrometer^a
and a Lamellar Grating Interferometer^b

	Conventional Spectrometer	Interferometer
Grating area	1050 cm ²	930 cm ²
f-number	~ f/4	~ f/4
Slit or entrance aperture area	0.8 cm ²	0.7 cm ²
Detector and NEP	Golay $(8 \times 10^{-11})^c$	Ge Bolometer T = 4.2 °K (5×10^{-12})

^aRef. 55

^bRef. 15

^cThis is from advertising literature from Eppley Laboratories (Golay) and Texas Instruments (Ge Bolometer). It has been our experience in comparing our bolometer and Golay cells that the bolometer is ~6 to 9 times better NEP-wise than the factor of 16 deduced from the advertising literature.

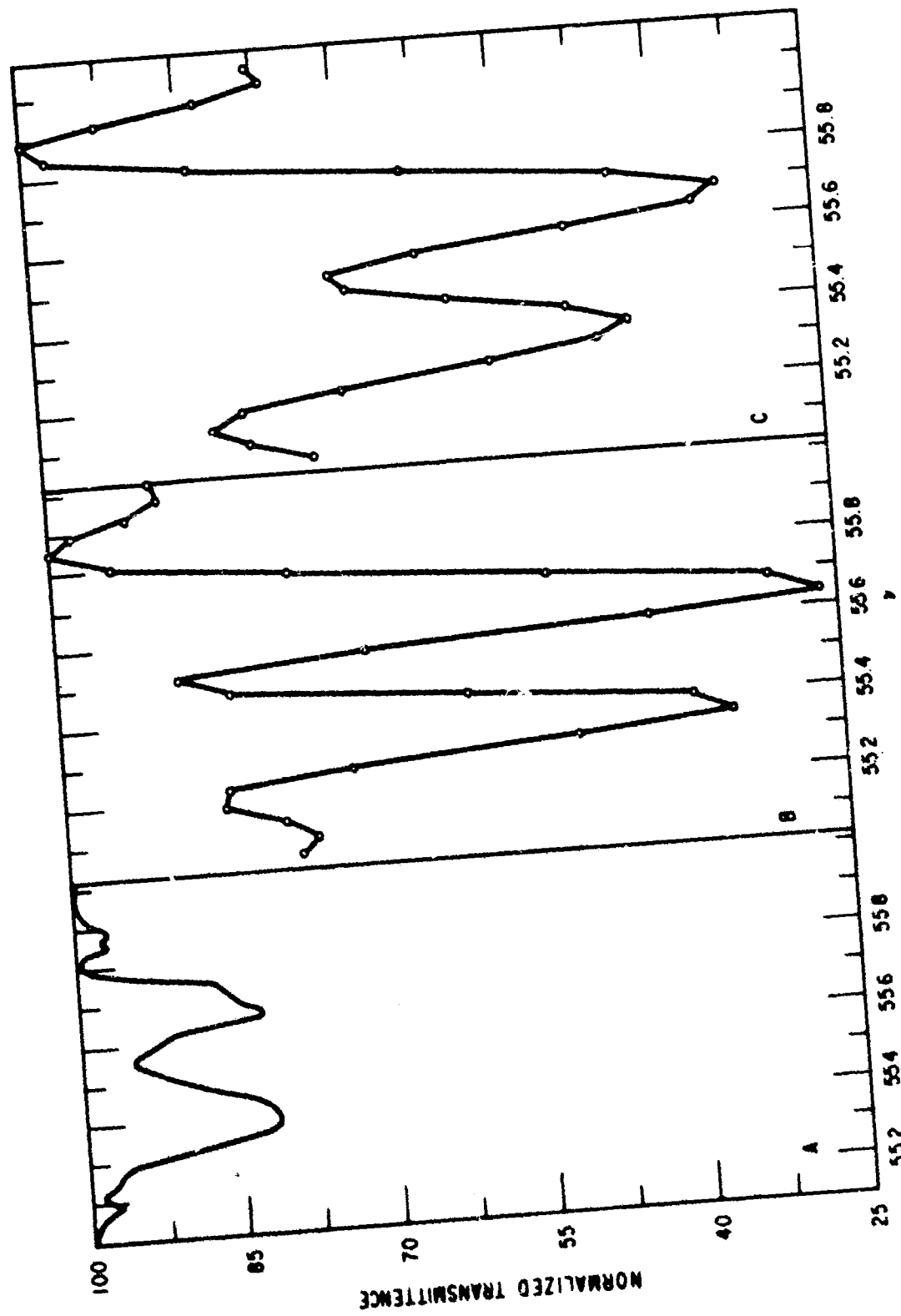
than in double-beam runs (Ref. 88), we feel it was sufficiently high to detect these lines if the relative intensities as shown in Fig. 3 of Ref. 55 are anywhere near correct. Their absence confirms our contention (Ref. 88) that these lines are second-order water vapor lines (and they do indeed correspond exactly within the accuracy of the wavelength quoted by KMS) appearing in the first-order spectrum because of incomplete filtering.

A second run was made in a much shorter time. The optical path difference attained was ~ 5.0 cm ($\Delta\nu_M \sim 0.20 \text{ cm}^{-1}$) in increments of 30μ ²⁴ of optical path difference and each point was sampled for 0.75 sec.²⁵ This interferogram function was FCT twice, once with $L \approx 5.0$ cm (total time of run, including dead time = 41.8 min) and also with $L \approx 3.5$ cm (by deleting the last 1.5 cm of the interferogram, which corresponds to a running time of 29.3 min). The $55-56 \text{ cm}^{-1}$ regions of these spectra are compared with the corresponding region as given by KMS (Fig. 4 of Ref. 55) in Fig. 73. The experimental conditions are listed in Table A-2. The results of KMS are "normalized transmittance." We have "normalized" our curves by assuming that the greatest intensity in this region corresponds to 100% transmission (and this appears to be what KMS have done). We make the following observations:

1. In Fig. A-1, the depth-of-absorption curves B and C are much greater than in A.
2. The B and C lines appear much more symmetrical than in A, especially the high wavenumber component.
3. In A the low wavenumber component appears slightly stronger than the high wavenumber component. In B and C the opposite is true. Theoretical relative intensities predict the higher wavenumber component to be stronger (Ref. 55).

²⁴ We point out that $\Delta x = 30 \mu$ corresponds to $\nu_c = 166 \text{ cm}^{-1}$. This Δx was chosen since we had changed our filtering slightly, and to be sure of avoiding aliasing we chose $\Delta x = 30 \mu$. Actually we could have used $\Delta x = 40 \mu$ as it was apparent from the spectrum $\Delta\nu_c \leq 125 \text{ cm}^{-1}$. This would have resulted in a $\sim 33\%$ reduction in time with small loss in the S/N in the spectrum.

²⁵ The dead time (i.e. the time it takes to move from point to point) during which no data are taken, for 30μ optical path difference steps, is also 0.75 sec. Thus the efficiency of this run, measuring time per total time, was $\sim 50\%$.



A-5

Fig. A-1. The 55 to 56 cm^{-1} region of the water vapor spectrum. A, from the paper of KMS; B and C from a single-beam interferogram.

Table A-2. Comparison of Experimental Parameters
Illustrated in Figure 71

	A (KMS)	B	C
Absorbing path	7.4 m	9.2 m	9.2 m
Pressure	2 Torr	1-1/2 Torr	1-1/2 Torr
Computer time	0	~44 sec ^a	~44 sec ^a
Scan time for 55-56 cm ⁻¹ region	17.8 min	0.42 min ^b	0.29 min ^b

^a Computer is a CDC 6600. The actual FCT time is small compared with the read-in, read-out time, etc.

^b Based on the total time it took to get the interferogram and the fact that 100 cm⁻¹ was covered. See text for a discussion on KMS's objection to this.

4. The apparent noise level increases from B to C, whereas one would expect it to decrease (see Section V). We note in particular that maximum intensity variation in the $55.8 \rightarrow 56.0 \text{ cm}^{-1}$ more than doubles in going from B to C (no H_2O absorption line is expected here). We interpret these variations (and they are seen in proximity to the other strong and medium lines) as being the sidelobes discussed in Section II. We thus infer that these lines are narrower than the scanning functions of these two runs and the variations observed are not true noise. We make no comment on the noise level for the spectra shown in Fig. 71-A since KMS made no estimate of their S/N

Kneubühl, Moser, and Steffen (Ref. 89) have objected to the "equivalent scan time" used by Dowling and Hall (Ref. 88) in comparing results obtained with the two instruments, on the basis,

"The equivalent scan time introduced by Dowling and Hall does not seem to be a great value. Theoretically, high resolution of a small spectral region can be achieved by an aperiodic interferometer in a short time (e.g., 5 min). But this requires a narrow band filter with a bandwidth of the order of magnitude of 1 cm^{-1} , e.g., a diffraction-grating spectrometer."

Although a diffraction-grating spectrometer would serve admirably as a narrow bandpass filter (as long as higher order radiation is filtered out), such a complicated instrument may not be necessary. The progress in fabricating narrow bandpass filters (Ref. 9) for the FIR is quite encouraging in this respect.

In his well-known treatment, Fellgett (Refs. 3, 4) has shown that the S/N gain of a multiplex instrument over conventional scanning spectrometers is $\sqrt{N}/2$, where N is the number of spectral elements (resolution widths) to be studied. The advantage is 1 when $N = 4$. That is, all other quantities being equal, the interferometer has the advantage if $N > 4$, the conventional spectrometer when $N < 4$. Usually many more than four spectral elements are desired.

At the present time the conventional spectrometer offers the advantage of short wavenumber scans, but with the development of narrow bandpass

filters (Ref. 91) and the more efficient use of the time available for measurement (i.e., minimization of the dead time), we believe this advantage is a temporary one.²⁶

²⁶ An opinion expressed in a letter to J. F. Moser.

UNCLASSIFIED
Security Classification

DOCUMENT CONTROL DATA - R&D

(Security classification of title, body of abstract and indexing annotation must be entered when the overall report is classified)

1. ORIGINATING ACTIVITY (Corporate author) Aerospace Corporation El Segundo, California	2a. REPORT SECURITY CLASSIFICATION Unclassified
	2b. GROUP

3. REPORT TITLE INVESTIGATIONS IN THE FAR-INFRARED WITH A LAMELLAR GRATING INTERFEROMETER

4. DESCRIPTIVE NOTES (Type of report and inclusive dates)

5. AUTHOR(S) (Last name, first name, initial)

Dowling, Jerome M.

6. REPORT DATE March 1967	7a. TOTAL NO. OF PAGES 198	7b. NO. OF REFS 91
8a. CONTRACT OR GRANT NO. AF 04(695)-1001	9a. ORIGINATOR'S REPORT NUMBER(S) TR-1U01(9260-01)-7	
b. PROJECT NO.		
c.	9b. OTHER REPORT NC(S) (Any other numbers that may be assigned this report)	
d.	SSD-TR-67-30	

10. AVAILABILITY/LIMITATION NOTICES

~~Distribution of this document is limited.~~

11. SUPPLEMENTARY NOTES	12. SPONSORING MILITARY ACTIVITY Space Systems Division Air Force Systems Command Los Angeles, California
-------------------------	---

13. ABSTRACT

The theory and practice of far-infrared, two-beam interferometry is summarized. A description of the instrumentation and performance of the Aerospace Corporation two-beam, double-beam, far-infrared lamellar-grating interferometer is given. Detailed experimental measurements and analyses of the pure rotational spectra of the atmospheric molecules nitric oxide (NO) and water (H_2O) are presented. Also discussed in depth are measurements of the optical constants of some important far-infrared window materials and the fabrication and performance of narrow bandpass filters for the far-infrared. Included is a discussion of noise, experimental errors, and problems in the practice of two-beam interferometry. Finally, a summary is given of the computational programs necessary and convenient for reducing the raw interferometric data to their more readily used spectral form.

UNCLASSIFIED

Security Classification

14.

KEY WORDS

Far-Infrared
Interferometry
High Resolution
Interferogram
Rotational Spectra
Optical Constants
Narrow Bandpass Filters
Computer Programs

Abstract (Continued)

UNCLASSIFIED

Security Classification